Polarization Observables in $\vec{\gamma}\vec{p} \to p\pi^+\pi^-$ Using the g9a (FROST) Target and the CLAS Spectrometer

Sungkyun Park
Florida State University

August 13, 2013

Abstract

The study of baryon resonances provides a deeper understanding of the strong interaction because the dynamics and relevant degrees of freedom hidden within them are reflected by the properties of the excited states of baryons. Higher-lying excited states at and above 1.7 GeV/c^2 are generally predicted to have strong couplings to the $\pi\pi N$ final states via $\pi\Delta$ or ρN intermediate states. Double-pion photoproduction is therefore important to search for and investigate the properties of high-mass resonances. The excited states of the nucleon are usually found as broadly overlapping resonances which may decay into a multitude of final states involving mesons and baryons. Polarization observables make it possible to isolate single-resonance contributions from other interference terms. The CLAS g9a (FROST) experiment, as part of the N^* spectroscopy program at Jefferson Laboratory, has accumulated photoproduction data using circularly-polarized photons incident on a longitudinally-polarized butanol target in the photon energy range 0.3 to 2.4 GeV. This document summarizes how the beam-helicity asymmetry $\mathbf{I}^{\odot}$, the target asymmetry $\mathbf{P_z}$, and the helicity difference $\mathbf{P_z^{\odot}}$ for the reaction $\vec{\gamma}\vec{p} \to p\pi^+\pi^-$ have been extracted from the g9a dataset.

Contents

1 Introduction

Effective theories and models have been developed to better understand the properties of baryon resonances. Various constituent quark models (CQMs) are currently the best approach to make predictions for the properties of the baryon ground states and excited states. However, the predictions for the hadron spectrum made by these models do not match accurately the states measured by experiment, especially at high energies. These models predict many more resonances than have been observed, leading to the so-called "missing resonance" problem. The latest results in baryon spectroscopy suggest that 3-body final states are very likely key for the discovery of the higher-lying unobserved resonances. Especially, the photoproduction of double-pion final states [1] may give us very useful data to investigate many high-mass resonances because their cross sections dominate above W $\approx$ 1.9 GeV ($E_\gamma \approx 1.46$ GeV). Quark models predict $\gamma N \to N^\star \to \Delta\pi \to N\pi^+\pi^-$ and $\gamma N \to N^\star \to N\rho \to N\pi^+\pi^-$ as dominant resonant decay modes leading to $\gamma p \to p\pi^+\pi^-$. However, these modes are difficult to observe because detectors with a large angular acceptance are needed and a large non-resonant background contributes to the final state.

2 FROST Experiment at JLab

The experimental Hall B at JLab provides a unique set of experimental devices for the FROST experiment. The CEBAF Large Acceptance Spectrometer (CLAS) [2] housed in Hall B is a nearly-4π spectrometer. The bremsstrahlung tagging technique, which is used by the broad-range photon tagging facility at Hall B [3], can tag photon energies over a range from 20 % to 95 % of the incident electron energy and is capable of operation with CEBAF beam energies up to 5.5 GeV. The remaining element which is indispensable for double-polarization experiments is a frozen-spin target [4]. The FROST target uses butanol as the ideal target material with a theoretical dilution factor of approximately 13.5 %. This material is dynamically polarized outside the CLAS spectrometer using a homogeneous magnetic field of about 5.0 T and cooled to approximately 0.5 K. Once polarized, the target is then cooled to a low temperature of 30 mK, enough to preserve the nucleon polarization in a more moderate holding field of about 0.5 T. The target is then moved back into the CLAS spectrometer, and data acquisition with a tagged photon beam can commence. In this FROST-g9a experiment, the target polarization was longitudinal in combination with linearly- and circularly-polarized photons. The circularly-polarized photons covered the energy range 0.5 - 2.3 GeV. In addition to the polarized butanol target, the experiment also used carbon and polyethylene targets at approximately 6 cm and 16 cm further downstream, respectively. They are useful for various systematics checks and for the determination of the contribution of bound nucleons in the butanol data. This analysis is organized as follows. In Section 3, we shall discuss the identification of the photon and final-state particles, kinematic fitting, corrections, and additional cuts used to tune the g9a dataset. At the same time, the beam and target polarization will be introduced. The next sections summarize how the asymmetries for the reaction $\gamma p \to p\pi^+\pi^-$ have been extracted from the g9a data. In Section 4.2, the beam asymmetry is discussed and Section 4.3 presents the target asymmetry. Finally, in Section 4.4, the helicity difference will be described. The results and conclusions of this analysis are discussed in Section 5.

3 Event Selection

3.1 The g9a Dataset

The data for the g9a experiment (FROST-g9a) were taken between November 3th, 2007, and February 12th, 2008. The g9a data are divided into two major parts according to the polarization type of the incident photon beam: circular and linear polarization. In this analysis, the data with a circularly-polarized photon beam and a longitudinally-polarized target were used. The circularly-polarized dataset is organized in two parts according to the electron beam energy: one is the data from $E_{e^-} = 1.645$ GeV and another is from $E_{e^-} = 2.478$ GeV. All these data are broken up into seven different periods.[1] Table 1 shows the different experimental conditions of the g9a data.

Target Polarization	Beam Polarization	Electron Beam Energy (GeV)	Dates	Run Range	Period
Longitudinal	Circular	1.645	11/10/07 - 11/10/07	55521 - 55536	1
			11/11/07 - 11/13/07	55537 - 55555	2
			11/14/07 - 11/20/07	55556 - 55595	3
		2.478	11/27/07 - 11/30/07	55604 - 55625	4
			11/30/07 - 12/07/07	55630 - 55678	5
			02/04/08 - 02/07/08	56164 - 56193	6
			02/07/08 - 02/11/08	56196 - 56233	7
	Linear	3.539	12/07/07 - 12/20/07	55678 - 55844	
		2.751	01/05/08 - 01/11/08	55854 - 55938	
		4.599	01/17/08 - 02/03/08	55945 - 56152	

Table 1: The datasets of the g9a experiment classified according to a wide variety of characteristics, such as the target polarization, the beam polarization, the electron beam energy, dates, and run numbers. The data using a circularly-polarized beam are grouped in periods with similar run conditions.

The information included in the raw data of the g9a experiment consists of QDC (Charge to Digital Convertor) and TDC (Time to Digital Converter) channel IDs and values. The data must then undergo reconstruction, or be cooked (converting these data into physical quantities like particle IDs, positions, angles, energies, and momenta) in order to be ready for a physics analysis. The data calibration is carried out for each detector component of CLAS independently. After the detectors have been calibrated and the particle tracks have been reconstructed, the cooking of the data is complete and the data are made available for analysis. Each event has its information organized in data banks. These data banks hold not only the properties of the particles involved in the reaction but also information about detector hits.

[1] A period is defined as a group of runs with similar conditions like the same target polarization or 1/2-wave plate status in the data using a circularly-polarized photon beam and longitudinally-polarized target.

3.2 Reaction Channel and General Event Selection

The reaction channel of interest in this analysis is $\gamma p \to p\pi^+\pi^-$ using a circularly-polarized photon beam and this channel is broken up into different topologies as shown in Table 2. A topology is defined according to the detected particles in the final state: the two-particle final states (Topologies 1-3) and the three-particle final state (Topology 4). A particle which is not detected in a given topology can be identified through the missing-mass technique. For this method, the Lorentz vectors of the incoming beam and the target are used. The four-momentum of an identified particle in the reaction $\gamma p \to p\pi^+\pi^-$ is determined from the measured three momentum and the particle energy. The missing four-momentum is given by:

$$x^\mu = k^\mu + P^\mu - \sum_{i=1}^{2,3} p_i^\mu \,, \tag{1}$$

where k^μ and P^μ are the photon and proton-target four-momenta, and p_i^μ are the four-momenta of the two or three detected particles. The missing mass m_X is defined as:

$$m_X^2 = x^\mu x_\mu \,. \tag{2}$$

The missing-mass distribution is used to check the condition of the data after applying corrections and cuts. The four-momentum vector x^μ of Equation 1 is used to complete the set of four-momentum vectors for events of Topologies 1, 2, and 3 (Table 2).

Topology	Reconstructed particles				Missing mass of interest
	total	p	π^+	π^-	m_X
1	2	1	1	0	m_{π^-}
2	2	1	0	1	m_{π^+}
3	2	0	1	1	m_p
4	3	1	1	1	0

Table 2: Identification of the $\gamma p \to p\pi^+\pi^-$ channel using different topologies. Reconstructed particles are identified by the **PID** information from the **GPID** bank.

Since the g9a experiment has used a trigger which required at least one charged particle in CLAS, the trigger file used during data-taking allowed for the recording of a large variety of events. In order to analyze only the specific topologies of the reaction $\gamma p \to p\pi^+\pi^-$, events possessing the final-state particles of interest should be filtered using the particle's identification number (PID), which is determined during the cooking process. Events that do not meet this requirement are ignored and subsequently omitted from the analysis. The calculation of the detected particles' mass, which is necessary to determine the PIDs of the final particles, uses two independently measured quantities, momentum (p) and velocity as fraction of the speed of light (β). The magnitude of the particle's momentum (p) is determined with an error of $< 1\,\%$ using the measurements made by the CLAS Drift Chambers (DC) [2]. The β of the detected final-state particle is determined using a combination of the Start Counter (SC), the Time of Flight (TOF), and the particle's detected trajectory through CLAS with an error of up to 5 % [2]. A detected particle's mass can then be calculated by:

$$m^2_{\text{particle}\,X} = \frac{p^2(1-\beta^2)}{\beta^2}\,. \tag{3}$$

After the particle's mass has been calculated, it is compared to the masses of known particles (hadrons and leptons). If this calculated mass matches that of a known particle (within resolution), the PID associated with that mass is assigned to the final-state particle. This value can then be used to select certain final-state particles for analysis. Therefore, to select events that match one of the four topologies, the PID value is used and the necessary final-state particles are detected. In this analysis, information regarding the properties of these final-state particles (their 4-vectors, vertex information, etc.) has been extracted from the GPID [5] data banks and used for kinematic fitting and application of cuts and systematic corrections, and the extraction of the polarization observables.

3.3 Photon and Particle Identification

3.3.1 Photon Selection

The electrons, which are used to produce the beam of polarized photons, are delivered from the accelerator into Hall B. They are carried in the form of 2 ns bunches. The circularly-polarized photon beam is also produced in the form of 2 ns bunches by directing the bunch of longitudinally-polarized electrons to the amorphous radiator. It is very important to determine the correct photon in each event because the photon energy is key to understanding the initial state of the event. To determine the exact photon corresponding to a physics event, a timing window can be used which satifies the consistency check between the Tagger and Start Counter times.

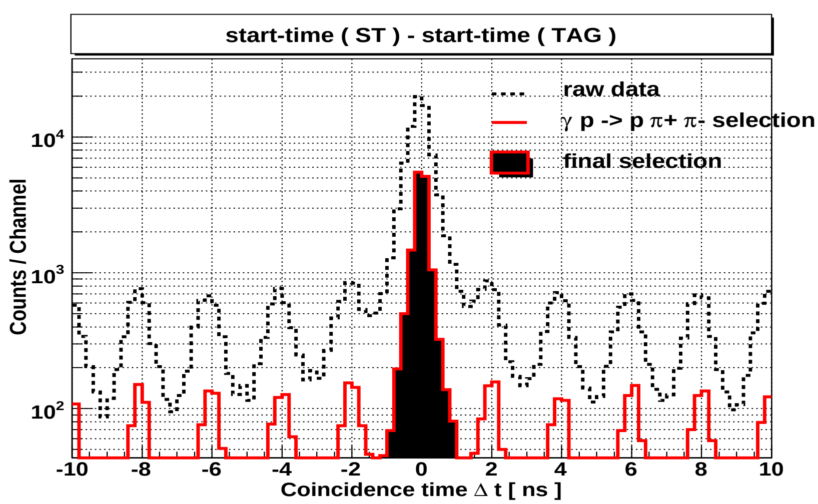

Figure 1: Coincidence-time distribution of tagged photons for the raw data (dotted histogram) and after applying all $\gamma p \to p\pi^+\pi^-$ selection cuts (solid histogram). Events of the center bins filled in black indicate the candidates for the final selection.

The event start-time difference between the Tagger and the Start Counter at the interaction point, Δt_{TGPB}, is defined as the coincidence time between the Tagger and the CLAS spectrometer. Figure 1 shows the distribution of tagged photons as a function of the coincidence time, Δt_{TGPB}, on a logarithmic scale. In the central peak, there are events with the "true" tagger-CLAS coincidence time. Accidental coincidences can be seen as a series of other peaks associated with different beam buckets. Only true coincident events determined by:

$$|\,\Delta t_{TGPB}\,| \, < \, 1.2 \text{ ns} \tag{4}$$

are selected. The tagged energy of that photon will be used as the photon energy for the event. The fraction of accidental coincidences remaining in the central peak is $< 3\,\%$ and is calculated from the comparison in the yields between the central peak and neighboring beam buckets. When events with only one photon are selected, the fraction of accidental coincidences in the data is reduced strongly. In this analysis, events with one "true" photon are selected using NGRF $= 1$ and TAGRID the same for all detected particles. These variables are from the GPID bank and introduced and described in more detail in Section 3.6.2.

3.3.2 Proton and Pion Selection

The reaction channel of interest in this analysis is $\gamma p \to p\pi^+\pi^-$ and the photon energy for each event is selected according to the procedure outlined in Section 3.3.1. In the next step, the identification of the proton, π^+, and π^- as the final-state particles of $\gamma p \to p\pi^+\pi^-$ is needed. The GPID bank contains the CLAS-measured momentum of a particle and a theoretical β_c value for that particle can be calculated from the measured momentum. This theoretically calculated β_c value for all

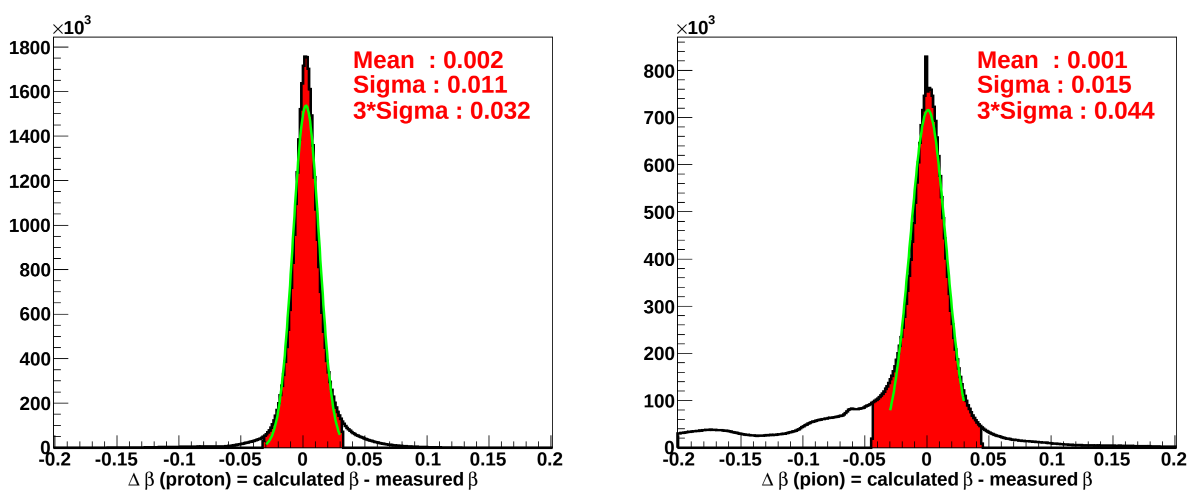

(a) $\Delta\beta$ (proton) (b) $\Delta\beta$ (pions)

Figure 2: Distribution of $\Delta\beta = \beta_c - \beta_m$ made from protons (a) and pions (plus and minus) (b), where β_c is calculated based on the particle's assumed mass. Events of the center peak filled in red are selected after applying the $|\beta_c - \beta_m| \leq 3\sigma$ cut.

possible hadron particle types is compared to the CLAS-measured empirical β_m value. Particle identification then proceeds by matching the calculated β_c closest to the empirical measured β_m. Figure 2 shows the difference, $\Delta\beta$, between the calculated β_c and the measured β_m. Assuming mass m for the particle, $\Delta\beta$ is given by:

$$\Delta\beta = \beta_c - \beta_m = \sqrt{\frac{p^2}{m^2 + p^2}} - \beta_m \,. \tag{5}$$

The peak around $\Delta\beta = 0$ shown in Figure 2 corresponds to the particles of interest. $\Delta\beta$ for the pions in Figure 2 (b) is broader than for the proton in Figure 2 (a) and there is a long tail to negative values of $\Delta\beta$ for the pions. When the GPID bank is made during the reconstruction, electrons are not separated from pions within the data. The long tail in the $\Delta\beta$ distribution for the pions represents electrons that need to be filtered out. To identify the proton and pions, a $|\beta_c - \beta_m|$ cut has been applied. This cut can be determined by fitting the main peak near $\Delta\beta = 0$ with a gaussian, discarding all events outside 3σ, where σ is the width of the fitted gaussian. Thus, any events with a value of $\Delta\beta$ greater than 0.032 for the proton and 0.044 for the pions are filtered out of the dataset. Figure 3 shows the measured momentum (p) versus the empirical measured β_m for protons and pions before (a) and after (b) applying the $|\beta_c - \beta_m|$ cut. Due to the different rest masses, bands for pions and protons are clearly visible, especially after applying the $|\beta_c - \beta_m|$ cut, and protons and pions are well identified.

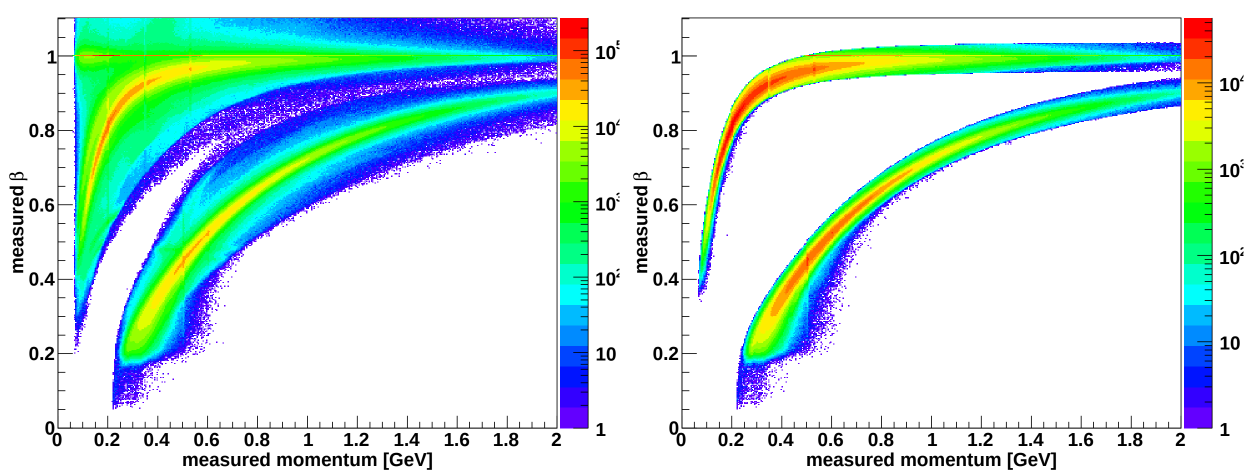

(a) Before applying the $\Delta\beta$ cut

(b) After applying the $\Delta\beta$ cut

Figure 3: (a) Measured β_m versus the measured momentum for the double-pion photoproduction events read from GPID on a logarithmic color scale. Notice the stripes for pions at the top, followed by protons. (b) Measured β_m versus the measured momentum after applying the cut based on the difference $\Delta\beta = \beta_c - \beta_m$. Clean pion and proton bands are clearly visible after applying the cut.

3.4 Kinematic Fitting

The reconstruction process determines the 4-vectors of the final-state particles. Kinematic fitting [6] modifies these 4-vectors by imposing energy-momentum conservation on the event as a physical constraint. All components of the Lorentz 4-vectors and the photon energy are modified until the event satisfies energy-momentum conservation exactly, and then the kinematically fitted event has several quantities to inspect the quality of the kinematic fitting: a confidence level and pull values for each measured quantity. The confidence level is used to estimate the goodness-of-fit. The pull distributions are used to evaluate the quality of the error estimation and check for systematics.

3.4.1 Confidence Level

After performing the fit, we need a way to check the agreement between the data and the hypothesis. The confidence level used as the primary method of the goodness-of-fit of an event is defined as:

$$CL = \int_{\chi^2}^{\infty} f(z;n)dz \,, \tag{6}$$

where $f(z;n)$ is the χ^2 probability density function with n degrees of freedom. It denotes the probability that a given event fullfills the constraint imposed on the event kinematics, e.g. energy-momentum conservation. In the ideal case of independent variables and gaussian errors, the confidence-level distributions of the events (without background) is flat and ranges from 0 to 1. However, the real data produce confidence level distributions which have a sharp rise nero zero. The large number of events with low confidence level values represents events that do not satisfy well the imposed constraints. These events include background events, poorly reconstructed events, or events with misidentified particles. Cutting out events with low confidence levels provides a reasonable way to eliminate the majority of the background while losing a relatively small amount of good events.

3.4.2 Pulls

To effectively use the confidence level to cut out background events, a good understanding of each fit quantity's error is needed. The quality of the error estimation can be obtained by examining the pull distributions. All fit parameters for every detected final-state particle have pull distributions. A pull is a measure of how much and in what direction the kinematic fitter has to alter the measured parameters. The pull value for the i^{th} fit quantity is given by:

$$z_i \;=\; \frac{\epsilon_i}{\sigma(\epsilon_i)} \,, \tag{7}$$

where $\epsilon_i \;=\; \eta_i - y_i$ is the difference between the fit value of the i^{th} parameter, η_i, and the measured value of the i^{th} parameter, y_i. The quantity σ represents the standard deviation of the parameter ϵ_i. Therefore, the i^{th} pull can be written as:

$$z_i \;=\; \frac{\eta_i - y_i}{\sqrt{\sigma^2(\eta_i) - \sigma^2(y_i)}} \,. \tag{8}$$

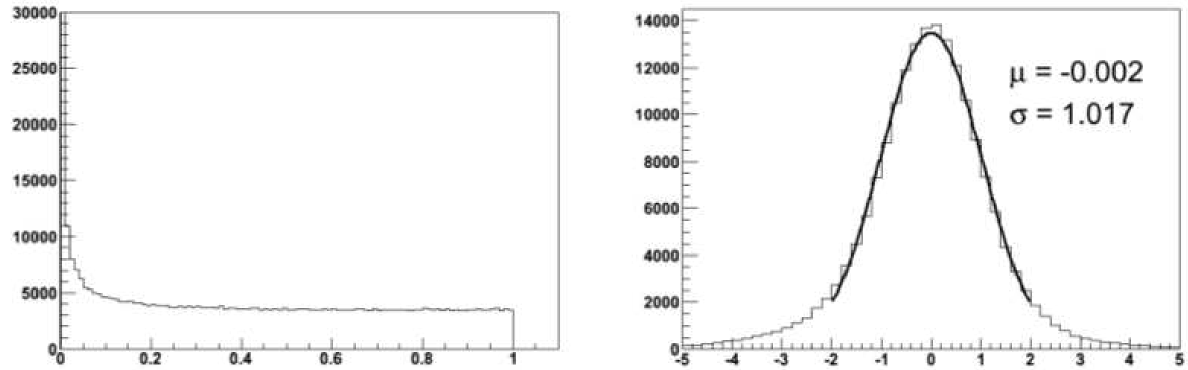

(a) Confidence Level Distribution (b) Pull Distribution

Figure 4: Example of fit results coming from a fit to a fully reconstructed $\gamma p \rightarrow p\pi^+\pi^-$ final state. (a) Shows an example of a confidence level distribution. A confidence level distribution (working with real data) peaks toward zero but flattens out toward one. (b) Shows an example of a pull distribution (the photon energy pull). Ideally, a pull distribution is gaussian in shape around the origin with a mean (μ) of zero and a sigma (σ) of one.

The reaction channel $\gamma p \rightarrow p\pi^+\pi^-$ has three final-state particles: proton, π^+, and π^-. There are three fit parameters for each particle in the kinematic fitting: a momentum and two angles, λ and ϕ. Thus, this analysis has ten pull distributions including a pull for the photon energy if all particles in the final state are detected. Assuming that the errors of the parameters used for kinematic fitting are properly determined and all systematic errors have been corrected, the distribution of the pull values (z_i values) will be gaussian in shape with a width of one ($\sigma = 1$) and a mean value of zero ($\mu = 0$); an example is shown in Figure 4. A systematic error in the quantity η_i can be seen as an overall shift in the distribution of the corresponding z_i away from zero. Similarly, if the error of η_i has been consistently (overestimated) underestimated, then the corresponding pull distribution will be too (narrow) broad. The error of the measured value η_i can be corrected from the pull distribution in an iterative procedure. Kinematic fitting provides an effective tool also to determine corrections to the particles' energies and momenta. This will be discribed in the following sections.

3.5 Corrections

3.5.1 Enery Loss (ELoss) Correction

As charged particles from the decay of a resonance travel from the target cell to the Drift Chambers of CLAS, they lose energy through atomic excitations or ionizations when interacting with the three kinds of targets, target walls, support structures, beam pipe, Start Counter, and the air gap between the Start Counter and the Region 1 Drift Chambers. Therefore, the reconstructed momentum seen in the Drift Chambers is actually less than the momentum of the particle at the production vertex. To account and correct for this, the 4-vectors of the final-state particles taken from the data were corrected event-by-event using the ELoss package developed for charged particles

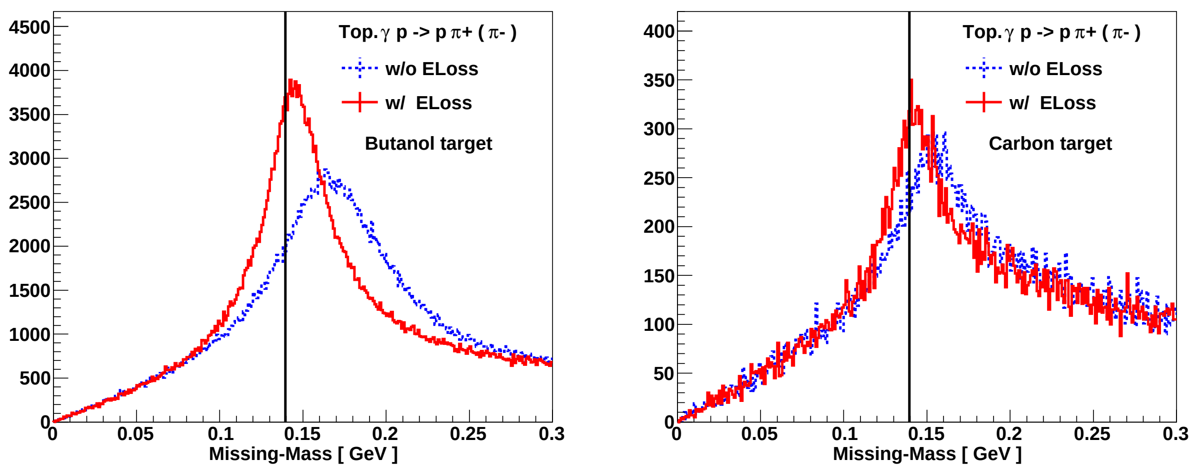

(a) Butanol target (b) Carbon target

Figure 5: Missing-mass distributions before (dotted blue histogram) and after (solid red histogram) applying energy-loss corrections in the Topology $\gamma p \to p\pi^+(\pi^-)$ from the butanol target (a) and carbon target (b). The vertical lines denote the mass of the π^-. The energy-loss corrections make the peak shape noticeably narrower and the peak position is also corrected. However, the peak is not positioned exactly at the π^- mass, so further corrections are needed.

moving through CLAS [7]. This ELoss package calculates the lost momentum of each particle in several materials which the charged particle has interacted with. To perform this calculation, the particle's 4-momentum measured by the Region 1 of the Drift Chamber is used to track the particle back to the reaction vertex in the target cell. As the particle is tracked back to the reaction vertex, the materials and distances it traverses are taken into account and the energy loss of the detected particle is also calculated. The 4-vector of the particle is corrected by multiplying an ELoss correction factor to the momentum of this vector:

$$\begin{aligned} P_{(\,p\,,\,\mathrm{ELoss}\,)} &= \eta_p \,\cdot P_{(\,p\,,\,\mathrm{CLAS}\,)} \\ P_{(\,\pi^+\,,\,\mathrm{ELoss}\,)} &= \eta_{\pi^+} \,\cdot P_{(\,\pi^+\,,\,\mathrm{CLAS}\,)} \\ P_{(\,\pi^-\,,\,\mathrm{ELoss}\,)} &= \eta_{\pi^-} \,\cdot P_{(\,\pi^-\,,\,\mathrm{CLAS}\,)}\,, \end{aligned} \tag{9}$$

where $P_{(\,x\,,\,\mathrm{ELoss}\,)}$ is the momentum of the particle x after applying the energy loss correction, $P_{(\,x\,,\,\mathrm{CLAS}\,)}$ is the raw momentum measured in CLAS and x is either the proton, π^+, or π^-. The parameters η_p, η_{π^+}, and η_{π^-} are the correction factors of the energy loss correction. The energy-loss corrected 4-vectors are then used in the analysis with the corrections being of the order of a few MeV. The energy loss correction produces a shift in mass as can be seen for the missing-mass calculations in Figure 5.

3.5.2 Photon Beam Correction

The energy of the photons that are incident on the target is determined in the Hall B tagging system. The photon energy measured in this tagging system should be also checked for consistency with the final state after applying the energy loss correction described in Section 3.5.1. It has been seen in past experiments that a physical sagging of the support structures of the E-counter scintillator bars in the tagger hodoscope could be attributed to gravitational forces [8]. The consequence of this sagging is a misalignment of the scintillator bars which leads to a mis-measurement of the scattered electron's energy [9]. In the g9a experiment, this sagging problem has been already partially corrected when the data were reconstructed. However, whether the sagging problem still persists in the g9a dataset should be checked and minor corrections need to be applied to the photon beam if necessary.

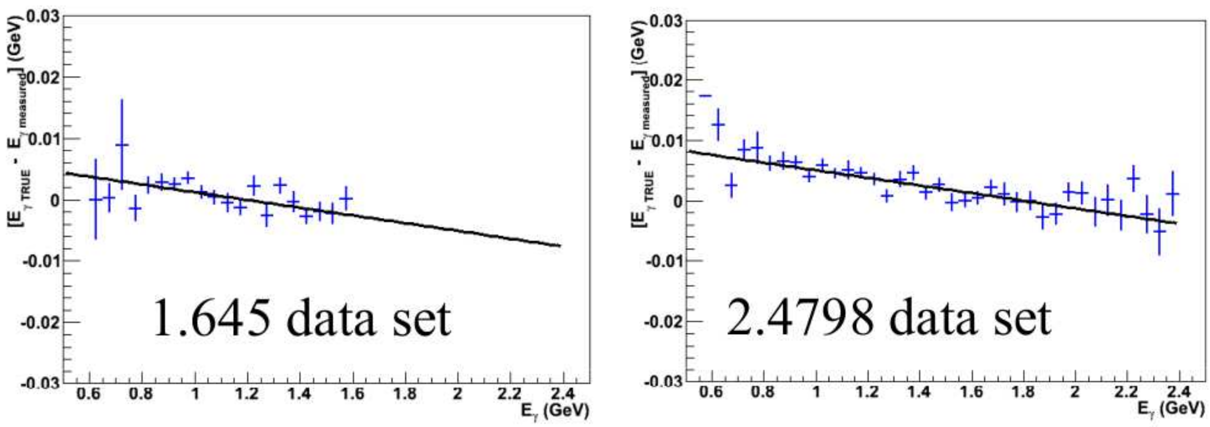

(a) $E_{e^-} = 1.645$ GeV dataset

(b) $E_{e^-} = 2.478$ GeV dataset

Figure 6: Initial photon-beam correction developed at ASU for the $E_{e^-} = 1.645$ GeV dataset (a) and $E_{e^-} = 2.478$ GeV dataset (b). $E_{\gamma\,measured}$ is the measured photon energy from the data [10], whereas $E_{\gamma\,TRUE}$ is the assumed correct photon energy applying the simple ansatz $E_{\gamma\,TRUE} = \alpha_\gamma\, E_{\gamma\,Tagger}$.

The photon beam energy can be calculated from the particles' information in the reaction $\gamma p \to p\pi^+\pi^-$ using energy and momentum conservation:

$$E_{(\,cal.\gamma\,)} = \sqrt{m_p^2 + P^2_{(\,p\,,\mathrm{ELoss}\,)}} + \sqrt{m_{\pi^+}^2 + P^2_{(\,\pi^+\,,\mathrm{ELoss}\,)}} + \sqrt{m_{\pi^-}^2 + P^2_{(\,\pi^-\,,\mathrm{ELoss}\,)}} - m_p\,, \quad (10)$$

where $P_{(\,p\,,\mathrm{ELoss}\,)}$, $P_{(\,\pi^+\,,\mathrm{ELoss}\,)}$ and $P_{(\,\pi^-\,,\mathrm{ELoss}\,)}$ are the ELoss-corrected momenta of the final particles (Equation 9). The status of the photon beam energy can be checked by comparing the calculated photon energy, $E_{cal.\,\gamma}$, from Equation 10 with the measured photon energy, $E_{mea.\,\gamma}$, from the g9a dataset.

The initial photon beam correction was developed by Michael Dugger (Arizona State University) [10] and was given by:

$$E_{out} = E_{in} + a_1 \cdot E_{in} + a_0 \cdot E_{e^-}\,, \qquad \text{with} \qquad \begin{aligned} a_0 &= 0.00456797 \\ a_1 &= \text{-}0.00630536\,, \end{aligned} \quad (11)$$

where E_{in} is the photon energy before the correction and E_{out} is the photon energy after the ASU correction (Figure 6). E_{e^-} is the electron beam energy used in this analysis. Figure 7 shows the comparison of the calculated photon energy, $E_{cal.\,\gamma}$, to the measured photon energy, $E_{mea.\,\gamma}$, after

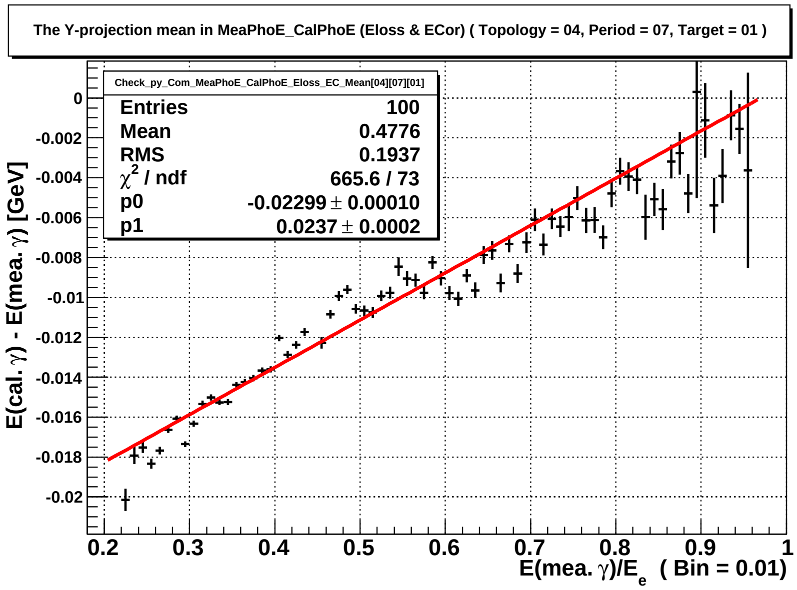

Figure 7: The difference between the calculated photon energy $E_{cal.\gamma}$ and measured photon energy $E_{mea.\gamma}$ after applying the ASU photon beam correction.

applying the ASU photon correction. At low energies, there is an overall shift in the distribution of the corresponding energy difference away from zero: the measured photon energy is bigger than the calculated photon energy. The ASU photon energy correction needs to be supplemented and was improved by Sungkyun Park (Florida State University) in this analysis by using the fit shown in Figure 7. The additional FSU photon energy correction is given by:

$$E_{out} = \left(a_1 \cdot E_{in} + a_0 \cdot E_e\right) \cdot \left(1 + \frac{p_1}{E_e}\right) + p_0 \,. \tag{12}$$

Target	p_0	p_1
butanol	-0.02299	0.0237
carbon	-0.01533	0.02012
polyethylene	-0.01539	0.02413

Table 3: The parameters used in the FSU photon beam correction.

The three kinds of targets have different values for the parameters, p_0, p_1, and p_2, shown in Table 3. The parameters a_1 and a_2 are from Equation 11. E_{out} is the photon energy after applying the final photon energy correction. After the photon beam correction has been applied to the photon energy measured in the CLAS spectrometer, we can compare the difference between the calculated and measured photon energy. This is shown in Figure 8. After applying energy-loss and the photon beam correction, 4-vectors of the final-state particles and the photon beam energy are corrected very well except for the regions of very high and low energies.

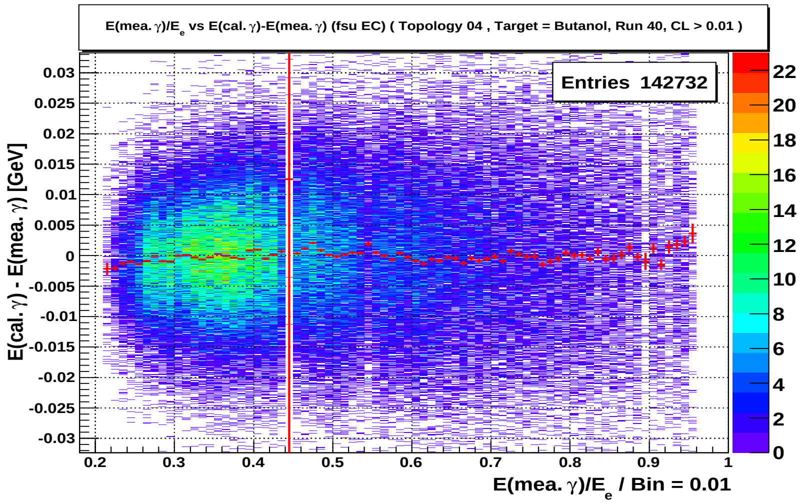

Figure 8: The difference between the calculated photon energy, $E_{cal.\,\gamma}$, and measured photon energy, $E_{mea.\,\gamma}$, after applying energy-loss correction and all photon-beam corrections. This figure is made from the Topology $\gamma p \to p\pi^+\pi^-$ with no missing mass and data from the butanol target. On the x-axis, E_{e^-} is the electron beam energy used in the g9a experiment. As the tagging system of the Hall-B can tag photon energies from 20 % to 95 % of the incident electron beam energy, the data on the x-axis cover a range from 0.2 to 0.95.

3.5.3 Momentum Correction

Since the CLAS spectrometer used in the g9a experiment is not a perfect detector, corrections must be determined also for the particles' momenta. The reason is mainly a result of unknown variations in the magnetic field provided by the Torus Magnet as well as inefficiencies and misalignments of the Drift Chambers. The momentum corrections in the g9a experiment were determined using the kinematic fitter.

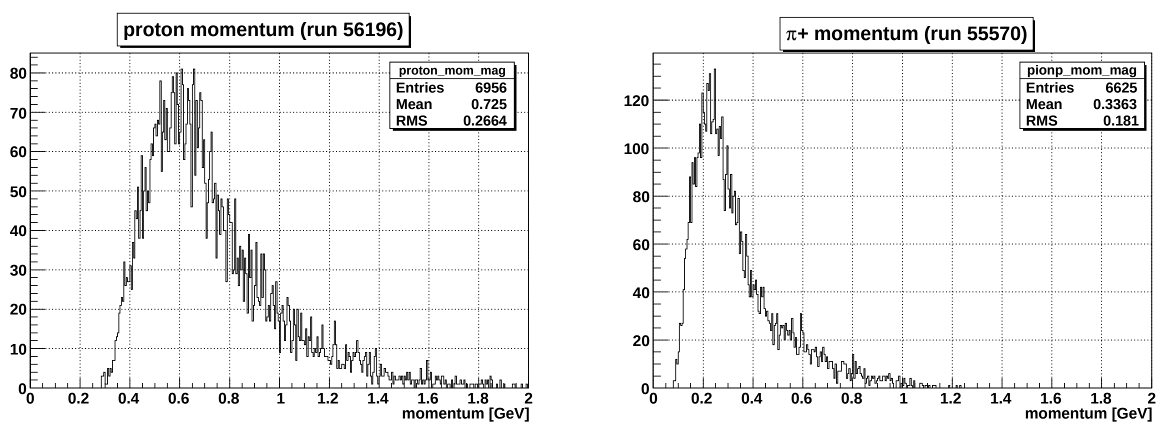

(a) Protons (b) Pions

Figure 9: Examples of momentum distributions of final-state particles in the g9a dataset.

To properly determine correction factors for the momentum, pull distributions must be evaluated for different momentum bins. The binning of the momentum was determined based upon the observed distributions of the proton and pion momenta shown in Figure 9. The momentum binning utilized five momentum bins, which are shown in Table 4.

particle	momentum bin	range [GeV]	correction factor
proton	1	0.2 - 0.5	1.012011
	2	0.5 - 0.6	1.002014
	3	0.6 - 0.7	0.999716
	4	0.7 - 0.9	1.000439
	5	0.9 - 1.7	0.999975
π^+	1	0.05 - 0.2	1.005510
	2	0.20 - 0.27	0.998049
	3	0.27 - 0.35	0.998151
	4	0.35 - 0.53	1.000716
	5	0.53 - 1.40	1.001858
π^-	1	0.05 - 0.2	1.018893
	2	0.20 - 0.27	0.987956
	3	0.27 - 0.35	0.986561
	4	0.35 - 0.53	1.010072
	5	0.53 - 1.40	0.992872

Table 4: The momentum binning of the proton and pions for the momentum corrections and the correction factors applied in this analysis.

The final goal of the momentum corrections is to obtain pull distributions, which are gaussian in shape with $\sigma = 1$ and mean $= 0$. Only small correction factors are applied to the momenta to adjust the positions of the pull distributions. This iterative process is repeated until the pull distributions for proton, π^+, and π^- are centered at zero with a symmetric shape. Pull distributions and the confidence-level distribution after applying the energy-loss correction, the photon-beam correction, and the momentum corrections are shown in Figure 10. Means and sigmas of these pull distributions are acquired by fitting pull distributions with all corrections to a gaussian curve and are shown in Table 5.

	proton			π^+			π^-			photon
	mom	λ	ϕ	mom	λ	ϕ	mom	λ	ϕ	
mean	-0.012	$+0.205$	-0.050	-0.086	$+0.099$	-0.098	-0.090	-0.371	-0.085	$+0.088$
σ	1.029	0.983	0.991	1.002	1.004	0.990	1.023	0.976	0.987	1.035

Table 5: Means and σ's of pull distributions integrated over all momentum bins used for momentum corrections (Table 4) after applying all corrections.

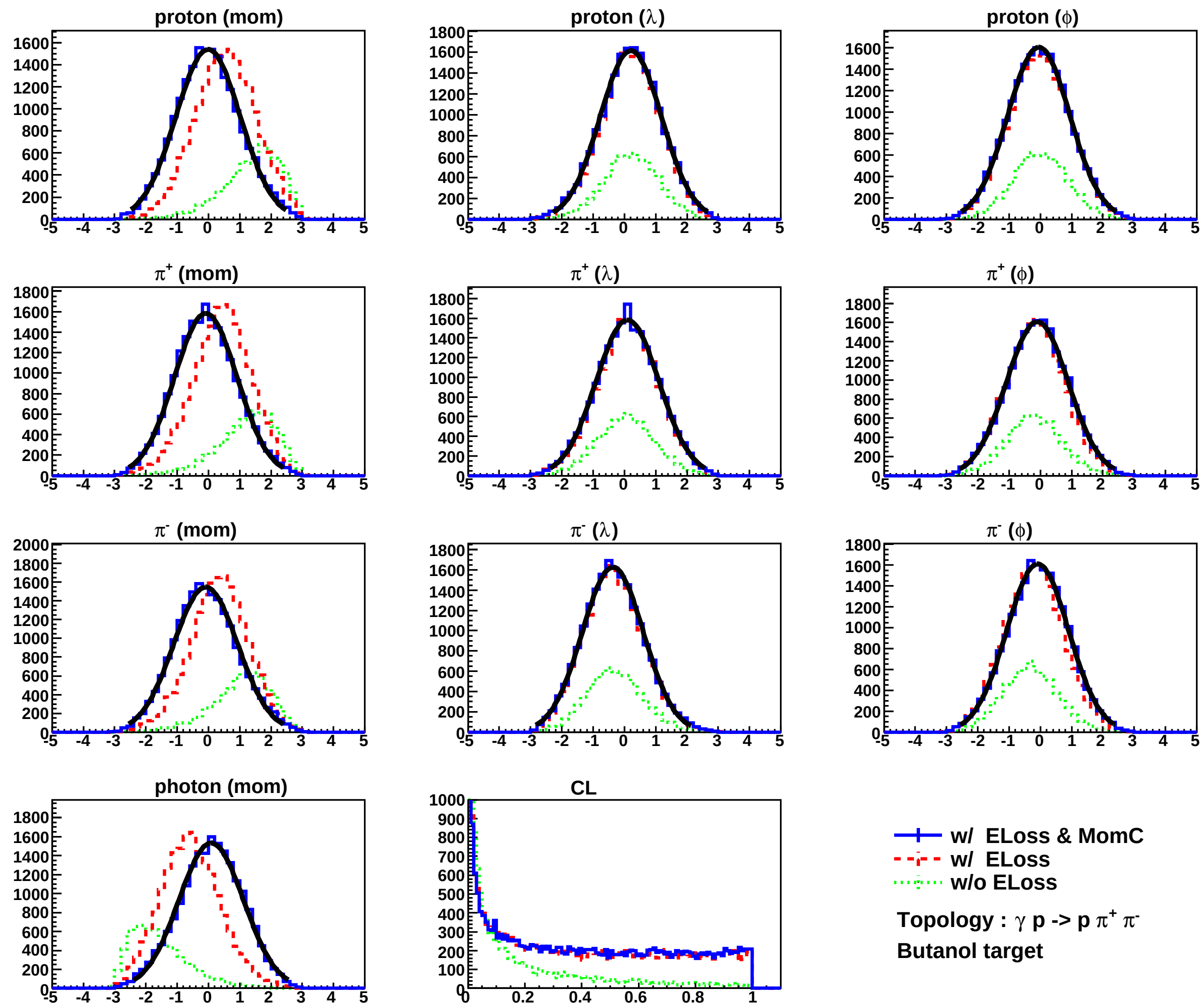

Figure 10: Pull and confidence-level distributions after applying all corrections to the data from the butanol target. The green dotted line is made from the raw data. After the energy-loss correction is applied to the raw data, the red dashed line is obtained. One after another, photon-beam correction and momentum corrections are applied on the dataset and the blue solid histograms are obtained. These pull and the confidence-level distributions are from Topology 4, $\gamma p \to p\pi^+\pi^-$, with a 5 % confidence-level cut applied. The lines represent gaussian fits to the data; the mean and σ of the fits can be found in Table 5.

3.6 Basic Cuts

The events of all four topologies were kinematically fitted after applying all corrections. In the next step, it is necessary to impose a series of cuts before extracting polarization observables. These cuts will serve to further refine the data sample and help remove events with accidental particles and other things that corrupt the dataset.

3.6.1 Vertex Cut

The g9a experiment has three kinds of targets such as a butanol, carbon, and polyethylene target. The butanol target is 5 cm long and 3 cm in diameter with its center located at the center of the CLAS spectrometer. The carbon target is located at 6 cm from the CLAS center downstream with 0.15 cm in length. The polyethylene target is located at 16 cm from the CLAS center downstream with 0.35 cm in length. The applied vertex cuts therefore are: $-3\,\text{cm} < z_{\text{all particles}} < +3\,\text{cm}$ for the butanol target, $+5\,\text{cm} < z_{\text{all particles}} < +7.5\,\text{cm}$ for the carbon target, and $+15\,\text{cm} < z_{\text{all particles}} < +18\,\text{cm}$ for the polyethylene target. The vertex cut involving the x- and y-components selects those events, which originated no more than 2 cm from the z axis (beam line).

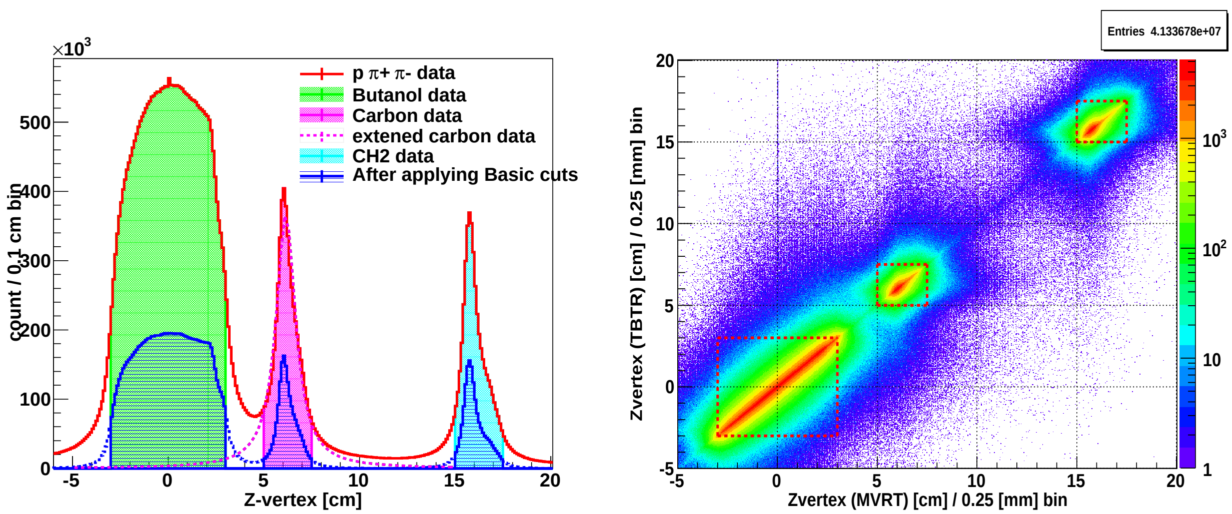

(a) z-vertex (MVRT) (b) z-vertex (MVRT) vs. z-vertex (TBTR)

Figure 11: (a) The vertex z-position (axis along the beam line) of all reconstructed particles showing the positions of the three kinds of targets. The red line denotes the data with all $p\pi^+\pi^-$ events. The blue line denotes events after applying basic cuts. The carbon data with all $p\pi^+\pi^-$ events is fitted with a Breit-Wigner to check the distribution of carbon events. (b) A comparison of the z-vertex reconstruction from the MVRT and TBTR bank is shown on a log-z color scale. Lines indicating the target cut regions are shown in the dashed red boxes.

Since the vertex distributions of the butanol and carbon targets are very close as shown in Figure 11 (a), the overlap between both targets needs to be checked. To study the contamination of the butanol events with carbon events, the total distribution of the carbon data with all $p\pi^+\pi^-$

events has been fitted with a Breit-Wigner function. We observe very little interference of the carbon events with the butanol data. After applying basic cuts, the butanol and carbon events are clearly distinguished and the contamination due to carbon events in the butanol target is negligible.

The vertex information in this analysis can be taken from either of the two banks, TBTR or MVRT. The difference of the vertex information between the TBTR and MVRT bank comes from the number of particles used to reconstruct the vertex. The reconstruction from the TBTR bank uses the vertex position for a particle based solely on CLAS information for the particle, whereas the MVRT bank assigns a single vertex from the tracking information of all available charged particles in the event to calculate the best estimate for the vertex location. The MVRT vertex reconstruction is usually more accurate than the TBTR vertex when there are multiple tracks like in double-pion photoproduction since more tracks included in the reconstruction of the vertex location will determine the vertex with a higher degree of accuracy. In an ideal situation, both TBTR and MVRT vertex would give identical results, which seems to be a good approximation when looking at the vertex information for the entire dataset, shown in Figure 11 (b). This plot shows single thin straight lines with $V_z(TBTR) = V_z(MVRT)$ as expected in the ideal situation. This analysis uses the vertex information from the MVRT bank.

3.6.2 Accidental Cuts

Accidental events can occur as a result of a number of factors, such as human error, detector error, natural events (e.g. cosmic ray), or a combination of these. Cuts imposed on the g9a dataset during this analysis to remove the accidental events use specific bank variables. These variables can be found in the GPID bank [5] with the names NGRF and TAGRID and corresponding distributions are shown in Figure 12.

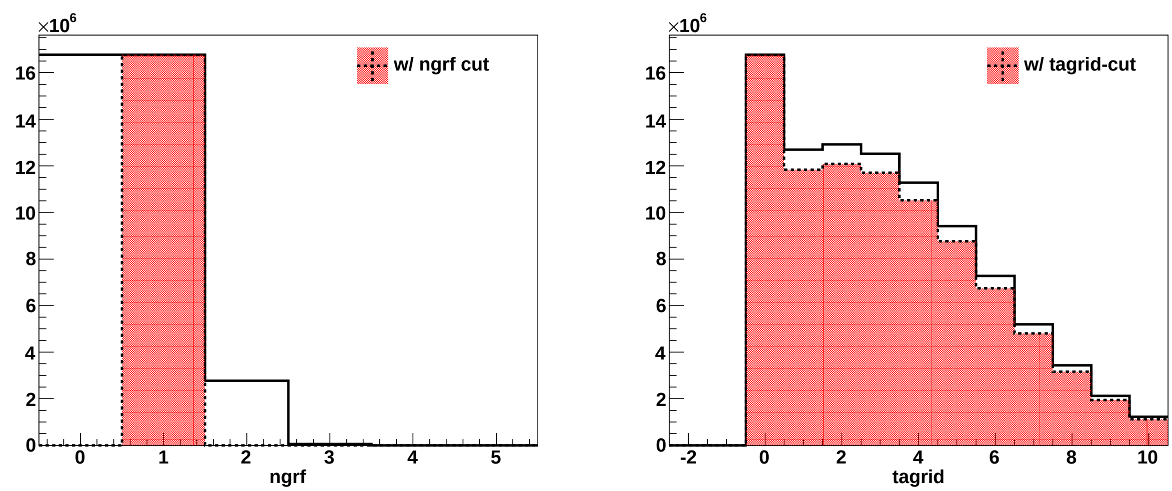

Figure 12: The distributions of the variables NGRF and TAGRID used in the g9a experiment.

The NGRF variable indicates how many candidate photons were found in the reconstruction, which passed the reconstruction timing cut to find the incident photon. The TAGRID provides an index to the location of the photon related to a particle in the TAGR bank. The NGRF cut imposed on all final-state particles requires that they all have a value of one (NGRF=1). This means that for every final-state particle, there was only one photon found which meets the timing requirements. For the TAGRID cut, the requirement is that values of this variable for all final-state particles are the same and this guarantees that the reconstruction code found the same photon for all final-state particles. These accidental cuts ensure that the analyzed events have been subject to a successful determination of the incident photon and that this photon is the same for all final-state particles, thus leading to a well-defined initial state.

3.6.3 Confidence-Level Cut

By performing a cut on the confidence level, the background events, poorly reconstructed events as well as events with misidentified particles can be significantly removed from the g9a dataset. Figure 13 (a) shows the confidence-level distribution for the Topology $\gamma p \to p\pi^+(\pi^-)$ before and after applying the confidence-level cut of 5 % and Figure 13 (b) presents the missing-mass distribution before and after applying the confidence-level cut of 5 %. This confidence-level cut removes much of the background events while ideally only cutting out 5 % of the good events.

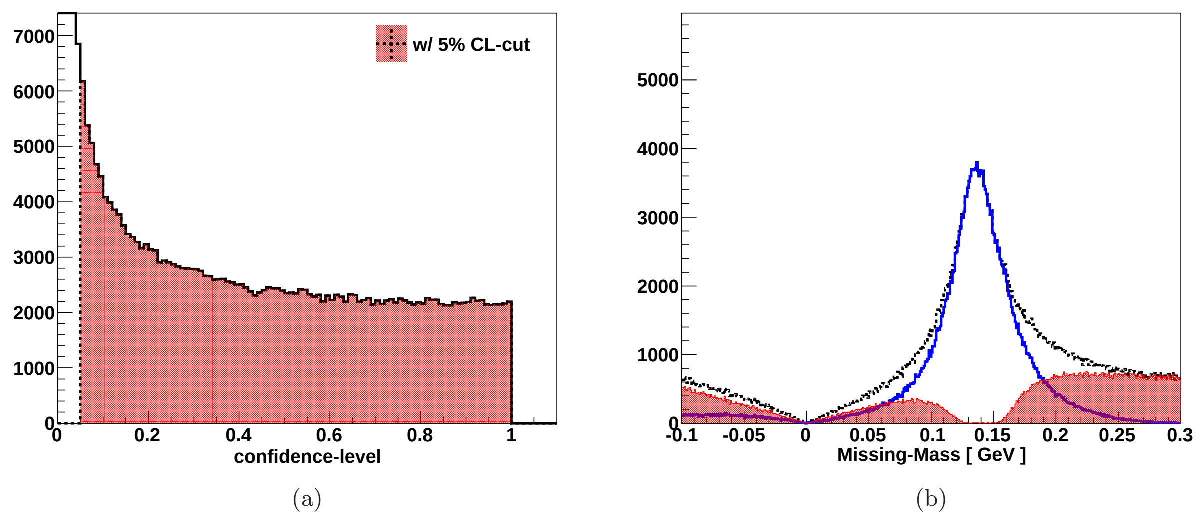

Figure 13: (a) The distribution of confidence-level values for the Topology $\gamma p \to p\pi^+(\pi^-)$ generated from the butanol target. The confidence-level cut selects the events whose confidence level is greater than 0.05 as shown in the colored region. (b) The missing-mass distribution made from the same topology and target as in Figure 13 (a). The black dashed line is made after applying all cuts and corrections without the confidence-level cut and the blue solid histogram indicates the good events after applying the confidence-level cut of 5 % on the black dashed histogram. The colored area includes events whose confidence level is less than 0.05.

3.6.4 Removing Bad Time-of-Flight Paddles

Since some TOF paddles of the CLAS spectrometer are dead or malfunctioning, the information from these bad TOF paddles should be removed from the g9a dataset. The number of counts for each scintillator paddle is plotted in Figure 14. The bad paddles are identified by comparing the TOF paddle with very low counts to the average value of the sectors. The identified bad TOF paddles are listed in Table 6.

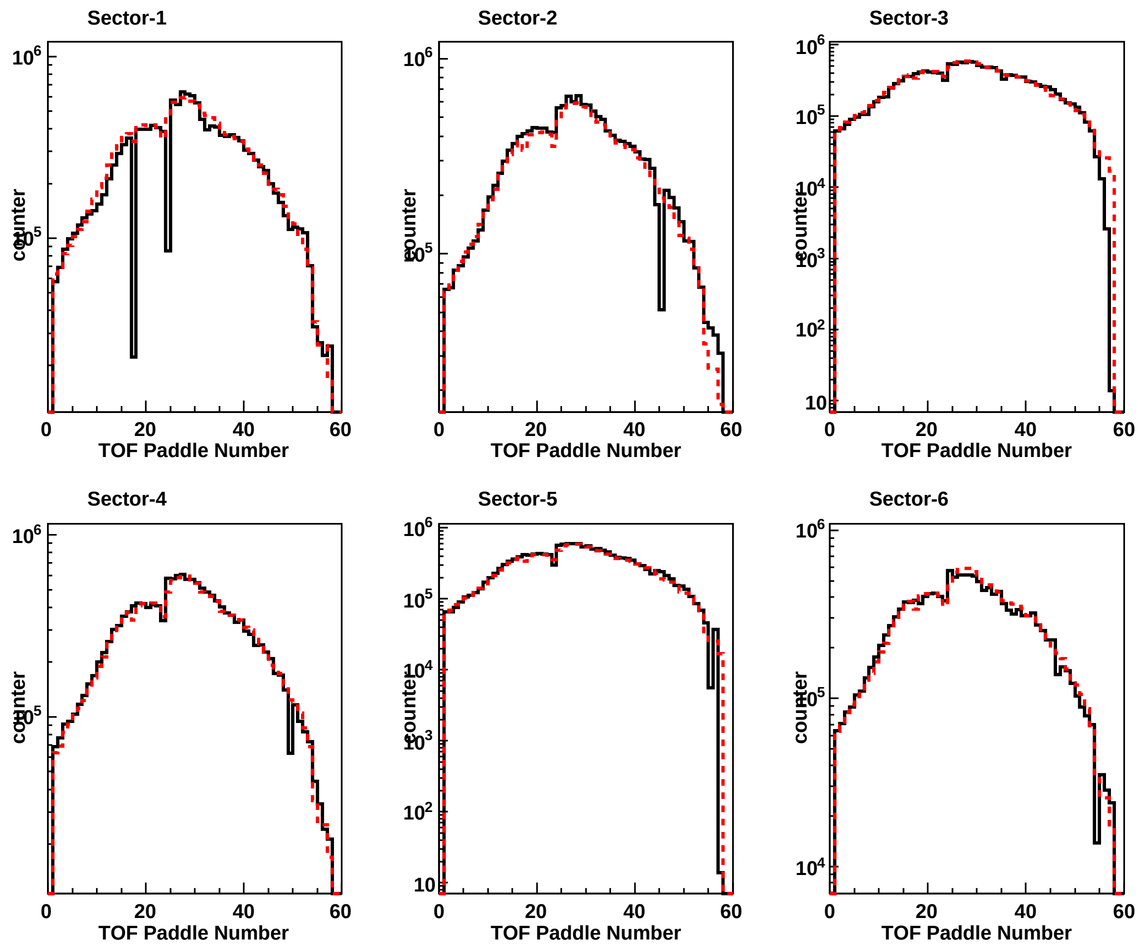

Figure 14: The TOF paddle hit distributions in the six sectors. The red dashed line is the average of the six sectors' counts in the paddle distribution.

3.6.5 Event Distributions after Applying all Cuts and Corrections

The process of developing and applying energy and momentum corrections during the course of an analysis serves the purpose of correcting for the effects of the experimental setup, therefore result-

sector number	bad TOF paddles
1	17, 24
2	45
3	23, 35
4	23, 49
5	23, 55
6	54

Table 6: The information of the bad time-of-flight paddles.

ing in a dataset that is as nature intended it. Additionally, determining and enforcing cuts used in an analysis serves not only to remove the remaining effects of the experimental setup but also to remove the contribution to the dataset from physics events not of interest to the analysis (the hadronic background). Figure 15 shows missing-mass distributions and a squared missing-mass distribution for the four kinds of topologies in the reaction $\gamma p \to p\pi^+\pi^-$, respectively. In this figure, missing-mass distributions after applying energy and momentum corrections to the 4-vectors are presented as well as the changes after applying all cuts with and without the confidence-level cut.

The remaining background may be comprised of accidental events where a detected particle was attributed to an event to which it does not belong, events with an incorrect initial state like a misidentification of a photon and events originating from interactions with matter other than the target materials. A typical method of observing the background is to choose a final-state topology and construct the missing mass of that topology, as shown in Figure 13 (b). A single cut on the confidence level greatly reduces this background but does not entirely remove it. Through the application of the proper vertex position, photon and particles identification variables, this background may be reduced even further. Because the g9a experiment uses a “dirty” polarized target (about 86.5 % of the nucleons in butanol are from carbon and oxygen), the free-proton events from the butanol – after removing some of the background – still have contributions from bound nucleons. These bound-nucleon contributions still need to be taken care of.

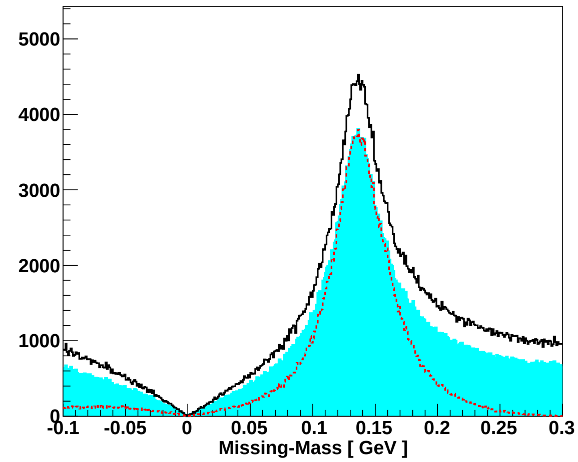

(a) Topology 1: $\gamma\, p \to\, p\, \pi^+ (\pi^-)$

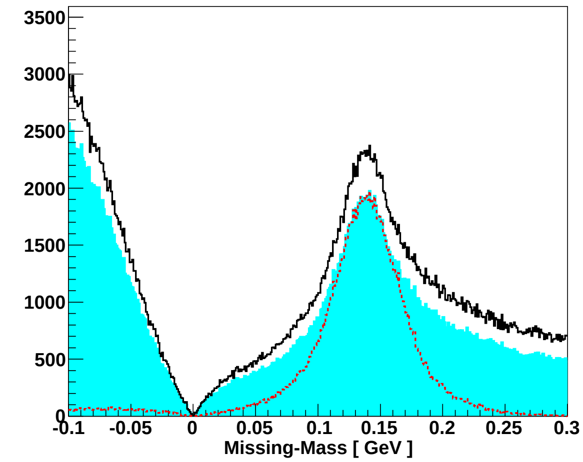

(b) Topology 2: $\gamma\, p \to\, p\, \pi^- (\pi^+)$

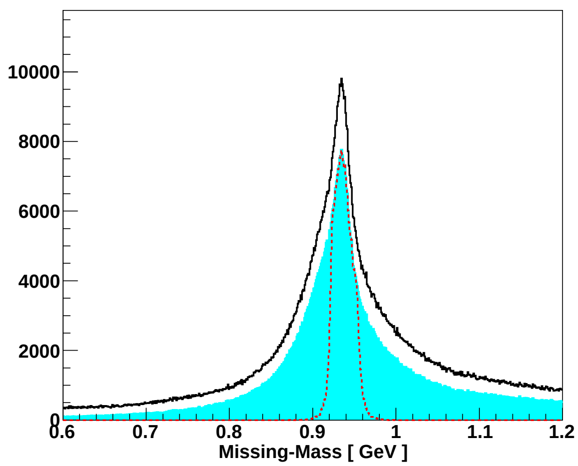

(c) Topology 3: $\gamma\, p \to\, \pi^+ \pi^- (p)$

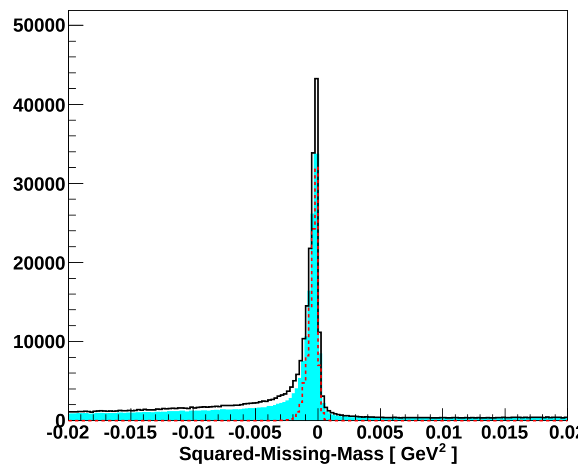

(d) Topology 4: $\gamma\, p \to\, p\, \pi^+ \pi^-$

Figure 15: Missing-mass distributions for the four different topologies. The π^- particle is missing in all events (a), the π^+ particle is missing (b), the proton is missing (c), and no particle is missing (d). The black solid line is made from the butanol target after applying all corrections. The histogram filled in light blue indicates the good events after applying all basic and accidental cuts and corrections without the confidence-level cut. The red dashed histogram includes events whose confidence level is greater than 0.05. The distribution in (d) is made as a function of the squared missing mass.

3.7 Beam and Target Polarization

3.7.1 Photon Beam Polarization

Circularly-polarized photons are produced via bremsstrahlung of longitudinally-polarized electrons from an amorphous radiator. The degree of circular polarization of the bremsstrahlung photons, $\delta_{\odot}$, can be calculated from the longitudinal polarization of the electron beam, δ_{e^-}, multiplied by a numerical factor. In particular, with $x = E_\gamma/E_e$, the degree of circular polarization of bremsstrahlung photons from longitudinally-polarized electrons is given by [11]:

$$\delta_{\odot} = \delta_e \cdot \frac{4x - x^2}{4 - 4x + 3x^2} \,. \tag{13}$$

Figure 16, made from Equation 13, shows that the circular polarization of the photon beam and the photon beam energy are roughly proportional to each other. In the figure, the photon energy, E_γ, is given as a fraction of the electron-beam energy, E_{e^-}. The data using a circularly-polarized photon beam in the g9a experiment have two kinds of electron beam energies, 1.645 GeV and 2.478 GeV, shown in Table 1. Runs with different electron beam energies have different circular polarizations for the same photon energy E_γ. Thus, the circular polarization of the photon beam should be calculated separately in runs with different electron beam energies, as shown in Figure 17.

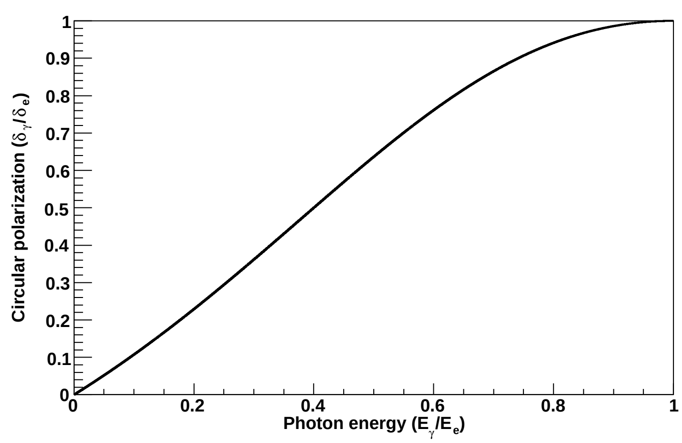

Figure 16: Circular polarization of the photon beam as a function of photon energy.

As the first step in calculating the degree of circular polarization of the photon beam, the longitudinal polarization of the electron beam, δ_{e^-}, must be found in runs with different electron beam energies. Table 7 summarizes the Møller measurements of the electron-beam polarization, δ_{e^-}, in the g9a experiment and their average values in runs with different electron beam energies. An average value of 84.798 % and 83.016 % with an uncertainty of 0.470 % and 0.789 %, respectively, is used for the degree of the electron-beam polarization, δ_{e^-}. Since the center-of-mass energy is used as an independent kinematic variable, the degree of circular polarization cannot be a continuous function.

Electron-beam energy E_{e^-}	Date	Run number	Electrom-beam polarization δ_{e^-}	Average
1.645 GeV	Nov. 12, 2007	55544	$+85.228 \pm 1.420$	84.789 ± 0.470
			-78.523 ± 1.350	
			-79.150 ± 1.26	
			$+88.700 \pm 1.480$	
	Nov. 13, 2007	55552	$+84.167 \pm 1.330$	
			-84.725 ± 1.530	
	Nov. 19, 2007	55588	-86.531 ± 1.380	
			$+88.409 \pm 1.440$	
			$+87.753 \pm 1.480$	
2.478 GeV	Nov. 28, 2007	55608	-82.534 ± 1.400	83.016 ± 0.789
	Nov. 28, 2007	55608	-79.450 ± 1.410	
			$+80.060 \pm 1.400$	
	Jan. 07, 2008	56194	-83.267 ± 1.380	
	Feb. 08, 2008	56202	-83.248 ± 1.320	

Table 7: Møller measurements of the electron-beam polarization.

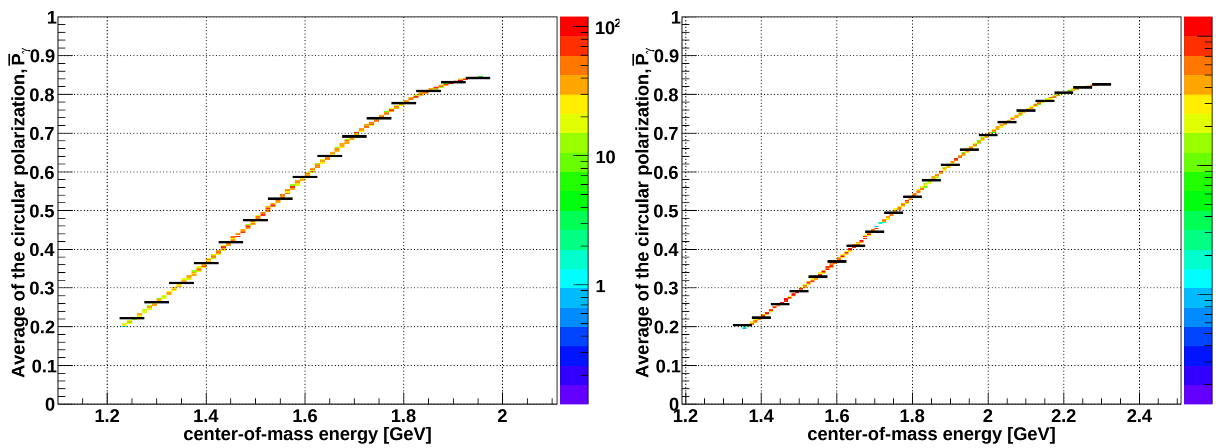

(a) $E_{e^-} = 1.645$ GeV

(b) $E_{e^-} = 2.427$ GeV

Figure 17: The average degree of circular polarization of the photon beam as a function of the center-of-mass energy for electron beam energies 1.645 GeV (a) and 2.427 GeV (b).

The average values of the circular polarization for a specific phase-space volume $\Delta\tau$ in each center-of-mass bin are given by:

$$\bar{\delta}_\odot = \frac{1}{N^+ + N^-} \sum_{i \in \Delta\tau} \delta_\odot(W)\,, \tag{14}$$

where $N^\pm$ are the total number of $\gamma p \to p\pi^+\pi^-$ events for the two helicity states and W is the center-of-mass energy; $\delta_\odot(W)$ is calculated from Equation 13. These average values are derived for each center-of-mass bin, shown in Table 8. Figure 17 shows the degree of circular polarization and their averages for the two electron beam energies, 1.645 GeV and 2.478 GeV.

The center of mass energy [GeV]	The average circular polarization, $\bar{\delta}_\odot$ $E_{e^-} = 1.645$ GeV	$E_{e^-} = 2.427$ GeV
1.25	0.22172 ± 0.00007	
1.30	0.26349 ± 0.00006	
1.35	0.31319 ± 0.00007	0.20442 ± 0.00019
1.40	0.36416 ± 0.00008	0.22325 ± 0.00007
1.45	0.41810 ± 0.00008	0.25841 ± 0.00008
1.50	0.47551 ± 0.00009	0.29194 ± 0.00010
1.55	0.53077 ± 0.00010	0.32929 ± 0.00010
1.60	0.58695 ± 0.00013	0.36861 ± 0.00012
1.65	0.64083 ± 0.00015	0.40909 ± 0.00014
1.70	0.69159 ± 0.00017	0.44555 ± 0.00021
1.75	0.73866 ± 0.00019	0.49416 ± 0.00020
1.80	0.77739 ± 0.00022	0.53564 ± 0.00022
1.85	0.80903 ± 0.00024	0.57837 ± 0.00031
1.90	0.83162 ± 0.00025	0.61849 ± 0.00029
1.95	0.84239 ± 0.00034	0.65746 ± 0.00031
2.00		0.69530 ± 0.00035
2.05		0.72835 ± 0.00037
2.10		0.75822 ± 0.00040
2.15		0.78291 ± 0.00045
2.20		0.80441 ± 0.00051
2.25		0.81792 ± 0.00059
2.30		0.82581 ± 0.00065

Table 8: The average degrees of circular polarization in FROST g9a.

3.7.2 Beam Charge Asymmetry

The electron beam polarization is toggled between the h^+ helicity state and the h^- helicity state at a 30 Hz rate. Therefore, the photon-beam flux for both helicity states should be identical on average. Small beam-charge asymmetries of the electron beam, however, can cause instrumental asymmetries in the observed $\gamma p \to p\pi^+\pi^-$ asymmetries, and need to be taken into account. This beam-charge asymmetry can be calculated by considering the luminosities for helicity-plus and helicity-minus events:

$$\Gamma^\pm = \alpha^\pm \Gamma = \frac{1}{2}(1 \pm \bar{a}_c)\Gamma\,, \tag{15}$$

where Γ is the total luminosity. The parameter $\alpha^\pm$ is used to find the helicity-plus and helicity-minus luminosities, $\Gamma^\pm$, from the total luminosity. This parameter depends on the mean value of the electron-beam charge asymmetry, $\bar{a}_c$. Figure 18 shows the beam-charge asymmetry, a_c, for the g9a runs used in this analysis. Their averages and errors calculated for different periods are shown in Table 9. These beam-charge asymmetries do not affect the final result of this analysis since these asymmetries are very small (see Appendix B).

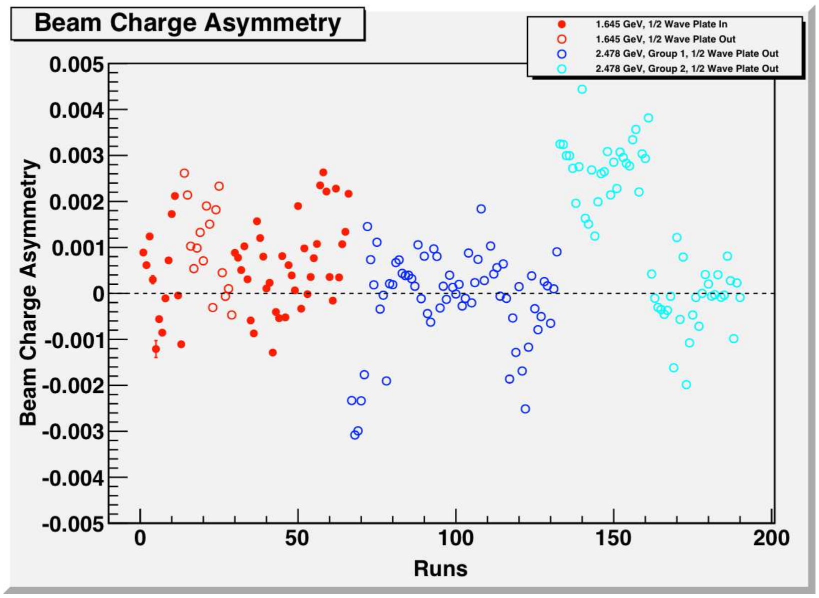

Figure 18: Distribution of beam-charge asymmetries for the analyzed runs.

Period	Average beam-charge asymmetry, $\bar{a}_c$	σ
1, 2, and 3	7×10^{-4}	1×10^{-3}
4 and 5	3×10^{-5}	3×10^{-3}
6 and 7	1×10^{-3}	4×10^{-3}

Table 9: The mean and error of the beam-charge asymmetries, $\bar{a}_c$, calculated in each period.

3.7.3 Target Polarization

The target polarization was determined by Josephine McAndrew (University of Edinburgh). The target polarization has the magnitude and the direction shown in Figure 19. The polarization direction is defined by two quantities: the direction of the holding magnetic field with respect to the beam and the direction of the proton polarization with respect to the holding field. Table 10 shows how the direction of the target polarization is defined in the FROST g9a experiment. The plus (minus) sign in the direction of the holding field indicates the field is parallel (anti-parallel) to the beam direction. The plus (minus) sign in the direction of the proton polarization indicates the protons are polarized parallel (anti-parallel) to the holding field. It turned out later that the directions of the target polarization between the NMR data and the run table are not consistent.

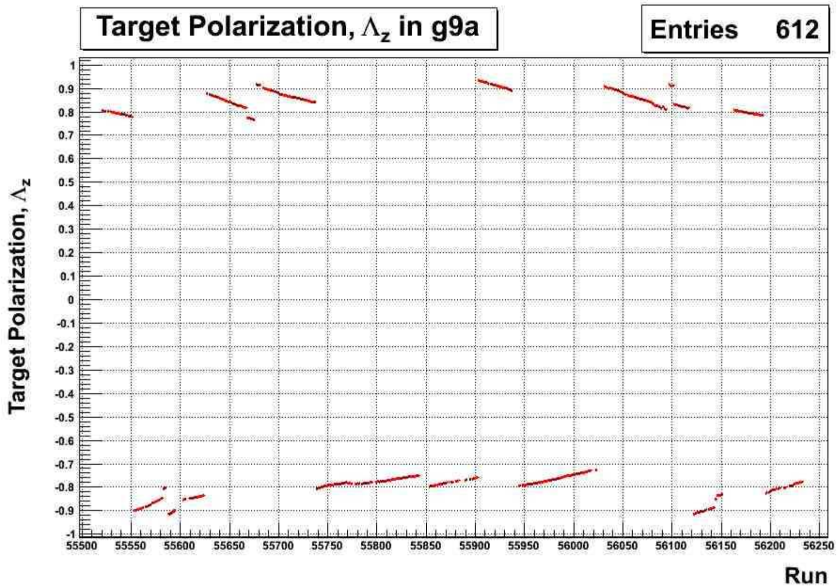

Figure 19: Target polarization versus run number measured in the g9a experiment.

L++ : Positive target polarization
L+− : Negative target polarization
L−+ : Negative target polarization
L−− : Positive target polarization

Table 10: The definition of the direction of the target polarization used in the g9a experiment. The first plus sign in L++ denotes the direction of the holding magnet and the second indicates the direction of the proton polarization.

The exact directions of the target polarization are determined from the target asymmetry in the reaction $\gamma p \to p\pi^+\pi^-$ based on the information in the run tables (see Appendix A). Table 11 shows the information of the direction of the target polarization before and after correcting the inconsistency using the target asymmetry. Each run has a different value of the target polarization and in order to be used in the asymmetry equation, average values per period must be calculated. Defining $\bar{\Lambda}_z$ as the mean value of the longitudinal target polarization, then:

$$\bar{\Lambda}_z^{\pm} = \frac{1}{N^{\pm}} \sum_{\text{run}} \Lambda_z^{\pm}(\text{run}) \,, \tag{16}$$

where $\pm$ denotes the target polarization is parallel/anti-parallel to the beam and $N^{\pm}$ is the total numbers of observed counts for the different target polarizations. Figure 20 shows the distribution of target polarizations used in the dataset for the circularly-polarized beam and longitudinally-polarized target. The average values are calculated by using Equation 16 and their mean values are listed in Table 12 with the statistical and systematic errors calculated using standard error propagation.

Period	The target polarization	
	Before the correction	After the correction
1	L+−(⇐)	⇐
2	L+−(⇐)	⇐
3	L++(⇒)	⇒
4	L−+(⇐)	⇒
5	L−−(⇒)	⇐
6	L++(⇒)	⇒
7	L+−(⇐)	⇐

Table 11: The direction of the target polarization before and after correcting initial inconsistencies. After the correction, the direction of the target polarization in Periods 4 and 5 is reversed. The arrow ⇒ (⇐) denotes the target polarization is parallel (anti-parallel) to the beam direction.

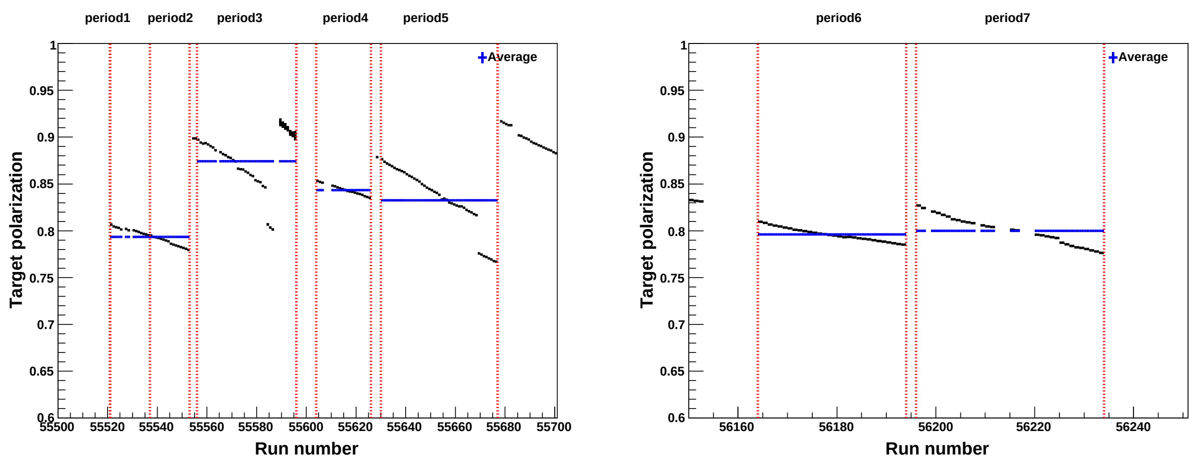

Figure 20: Values of target polarization versus run number measured in the g9a experiment and their averages (the blue line) calculated per period.

Period	Average target polarization			Ratio of target polarization		
	Λ_z	error		$\Lambda_z(=>)/\Lambda_z(<=)$	error	
		statistical	systematic		statistical	systematic
2	0.793444	4.50259e-05	0.00168486	1.10204	000359152	00235036
3	0.874406	0.000280614	0.000173592			
4	0.843431	5.16487e-05	0.000257478	1.01294	7.40223e-05	0.000363123
5	0.832656	3.32051e-05	0.000156484			
6	0.79606	3.0786e-05	0.000213638	0.995357	5.77651e-05	0.000378123
7	0.799774	3.46073e-05	0.000215037			

Table 12: Average values for the degree of target polarization including the statistical and systematic errors for each period and the ratio between the different target polarizations. This ratio of the different target polarization is later used in Equation 35.

3.7.4 Confirming the Orientation of the Beam and Target Polarization

In the next step, we should assure that the directions of the determined beam and target polarizations are credible. The direction of the target polarization is given in Table 11. The direction of the beam polarization depends on the condition of the half-wave plate (HWP): IN or OUT. The longitudinal polarization of the electron beam is flipped pseudo-randomly with 30 sequences of helicity (+,−) or (−,+) signals per second. Occasionally the HWP is inserted in the circularly-polarized laser beam of the electron gun to reverse helicities and the beam polarization phase should be changed by 180°. The HWP is inserted and removed at semi-regular intervals throughout the experimental run to ensure that no polarity-dependent bias is manifested in the measured asymmetries.

TGBI latch1	Beam helicity	
Bit 16	$\lambda/2$ (OUT)	$\lambda/2$ (IN)
1	+	−
0	−	+

Table 13: Helicity signal from the TGBI-bank latch1 for the two half-wave-plate positions. In the table, the sign +(−) means the beam polarization is parallel (anti-parallel) to the beam direction.

The electron-beam helicity information is stored in the level1-trigger-latch word of the TGBI bank. Bit 16 in the level1-trigger-latch word is the helicity-state bit. It indicates the sign of the electron-beam polarization as shown in Table 13. When the half-wave plate is OUT, the number 1 in Bit 16 of the level1-trigger latch means the beam polarization is parallel to the beam direction and the number 0 means the beam polarization is antiparallel to the beam. When the plate is IN, the directions of the beam polarization related to the numbers 1 and 0 are switched. Table 14 shows the information of the condition of the half-wave plate and the direction of the target polarization used in this analysis. The reliability of the information shown in Table 14 is confirmed by the beam and target asymmetries (see Appendix A).

Period	Run range	Beam polarization The condition of the half-wave plate	Target polarization
1	55521 - 55536	IN	$\Leftarrow$
2	55537 - 55555	OUT	$\Leftarrow$
3	55556 - 55595	IN	$\Rightarrow$
4	55604 - 55625	IN	$\Rightarrow$
5	55630 - 55678	IN	$\Leftarrow$
6	56164 - 56193	OUT	$\Rightarrow$
7	56196 - 56233	OUT	$\Leftarrow$

Table 14: The condition of the beam and target polarization of each period used in this analysis.

3.8 Normalization

As mentioned earlier, the g9a experimental data using the circularly-polarized beam can be divided into seven groups of runs with similar conditions called periods and each period has a different direction of the target polarization as shown in Table 14.

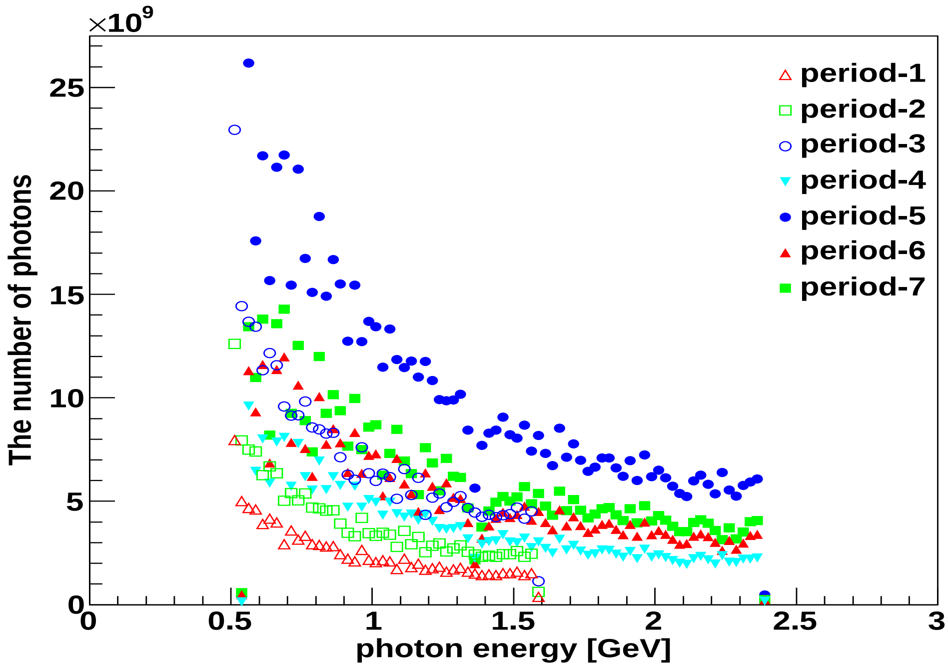

Figure 21: The distribution of the number of incoming photons as a function of photon energy. In this figure, all seven periods are shown and each period has 100 and 25-MeV wide bins in the range from 0.4875 to 2.9875 GeV, respectively. Period 5 has the largest number of photons.

Datasets with different target polarizations should be combined to calculate the asymmetries in the reaction $\gamma p \rightarrow p\pi^{+}\pi^{-}$. Since, however, the number of runs included in each period is different and each run has a different number of events, a normalization factor is needed to adjust the imbalance of the number of events between periods. The events included in the data are roughly proportional to the initial number of photons. The normalization factors can be found from comparing the number of photons between periods. The information about the number of photons in Hall-B is saved in "gflux" files. The gflux files contain the number of photons and their uncertainties in a given bin as shown in Figure 21. The g9a data using the circularly-polarized beam can be divided into two datasets according to the electron beam energy E_{e^-}. One dataset includes Periods 1, 2, and 3 with E_{e^-} = 1.645 GeV and the other dataset contains Periods 4, 5, 6, and 7 with E_{e^-} = 2.427 GeV. In the first dataset, Period 1 and Period 2 have very similar conditions except for the condition of the half-wave plate. Owing to limited statistics, the data of Period 1 and Period 2 will be combined after taking into account the difference of the half-wave plate between the two periods and the combined data will then be defined as Period 2.

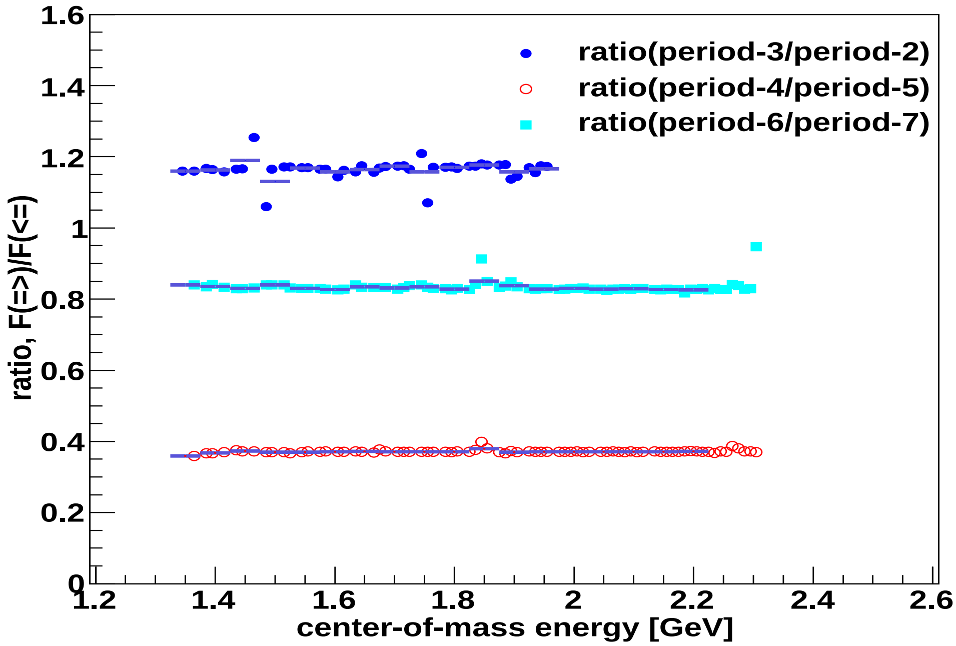

Figure 22: The ratio of the number of photons between periods with the target polarizations parallel (⇒) and anti-parallel (⇐) to the beam.

As mentioned before, the normalization factor is defined as the ratio of the number of photons between datasets with different directions of the target polarization, as shown in Figure 22. The Periods 3, 4, and 6 have the target polarization direction parallel to the beam direction (Table 14) and the other periods have the opposite direction of the target polarization. Therefore, three kinds of period combinations have been used to calculate the polarization observables in this analysis: combination-32 of Periods 3 and 2, combination-45 of Periods 4 and 5, and combination-67 of Periods 6 and 7. The normalization factors used for the different center-of-mass bins in this analysis are listed in Table 15.

The center of mass energy [GeV]	ratio, F($\Rightarrow$)/F($\Leftarrow$)		
	per-3/per-2	per-4/per-5	per-6/per-7
1.35	1.160	0.359	0.840
1.40	1.163	0.368	0.836
1.45	1.190	0.373	0.830
1.50	1.131	0.370	0.840
1.55	1.168	0.370	0.830
1.60	1.157	0.371	0.828
1.65	1.164	0.372	0.834
1.70	1.174	0.371	0.831
1.75	1.158	0.371	0.835
1.80	1.171	0.371	0.828
1.85	1.177	0.380	0.851
1.90	1.157	0.370	0.837
1.95	1.166	0.371	0.828
2.00		0.371	0.830
2.05		0.371	0.828
2.10		0.371	0.829
2.15		0.371	0.827
2.20		0.372	0.826

Table 15: The normalization factors used in combination-32, combination-45, and combination-67.

3.9 Dilution Factor

The g9a experiment utilizes butanol (C_4H_9OH) as the main target material. When this main target is polarized, only the 10 hydrogen nucleons of the butanol can be polarized. For the polarization observables, contributions from polarized free-proton events can be separated from contributions of bound-nucleon events, which are unpolarized and subject to Fermi motion, and other background events by using a dilution factor. This is illustrated in Figure 23. The dilution factor is generally defined as the ratio between the free proton and the full butanol contribution to the cross section. A simple calculation based on the chemical formula of butanol (C_4H_9OH) yields $10/74 = 0.135$ as the ideal dilution factor. In practice, dilution factors are reaction dependent and are generally larger than the ideal factor after the application of the selection cuts.

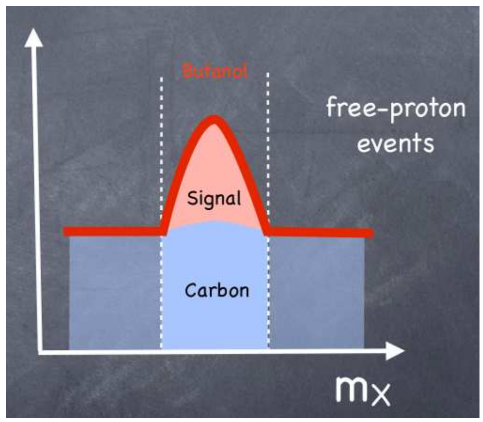

Figure 23: The signal and background events in the butanol data of the g9a experiment.

To determine the dilution factor in this analysis, it was necessary to evaluate the contribution of the bound-nucleon events to the reaction $\gamma p \to p\pi^+\pi^-$. In the g9a experiment, the carbon target is used as a known source of bound nucleons to estimate the contribution of bound-nucleon and background events in the butanol data, as shown in Figure 23. It is assumed that bound-nucleon events from ^{12}C and ^{16}O nuclei in the butanol behave similarly, and can be appropriately subtracted using the data from the carbon target.

Figure 24 (a) illustrates an example of the missing π^- mass distribution using butanol (in black) and carbon (in red) data for the Topology $\gamma p \to p\pi^+(\pi^-)$. Since the carbon data from the g9a experiment suffer from a hydrogen contamination of unknown origin [12], the carbon events from the g9b experiment have been used in this analysis. Figure 24 (b) shows the same butanol distribution where the bound-nucleon and background events are described with a Chebyshev polynomial. To isolate the free-proton events in the butanol data more accurately – the description using Chebyshev polynomials gives only a first estimate of the background shape – the pure carbon distribution from the carbon target must be scaled and then subtracted from the butanol distribution. The equation to calculate the dilution factor is then given by:

$$D(W) = 1 - \frac{\mathbf{s} \cdot N_C(W)}{N_{C_4H_9OH}(W)}, \tag{17}$$

where N_C is the number of events from the carbon target and $N_{C_4H_9OH}$ is the number of events from the butanol target. In Equation 17, $\mathbf{s}$ is the parameter to scale the measured carbon distribution and $\mathbf{s}\cdot N_c$ is the number of events from this scaled carbon distribution, i.e. the assumed true contribution of bound-nucleon and background events in the butanol data. In Section 3.9.1, the method to determine the scale parameters referred to as "phase space scale factors" will be described [13].

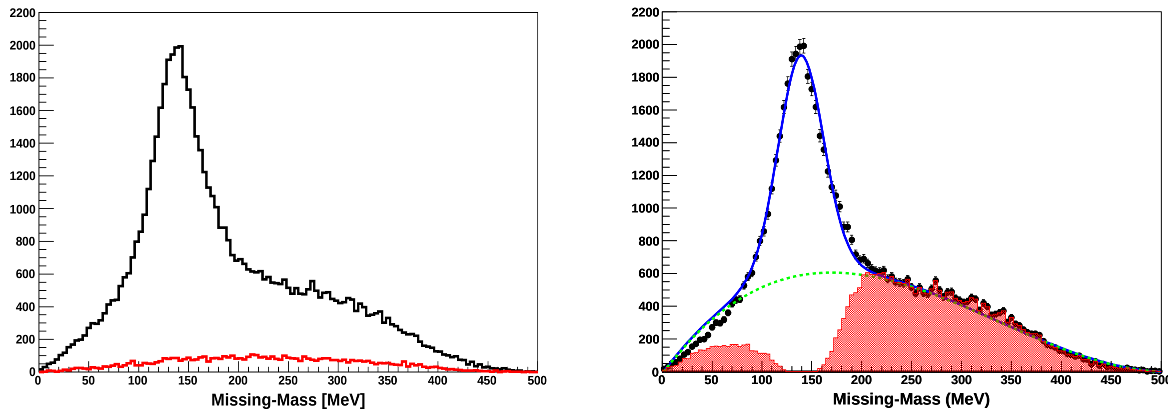

(a) (b)

Figure 24: (a) The missing-mass distributions for the Topology $\gamma p \to p\pi^+(\pi^-)$ from the butanol and carbon target. The black line describes the butanol events from the g9a experiment and the red line denotes the carbon events from the g9b experiment. (b) The fitted missing-mass distributions using a mixed function of a gaussian and a Chebyshev polynomial (blue line). The green dotted line denotes the Chebyshev polynomial in the mixed fitting function. The colored area includes events whose confidence level is less than 0.05. The data are selected from $W \in [1.575, 1.625]$ GeV; the beam polarization is anti-parallel to the beam and the target polarization is anti-parallel to the beam direction.

3.9.1 Phase Space Scale Factors

The scale factors or the "phase space scale factors" are used to produce the scaled carbon distributions from the carbon data. They are determined by comparing the bound-nucleon events from the butanol target with the events from the carbon target. In order to accomplish this, it is necessary to isolate the bound-nucleon events from the butanol data. The free proton events in the butanol data are from protons "at rest", that is, these events are not subject to Fermi motion. Energy conservation for the Topology $\gamma p \to p'\pi^+(\pi^-)$ requires:

$$E_{\pi^-} = \left(E_\gamma + E_p\right) - \left(E_{p'} + E_{\pi^+}\right), \tag{18}$$

where $\left(E_\gamma + E_p\right)$ is the energy of the initial state, and $\left(E_{p'} + E_{\pi^+}\right)$ is the energy of the final state. The free proton events obey the relation $E_p = m_p$ and are distributed near the missing-pion peak, as shown in Figure 25 (a). Since the bound-nucleon events are subject to additional Fermi motion, they obey the relation $E_p = \sqrt{m_p^2 + p_F^2}$, where p_F is the Fermi momentum, and can be distributed far from the missing-pion peak. In the squared missing-mass distribution of the butanol data, free-proton events in the butanol data cannot have negative mass values, but the squared missing-masses of bound-nucleon events can have such negative mass values. In Figure 25, a loose cut at $MM^2 < -0.2$ GeV^2 can isolate bound-nucleon events in the butanol data.

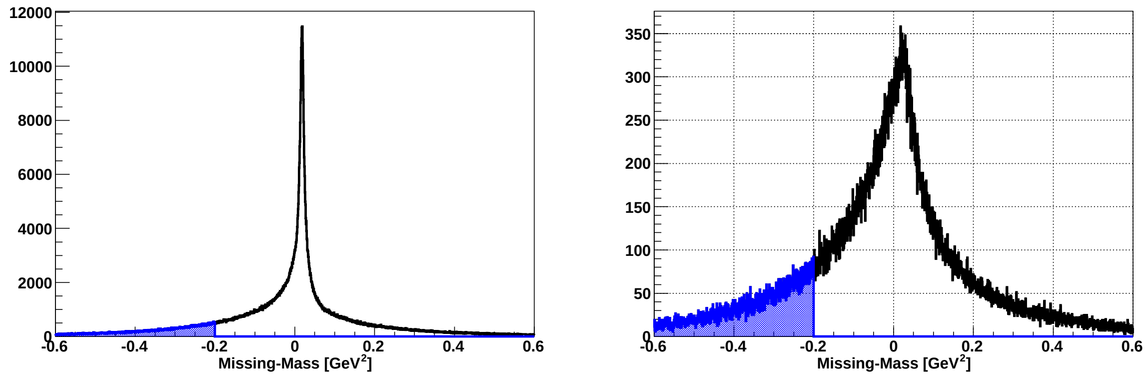

(a) Butanol data (g9a)

(b) Carbon data (g9b)

Figure 25: The missing squared-mass distribution for Topology $\gamma p \to p\pi^+(\pi^-)$ from the butanol target (a) and from the carbon target (b). The blue-shaded regions denote $MM^2 < -0.2$ GeV^2 and should contain only events from bound nucleons.

Figure 26 shows the two dimensional distributions of two kinematic variables: center-of-mass energy, W, versus the azimuthal angle [2], $\phi^*_{\pi^+}$, after applying the loose cut at $MM^2 < -0.2$ GeV^2 in the squared missing-mass.

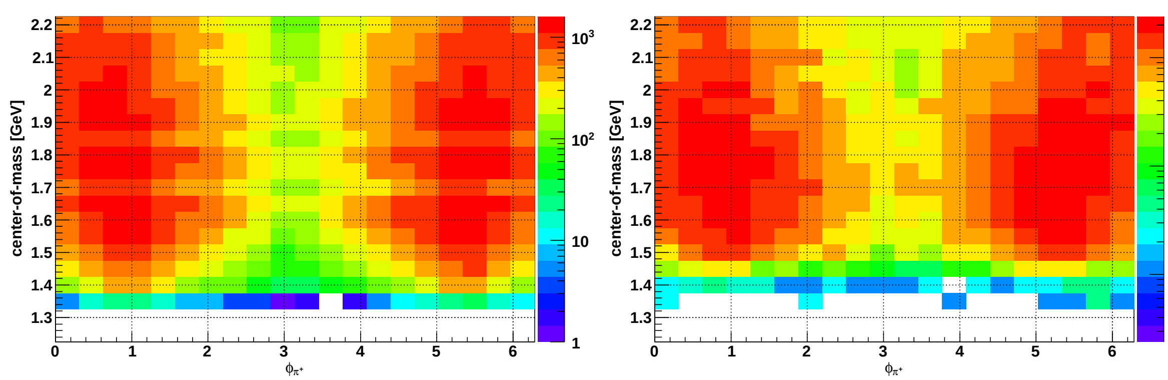

(a) g9a-butanol data

(b) g9b-carbon data

Figure 26: The comparison of the W versus $\phi^*_{\pi^+}$ from (a) the butanol (g9a) and (b) the carbon (g9b) data in the reaction $\gamma p \to p\pi^+(\pi^-)$.

[2] See Section 4.1.1 for an accurate definition of $\phi^*_{\pi^+}$

The phase space scale factors are calculated by simply dividing the two histograms in Figure 26. Figure 27 (a) shows that the resulting phase space scale factors exhibit a very flat distribution and are independent of the azimuthal angle $\phi^*_{\pi^+}$. The enhancement at very low energies is due to statistical limitations. Figure 27 (b) shows the free-proton distribution and scaled carbon distribution calculated by the method described in this section.

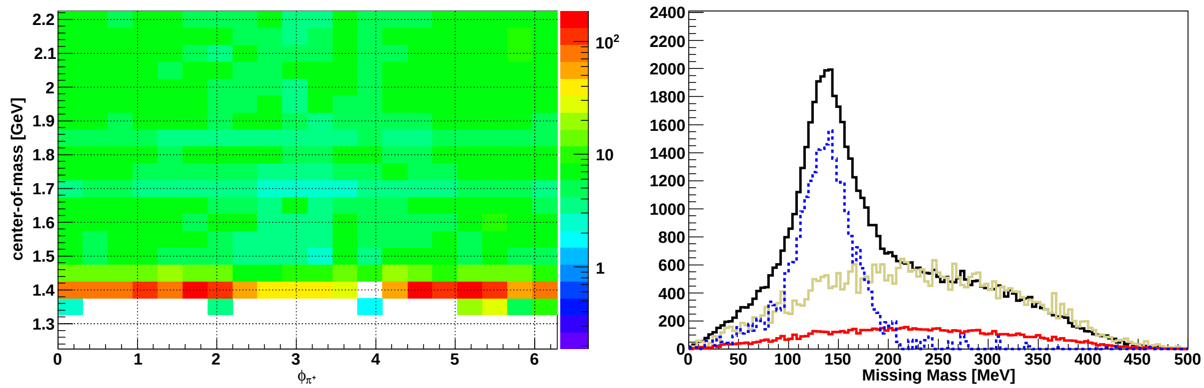

Figure 27: (a) The phase space scale factors in the two-dimensional distribution of W versus $\phi^*_{\pi^+}$. (b) The missing-mass including the free-proton and bound-nucleon distributions calculated using the phase space scale factors given in (a). The black line describes the butanol events for Topology $\gamma p \to p\pi^+(\pi^-)$ and the center-of-mass energy $W \in [1.575,\, 1.625]$ GeV from the g9a experiment, and the red line denotes the carbon events from the g9b experiment. The dark-yellow line is the scaled carbon distribution, and the blue dashed line is the free-proton distribution made from the phase space scale factors.

3.9.2 Q-Factor Method

Another approach, called the Q-factor method, has been used to separate the signal events from the background events. The Q-factor method assigns each event in the butanol data an event-based quality factor which denotes the probability that an event is a signal event [14]. The contribution of the bound-nucleon and background events can then be removed from the butanol data by weighting each event with this Q-factor. Such event-based dilution factors serve two important purposes. On the one hand, the database of four-vectors for the two-pion channel can easily be analyzed in an event-based partial-wave analysis. On the other hand, since the photoproduction of two pseudoscalar mesons requires five independent kinematic variables, the Q-factors will allow us to quickly re-display the asymmetries for a different choice of kinematic variables without repeating the analysis and finding new dilution factors each time.

To determine the Q-factors, the following five kinematic variables have been chosen which define the five-dimensional kinematic phase space of the reaction $\gamma p \to p\pi^+\pi^-$: $\cos\Theta^{\text{proton}}_{\text{c.m.}}$, a mass ($m_{p\pi^+}$, $m_{p\pi^-}$, or $m_{\pi^+\pi^-}$), the center-of-mass energy, W, and the polar and azimuthal angle $\theta^*_{\pi^+}$ and $\phi^*_{\pi^+}$ in the rest frame of the $\pi^+\pi^-$ system. [3] For each event (seed event), events closest in the kinematic

[3]See Section 4.1.1 for a proper definition of the $\gamma p \to p\pi^+\pi^-$ kinematics.

phase space defined by 4 of the 5 independent variables have been selected to perform event-based unbinned maximum likelihood fits [15] in the remaining fifth variable. In this analysis, we have performed fits on the missing pion mass in Topology 1 or 2. To locate the nearest neighbor events, the following equation describing the distance between event a and b, $D_{a,b}$, has been used:

$$D_{a,b}^2 = \sum_{i=1}^{4} \left(\frac{\Gamma_i^a - \Gamma_i^b}{\Delta_i} \right)^2 , \tag{19}$$

where Γ is a kinematic variable and Δ_i is the maximum range of the kinematic variable Γ. Table 16 shows the specific kinematic variables and their maximum ranges used in the Q-factor method.

Table 16: The kinematic variables Γ_i and their ranges Δ_i used in the Q-factor method.

Γ_i	Kinematic variable	Their maximum ranges, Δ_i
Γ_0	center-of-mass energy, W	50 [MeV]
Γ_1	$\cos\Theta_{\text{c.m.}}^{\text{proton}}$	2
Γ_2	$\phi_{\pi^+}^*$	2π [radian]
Γ_3	$\cos\theta_{\pi^+}^*$	2

The distances of all other events from a seed event are computed using Equation 19, and then the 300 nearest neighbors are selected to form a missing-mass distribution for the maximum-likelihood fitting. The missing-mass distributions made from the carbon data are used for the background function. The total fit function utilizes a signal function for the missing-pion peak and the carbon distribution from the g9b experiment for the description of the background. For the latter, a seed event in the carbon sample was chosen which is kinematically closest to the butanol seed event and the 300 nearest neighbors for the carbon seed events have been selected. Figure 28 (a) shows an example of the missing-mass distribution for a particular pair of a butanol and carbon seed event. These distributions will be used as the input for the Q-factor method.

In the missing π^- mass distribution from the butanol target for Topology $\gamma p \to p\pi^+(\pi^-)$, a clear peak near 139.5 MeV for the π^- can be seen. Since the peak is much broader than the natural width of the π^-, a gaussian resolution function should be used to describe the shape of the peak. Unfortunately, a gaussian could not describe very well the high-mass tail of the signal; for this reason, a Voigt function with a very small Breit-Wigner component has been used for the signal. The true carbon distribution of the g9b experiment is used for the background shape which describes a smooth non-peaking distribution underneath the peak. For this analysis, the total function is then defined as:

$$f(x) = N \cdot [f_s \cdot S(x) - (1 - f_s) \cdot B(x)] . \tag{20}$$

where $S(x)$ denotes the signal and $B(x)$ the background function. N is a normalization constant and f_s is the signal fraction with a value between 0 and 1. The Roofit package of the CERN ROOT software [15] is used for the fit procedure. The Q-factor itself is then given by:

$$Q = \frac{s(x)}{s(x) + b(x)} , \tag{21}$$

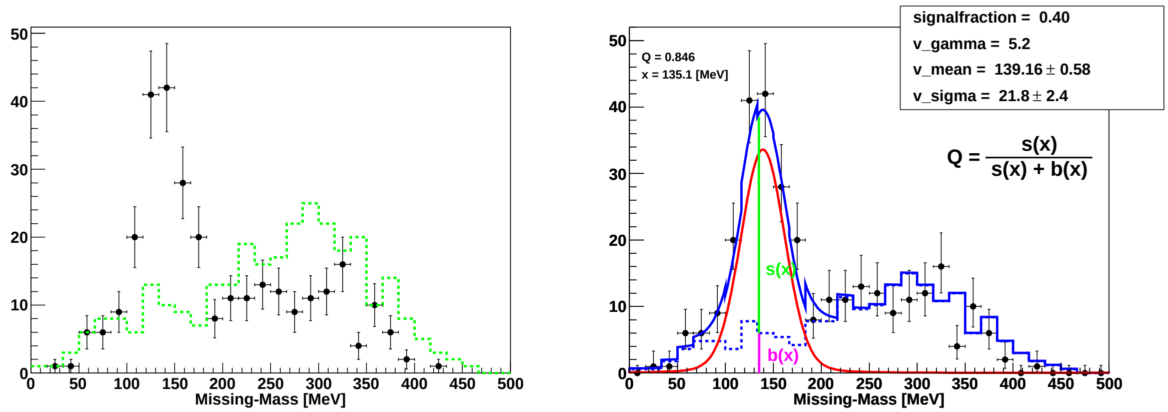

Figure 28: (a) An example of a missing-mass distribution made from the 300 nearest events selected from butanol (black dots) and carbon (green line) data in Topology $\gamma p \to p\pi^+(\pi^-)$, $W \in [1.575,\, 1.625]$ GeV, and Period 7. (b) Fitted missing-mass distribution (black dots) using a combination of the signal (red line) and carbon background (blue dashed line) functions.

where x is the missing mass of the seed event and $s(x) = f_s \cdot S(x)$ and $b(x) = (1 - f_s) \cdot B(s)$. The total fitting function $f(x)$ in Equation 20 has four parameters: Γ, mean, and σ of the Voigt function and f_s (the signal fraction). The mean of the Voigt function has been be fixed to 139.5 MeV; the σ of the Voigt function has no limitation. The Γ parameter of the Voigt function has been fixed to a very small value, which was derived from a similar fit to the fully integrated distribution (summed over all events, as shown in Figure 29).

The signal fraction f_s is the most important parameter and is related to the event-based scale factor.

The event-based scale factor, **s**, is given by (similar to Equation 20):

$$\mathbf{s} = \frac{(1 - f_s) \cdot (\#\text{ of nearest butanol events})}{(\#\text{ of nearest carbon events})} = 1 - f_s\,, \tag{22}$$

where the number of nearest butanol events is equal to the number of nearest carbon events. The event-based scale factors are assumed to be the same for all butanol seed events in a particular W bin. The peak of the reduced-χ^2 distribution derived from the all Q-factor fits has a value near one, as shown in the example in Figure 30 (a), and this guarantees good quality fitting. Similar phase space scale factor, as discussed in Section 3.9.1, can be derived from the Q-factor method. Figure 30 (b) shows the ratio of the phase space scale factors derived from kinematics (Section 3.9.1) to the phase space scale factors derived from the Q-factor method. Figure 30 (b) shows a fairly flat distribution, close to one. Figure 31 shows the free-proton distribution and scaled carbon distribution calculated by the Q-factor method for $W \in [1.575,\, 1.625]$ GeV. The results of the Q-factor method applied in the whole energy range $W \in [1.375,\, 2.125]$ GeV are shown in Figures 32-35. We have applied the Q-factor method to the missing-π^- peak in Topology 1 and to the missing-π^+ peak in Topology 2. For Topology 4 with all final-state particles detected, we decided to artificially remove the π^- and then to fit the corresponding missing-π^- peak.

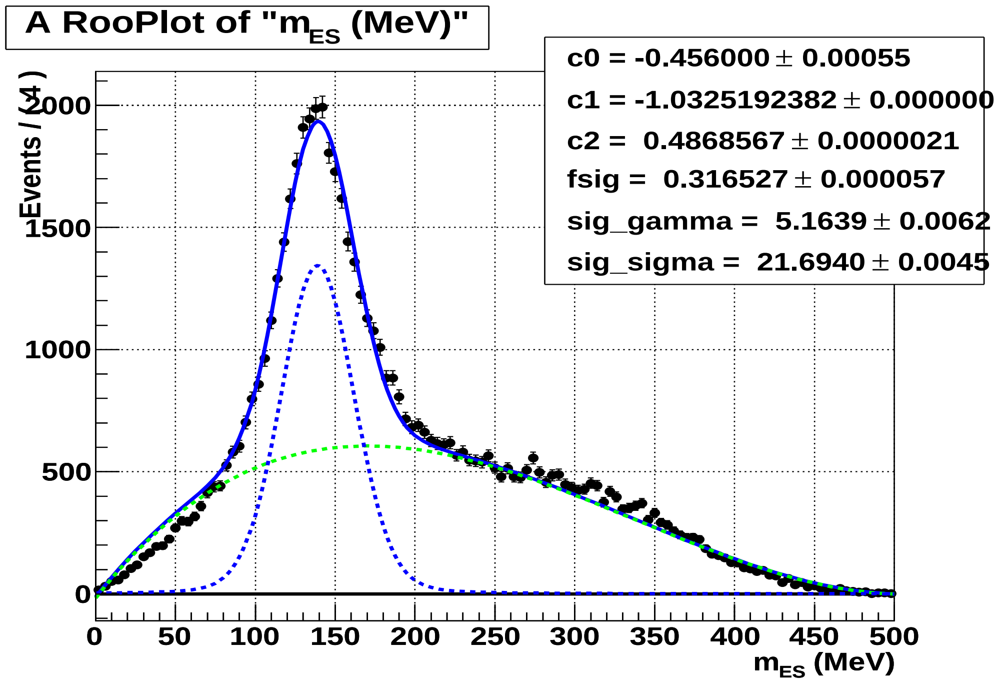

Figure 29: The fitted integrated missing-mass distribution from the butanol data in Topology 1, $\gamma p \to p\pi^+(\pi^-)$, $W \in [1.575, 1.625]$ GeV, and Period 7 using a Voigt function. The Γ parameter from this fit was used as a fixed value in the Q-factor method.

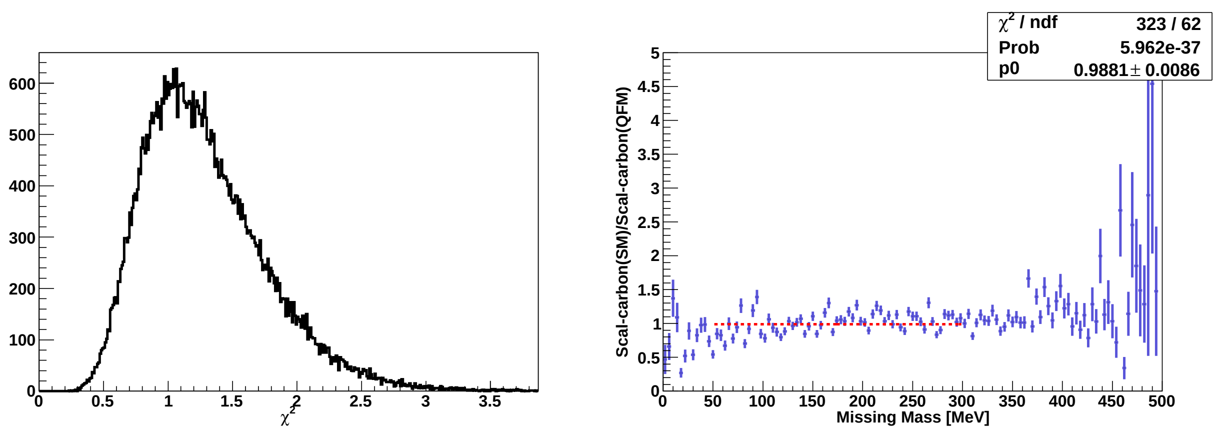

(a)

(b)

Figure 30: (a) An example of the normalized χ^2 distribution from the Q-factor method applied to Topology $\gamma p \to p\pi^+(\pi^-)$ and $W \in [1.575, 1.625]$ GeV. (b) The ratio of the scaled carbon distributions using the phase space scale factors (Section 3.9.1) and the Q-factor method.

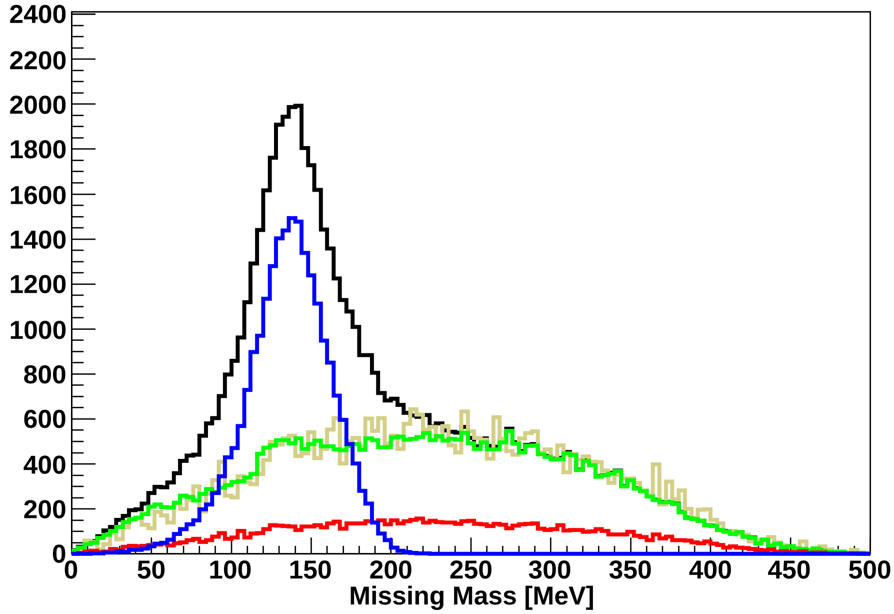

Figure 31: The missing-mass distribution with the free-proton and bound-nucleon distribution calculated by the Q-factor method. The black and red line denote the butanol (g9a) and carbon (g9b) data for Topology $\gamma p \to p\pi^+(\pi^-)$ and $W \in [1.575, 1.625]$ GeV, also used in Figure 27, respectively. The dark-yellow line and the green line denote the scaled carbon distributions using the method described in Section 3.9.1 and the Q-factor method, respectively.

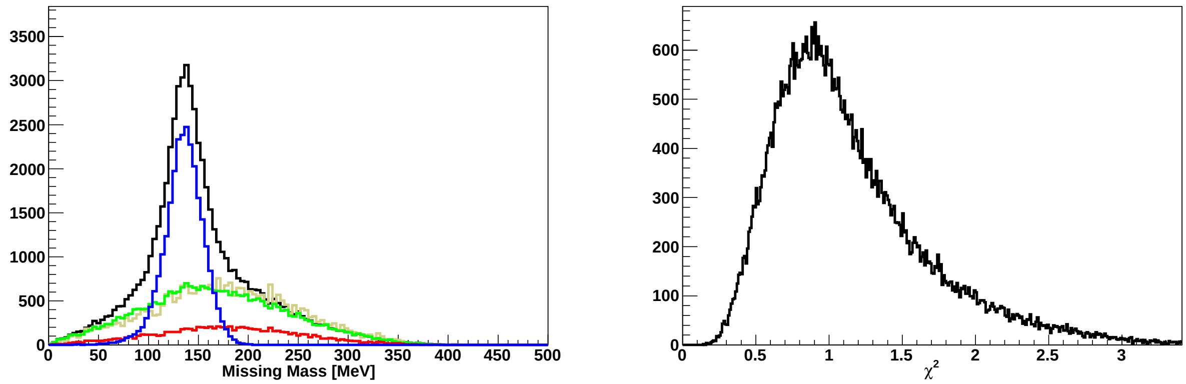

(a) $W = 1.50$ GeV

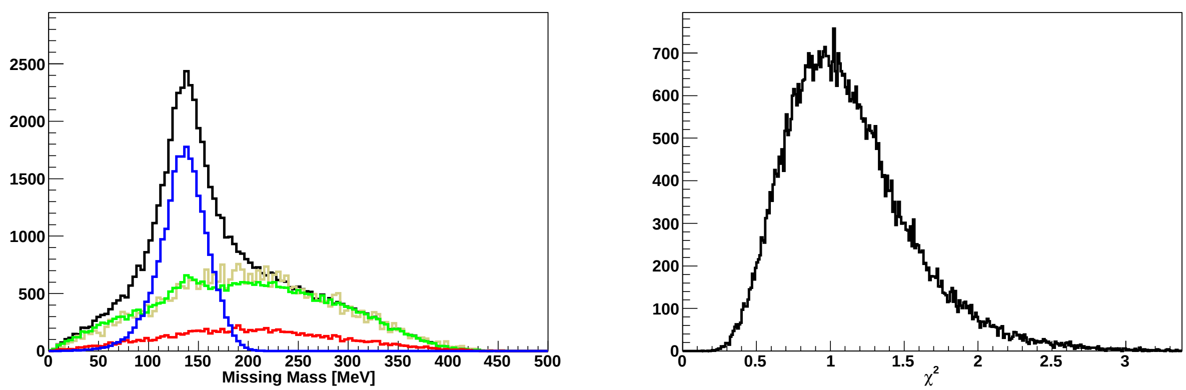

(b) $W = 1.55$ GeV

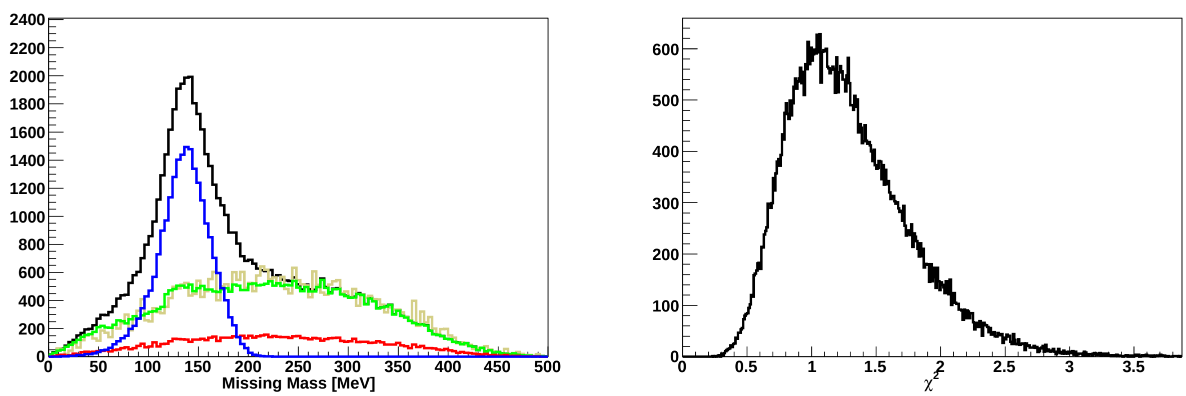

(c) $W = 1.60$ GeV (same as Figure 31)

Figure 32: Missing-mass distributions with the free-proton and bound-nucleon distributions calculated using the method described in Section 3.9.1 (dark yellow) and the Q-factor method (green) for Topology $\gamma p \to p\pi^+(\pi^-)$, center-of-mass energy range $W \in [1.475, 1.625]$ GeV, and Period 7, and their corresponding reduced-χ^2 distributions.

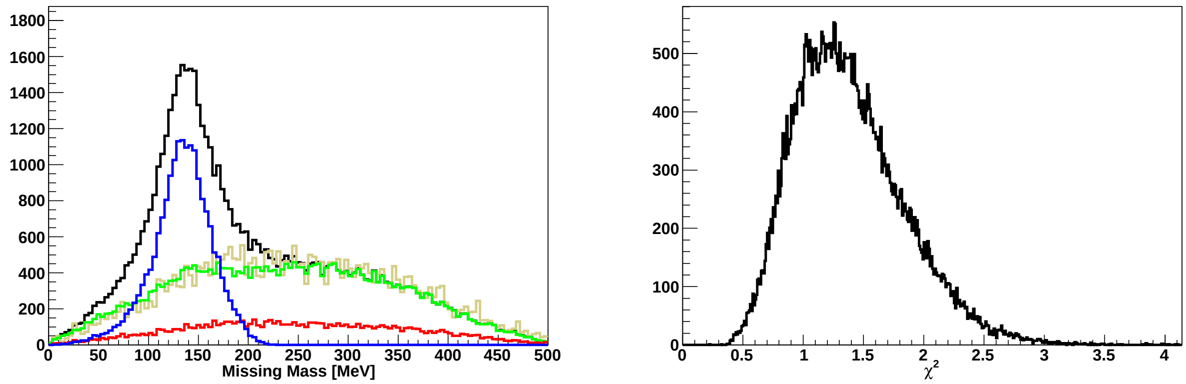

(a) $W = 1.65$ GeV

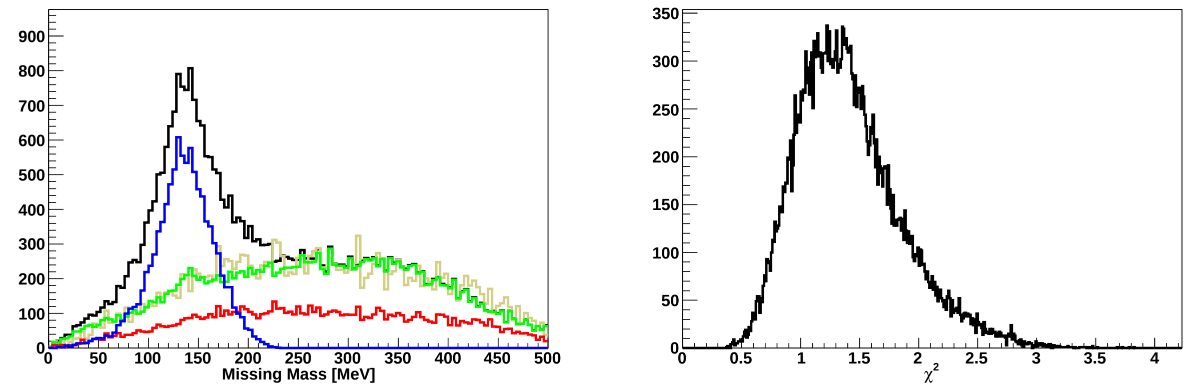

(b) $W = 1.70$ GeV

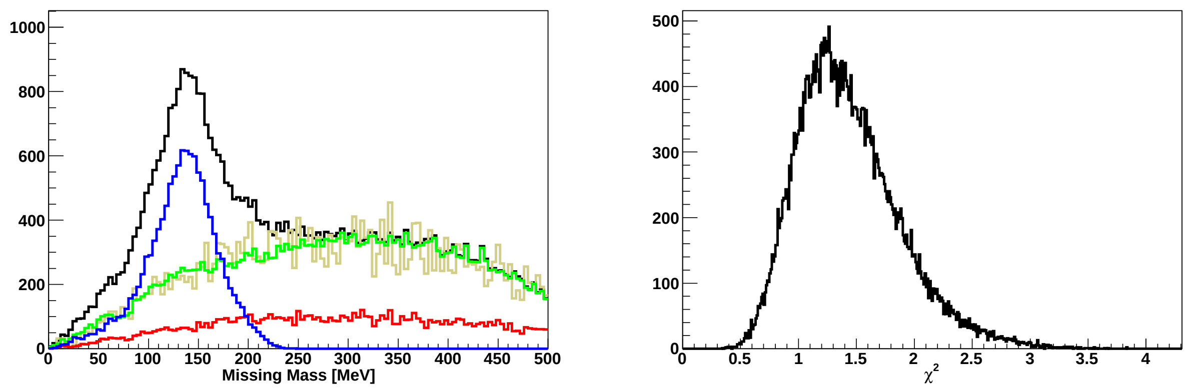

(c) $W = 1.75$ GeV

Figure 33: Missing-mass distributions with the free-proton and bound-nucleon distributions calculated using the method described in Section 3.9.1 (dark yellow) and the Q-factor method (green) for Topology $\gamma p \to p\pi^+(\pi^-)$, center-of-mass energy range $W \in [1.625, 1.775]$ GeV, and Period 7, and their corresponding reduced-χ^2 distributions.

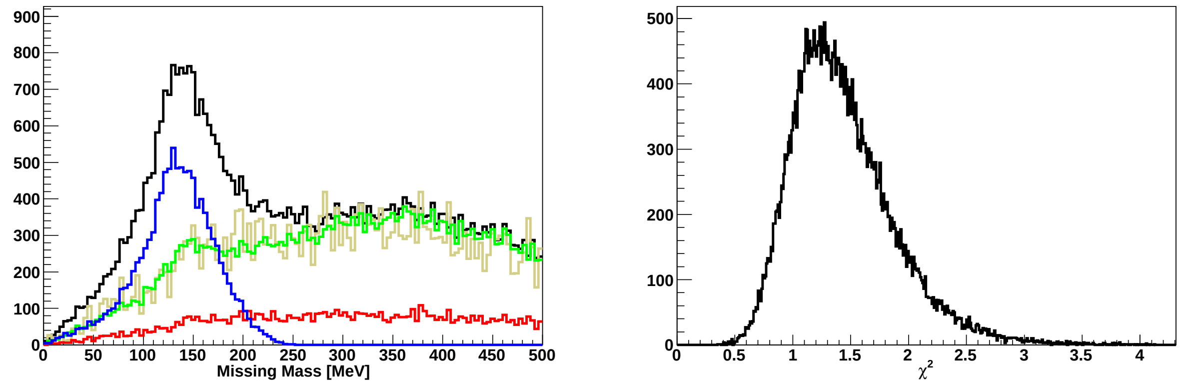

(a) $W = 1.80$ GeV

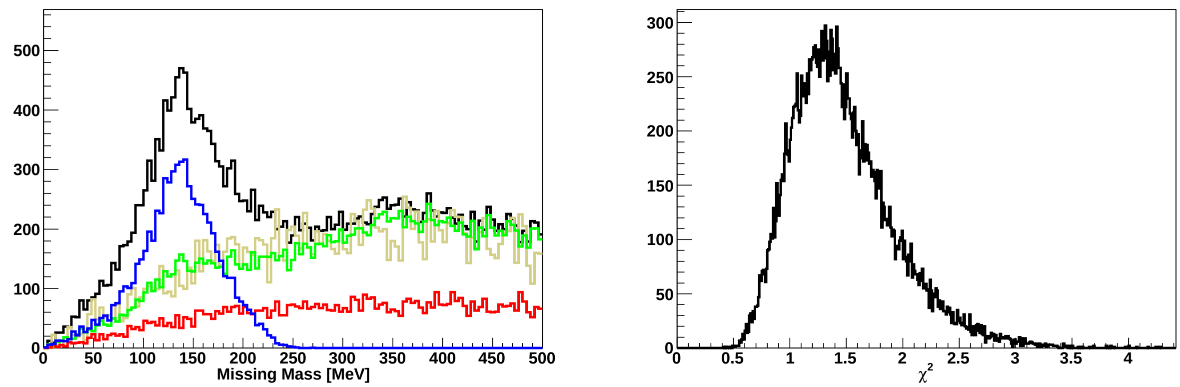

(b) $W = 1.85$ GeV

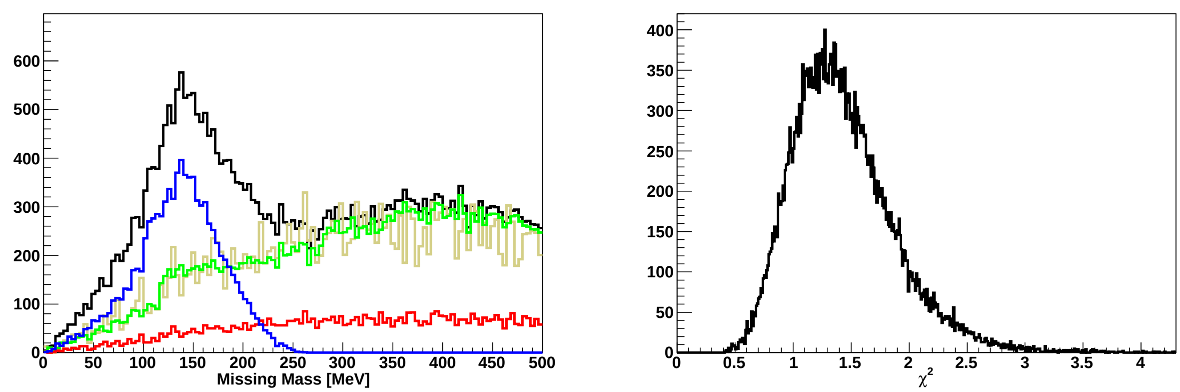

(c) $W = 1.90$ GeV

Figure 34: Missing-mass distributions with the free-proton and bound-nucleon distributions calculated using the method described in Section 3.9.1 (dark yellow) and the Q-factor method (green) for Topology $\gamma p \to p\pi^+(\pi^-)$, center-of-mass energy range $W \in [1.775, 1.925]$ GeV, and Period 7, and their corresponding reduced-χ^2 distributions.

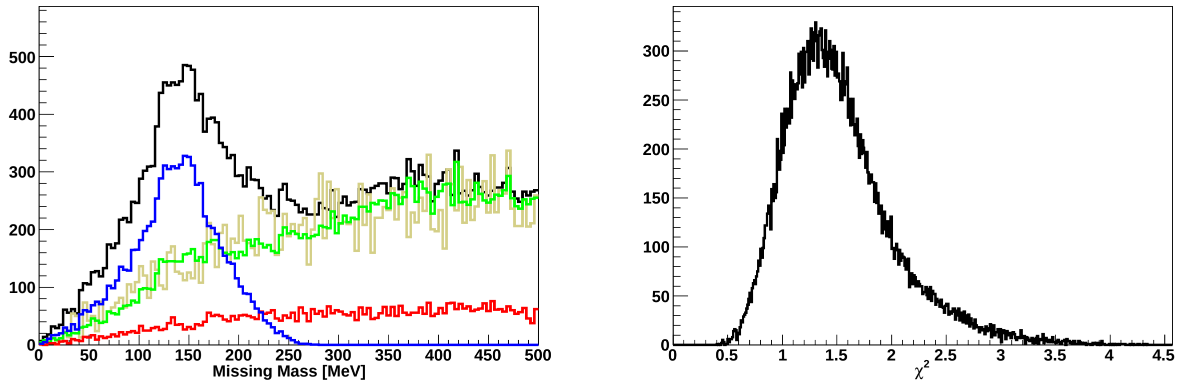

(a) $W = 1.95$ GeV

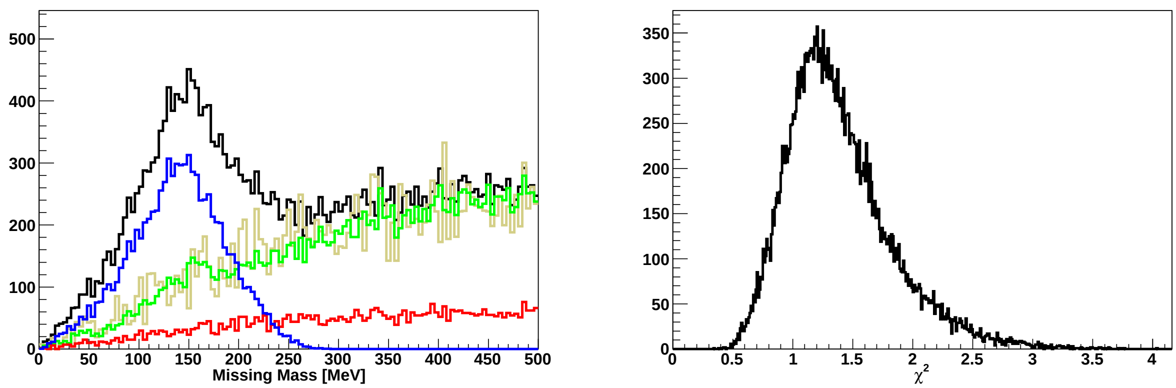

(b) $W = 2.00$ GeV

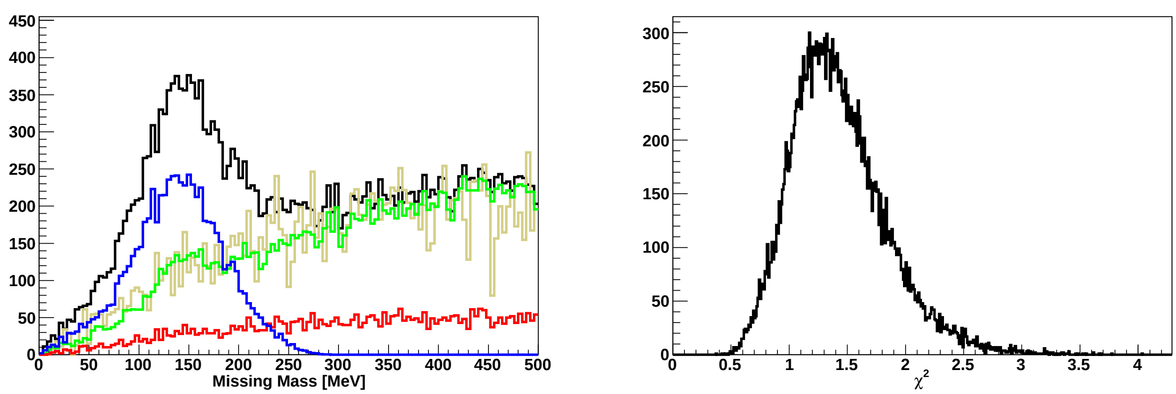

(c) $W = 2.05$ GeV

Figure 35: Missing-mass distributions with the free-proton and bound-nucleon distributions calculated using the method described in Section 3.9.1 (dark yellow) and the Q-factor method (green) for Topology $\gamma p \to p\pi^+(\pi^-)$, center-of-mass energy range $W \in [1.925, 2.075]$ GeV, and Period 7, and their corresponding reduced-χ^2 distributions.

4 Data Analysis and Extraction of Polarization Observables

After all corrections, cuts and kinematic fitting were applied, the different possible final-state topologies for the reaction $\gamma p \to p\pi^+\pi^-$ have been selected and the extraction of polarization observable commenced. The polarization observables $\mathbf{I}^{\odot}$, $\mathbf{P_z}$, and $\mathbf{P_z^{\odot}}$ have been extracted from the double-pion photoproduction data utilizing circular beam and longitudinal target polarization. This chapter presents the methodology utilized in the extraction of these polarization observables from the experimental data.

4.1 General Data Analysis

4.1.1 Binning and Angles

In order for an analysis to be conducted, the kinematics of the reaction of interest must be understood. First, the kinematics of $\gamma p \to p\pi^+\pi^-$ requires a selection of five independent kinematic variables. The kinematic variables chosen for this analysis are $\cos\Theta_{\text{c.m.}}$, a mass ($m_{p\pi^+}$, $m_{p\pi^-}$, or $m_{\pi^+\pi^-}$), the center-of-mass energy, W, as well as $\theta^*_{\pi^+}$ and $\phi^*_{\pi^+}$, where the latter two angles denote the polar and azimuthal angles of the π^+ in the rest frame of the $\pi^+\pi^-$ system. A diagram showing the kinematics of the reaction $\gamma p \to p\pi^+\pi^-$ can be seen in Figure 36. The blue plane represents the center-of-mass production plane composed of the initial photon and recoiling proton, whereas the red plane represents the decay plane formed by two of the final-state particles.

The angle $\phi^*_{\pi^+}$ is a kinematic variable unique to a final state containing two pseudoscalar mesons. It describes the orientation of the decay plane containing the two pions (or another pair of the particles) with respect to the production plane, which is defined by the incident photon and recoiling proton. It is also given by the azimuthal angle of the π^+ meson in the rest frame of the $\pi^+\pi^-$ system. This azimuthal angle, $\phi^*_{\pi^+}$, is calculated via two boosts, the first being a boost along the beam line into the overall center-of-mass frame. The second boost occurs along the axis that is antiparallel to the recoiling proton and results in the rest frame wherein the two final-state pions occur back-to-back. Mathematically, the angle $\phi^*_{\pi^+}$ is uniquely determined by the following expression:

$$\cos\phi^* \;=\; \frac{(\vec{p}\times\vec{a})\,\cdot\,(\vec{b}_2\times\vec{b}_1)}{|\vec{p}\times\vec{a}|\;|\vec{b}_2\times\vec{b}_1|}\,, \tag{23}$$

where $\vec{p}$ is the initial-state proton and $\vec{a}$, $\vec{b}_1$, and $\vec{b}_2$ are the final-state particles.

In this analysis the data are then binned in two of the five independent kinematical variables. These binning variables are the center-of-mass energy, W, and the azimuthal angle, $\phi^*_{\pi^+}$. In order to compare the polarization observable $\mathbf{I}^{\odot}$ with the results from the CLAS g1c analysis [17], the center-of-mass energy W is divided into 50-MeV wide bins. This results in a total of 20 bins in the center-of-mass energy, covering an energy range from 1.225 GeV to 2.225 GeV. For the azimuthal angle, $\phi^*_{\pi^+}$, 20 bins are used, covering a range from $0 \le \phi^*_{\pi^+} \le 2\pi$, to describe the structure of the observable more clearly than in the CLAS g1c analysis, which used 11 bins in the same angular range. This choice of binning using two variables results in a total of 400 bin combinations per final-state topology.

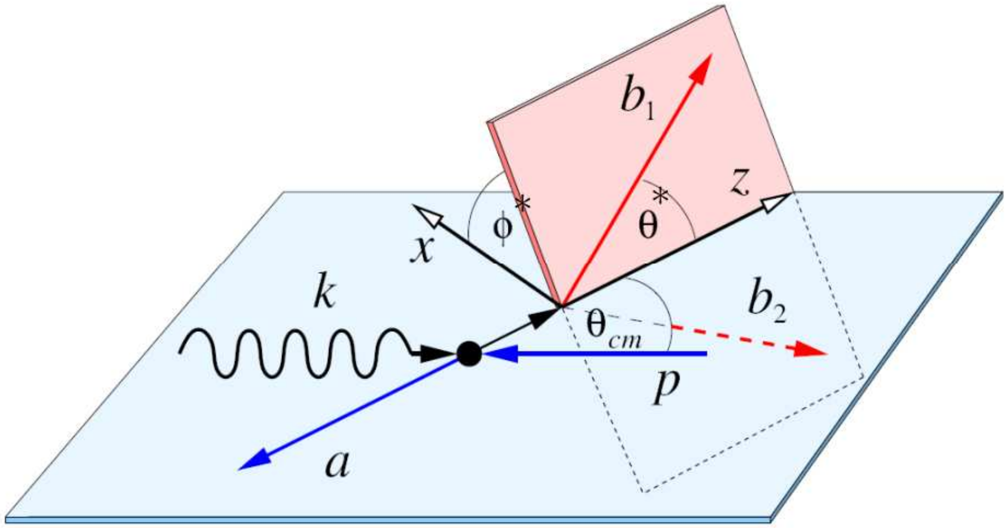

Figure 36: A diagram describing the kinematics of the reaction $\gamma p \to p\pi^+\pi^-$. The blue plane represents the center-of-mass production plane composed of the initial photon and proton, whereas the red plane represents the decay plane formed by two of the final-state particles. In the diagram, k is the initial photon and the particle p denotes the polarized target proton. a, b_1, and b_2 are the three particles of the final state. If we assume that particle a is the recoiling proton, b_1 and b_2 are the two pions, π^+ and π^-. $\Theta_{c.m.}$ denotes the angle between the initial proton and the particle a in the center-of-mass system. ϕ^* and θ^* indicate the azimuthal and polar angles of the particle b_1 in the rest frame of b_1 and b_2.

4.1.2 Observables with Circular Beam and Longitudinal Target Polarization

For $\gamma p \to p\,\pi\pi$, without measuring the polarization of the recoiling nucleon, the differential cross section, $d\sigma/dx_i$, is given by [16]:

$$\begin{aligned}\frac{\mathrm{d}\,\sigma}{\mathrm{d}\,x_i} = \sigma_0 \{ & (1 + \vec{\Lambda}_i \cdot \vec{\mathbf{P}}) \\ & + \delta_{\odot} (\mathbf{I}^{\odot} + \vec{\Lambda}_i \cdot \vec{\mathbf{P}}^{\odot}) \\ & + \delta_l [\sin 2\beta (\mathbf{I}^{\mathbf{s}} + \vec{\Lambda}_i \cdot \vec{\mathbf{P}}^{\mathbf{s}}) \\ & \quad + \cos 2\beta (\mathbf{I}^{\mathbf{c}} + \vec{\Lambda}_i \cdot \vec{\mathbf{P}}^{\mathbf{c}})] \} \,,\end{aligned} \tag{24}$$

where x_i are kinematic variables and σ_0 is the unpolarized cross section. $\vec{\Lambda}_i$ denotes the polarization of the initial nucleon and $\delta_{\odot}$ is the degree of circular polarization of the photon beam, while δ_l is the degree of linear polarization. The two-meson final state equation, as referenced in Equation 24, contains 15 polarization observables. $\mathbf{I}^{\odot}$, $\mathbf{I}^{\mathbf{s}}$, and $\mathbf{I}^{\mathbf{c}}$ are observables which arise from the beam polarization. The observable $\mathbf{I}^{\odot}$ describes the beam asymmetry for an unpolarized target and a circularly-polarized photon beam. The observables $\vec{\mathbf{P}}$ represent the target asymmetry that arise if only the target nucleon is polarized, and $\vec{\mathbf{P}}^{\odot}$ as well as $\vec{\mathbf{P}}^{\,\mathrm{s,c}}$ represent the double-polarization observables if, in addition to the target nucleon, the incoming photon is also polarized, either circularly or linearly, respectively. The observable $\mathbf{I}^{\odot}$, in the photoproduction of two charged pions, has been published previously by the CLAS collaboration. It has been analyzed from CLAS g1c data [17] and, for other isospin-related channels, from data obtained by the MAMI, TAPS, and A2 collaborations [18]. The observable $\mathbf{P}_z^{\odot}$ has been published at low energies (below g9a energies) in photoproduction using GDH and A2 collaboration data [19].

The reaction rate for $\gamma p \to p\,\pi\pi$, in the case of a circularly-polarized beam on a longitudinally-polarized target, can be written as:

$$\frac{\mathrm{d}\,\sigma}{\mathrm{d}\,x_i} = \sigma_0 \left\{ \left(1 + \Lambda_z \cdot \mathbf{P_z} \right) + \delta_{\odot} \left(\mathbf{I}^{\odot} + \Lambda_z \cdot \mathbf{P_z^{\odot}} \right) \right\}, \tag{25}$$

and results in the polarization observables $\mathbf{I}^{\odot}$, the beam-helicity asymmetry, the observable $\mathbf{P_z}$, the target asymmetry, and the observable $\mathbf{P_z^{\odot}}$, the helicity difference, which can be determined from the dataset in this analysis.

4.2 Polarization Observable $\mathbf{I}^{\odot}$

4.2.1 Beam Helicity Asymmetry

The differential cross section for $\gamma p \to p\,\pi\pi$ (Equation 25) is experimentally given by :

$$\frac{\mathrm{d}\,\sigma}{\mathrm{d}\,x_i} = \frac{N_{\mathrm{data}}}{A \cdot F \cdot \rho \cdot \Delta x_i}, \tag{26}$$

where N_{data} is the number of data events measured in the g9a experiment, A is the acceptance, F is the photon flux, ρ is the target area density parameter, and Δx_i is the width of the kinematic bin. Therefore, the number of measured data events, N_{data}, can be also defined as (using polarized data and combining Equations 25 and 26):

$$N_{\mathrm{data}} = \sigma_0 \cdot (A \cdot F \cdot \rho \cdot \Delta x_i) \left\{ \left(1 + \bar{\Lambda}_z \cdot \mathbf{P_z} \right) + \bar{\delta}_{\odot} \left(\mathbf{I}^{\odot} + \bar{\Lambda}_z \cdot \mathbf{P_z^{\odot}} \right) \right\}. \tag{27}$$

Since the beam and target polarization of N_{data} in the g9a dataset have a certain direction, a definition of this direction is required. In the following, $\rightarrow$ and $\leftarrow$ indicate that the circular beam polarization is parallel or antiparallel to the beam axis; $\Rightarrow$ and $\Leftarrow$ indicate that the longitudinal target polarization is parallel or antiparallel to the beam axis. In this analysis, we have used four different datasets with the following beam and target polarizations:

$$N(\rightarrow\Rightarrow), N(\leftarrow\Rightarrow), N(\rightarrow\Leftarrow), \text{ and } N(\leftarrow\Leftarrow). \tag{28}$$

In the process of calculating the asymmetries, the product $\sigma_0 \cdot A \cdot \rho \cdot \Delta x_i$ will cancel out. Moreover, each term in Equation 28 has a different photon flux F, average beam polarization $\bar{\delta}_{\odot}$, and average target polarization $\bar{\Lambda}_z$:

$$N_{\mathrm{combination}} \sim F \left\{ \left(1 + \bar{\Lambda}_z \cdot \mathbf{P_z} \right) + \bar{\delta}_{\odot} \left(\mathbf{I}^{\odot} + \bar{\Lambda}_z \cdot \mathbf{P_z^{\odot}} \right) \right\}. \tag{29}$$

The distributions of events with these four different polarization settings, as a function of ϕ^*, have the form:

$$\begin{aligned}
N(\phi^*,\sigma(\rightarrow\Rightarrow)) &\sim F(\rightarrow\Rightarrow)\Big\{1+\bar{\Lambda}_z(\Rightarrow)\mathbf{P_z}+\bar{\delta}_\odot(\rightarrow)\Big(\mathbf{I}^\odot+\bar{\Lambda}_z(\Rightarrow)\mathbf{P_z^\odot}\Big)\Big\}\\
N(\phi^*,\sigma(\leftarrow\Rightarrow)) &\sim F(\leftarrow\Rightarrow)\Big\{1+\bar{\Lambda}_z(\Rightarrow)\mathbf{P_z}-\bar{\delta}_\odot(\leftarrow)\Big(\mathbf{I}^\odot+\bar{\Lambda}_z(\Rightarrow)\mathbf{P_z^\odot}\Big)\Big\}\\
N(\phi^*,\sigma(\rightarrow\Leftarrow)) &\sim F(\rightarrow\Leftarrow)\Big\{1-\bar{\Lambda}_z(\Leftarrow)\mathbf{P_z}+\bar{\delta}_\odot(\rightarrow)\Big(\mathbf{I}^\odot-\bar{\Lambda}_z(\Leftarrow)\mathbf{P_z^\odot}\Big)\Big\}\\
N(\phi^*,\sigma(\leftarrow\Leftarrow)) &\sim F(\leftarrow\Leftarrow)\Big\{1-\bar{\Lambda}_z(\Leftarrow)\mathbf{P_z}-\bar{\delta}_\odot(\leftarrow)\Big(\mathbf{I}^\odot-\bar{\Lambda}_z(\Leftarrow)\mathbf{P_z^\odot}\Big)\Big\}.
\end{aligned} \tag{30}$$

In the ideal case, the photon flux will be well known, and flux parameters from the four different data combinations will have the same value: $F(\rightarrow\Rightarrow)) = F(\leftarrow\Rightarrow) = F(\rightarrow\Leftarrow) = F(\leftarrow\Leftarrow) = F$. Similarly, the ideal experimental setup makes it possible to use $\bar{\Lambda}_z(\Rightarrow) = \bar{\Lambda}_z(\Leftarrow) = \bar{\Lambda}_z$ and $\bar{\delta}_\odot(\rightarrow)$ $= \bar{\delta}_\odot(\leftarrow) = \bar{\delta}_\odot$, and the datasets can be reliably scaled. Since the polarization observable $\mathbf{I}^\odot$ refers to unpolarized target data, a dataset with unpolarized target nucleons and a circularly-polarized beam is needed. We can produce unpolarized target data by adding the data with different target polarizations:

$$\begin{aligned}
N(\phi^*,\sigma(\rightarrow)) &\sim N(\phi^*,\sigma(\rightarrow\Rightarrow))+N(\phi^*,\sigma(\rightarrow\Leftarrow)) \sim F\Big(2+2\cdot\bar{\delta}_\odot\mathbf{I}^\odot\Big)\\
N(\phi^*,\sigma(\leftarrow)) &\sim N(\phi^*,\sigma(\leftarrow\Rightarrow))+N(\phi^*,\sigma(\leftarrow\Leftarrow)) \sim F\Big(2-2\cdot\bar{\delta}_\odot\mathbf{I}^\odot\Big),
\end{aligned} \tag{31}$$

and the beam asymmetry derived from the unpolarized target data can be expressed as:

$$\frac{N(\phi^*,\sigma(\rightarrow))-N(\phi^*,\sigma(\leftarrow))}{N(\phi^*,\sigma(\rightarrow))+N(\phi^*,\sigma(\leftarrow))} = \bar{\delta}_\odot\mathbf{I}^\odot\,. \tag{32}$$

However, in the more general situation [20], $\bar{\Lambda}_z(\Rightarrow) \neq \bar{\Lambda}_z(\Leftarrow)$. As the polarization of the JLab electron beam in each period is flipped 30 times per second, we can assume that the flux parameters between the different beam polarizations are the same, $F(\rightarrow) = F(\leftarrow)$, and the beam polarization between the different beam directions is also the same, $\bar{\delta}_\odot(\rightarrow) = \bar{\delta}_\odot(\leftarrow) = \bar{\delta}_\odot$. Unfortunately, the flux parameters between the different target polarizations are different, and we have $F(\Rightarrow) \neq F(\Leftarrow)$. In this analysis, the four different datasets (Equation 28) were scaled with the proper target polarization and photon flux, as shown in Figure 37:

$$\begin{aligned}
\frac{N(\phi^*,\sigma(\rightarrow\Rightarrow))}{\Lambda_z(\Rightarrow)F(\Rightarrow)} &\sim \Big\{\Big(\frac{1}{\Lambda_z(\Rightarrow)}+\mathbf{P_z}\Big)+\frac{\bar{\delta}_\odot}{\Lambda_z(\Rightarrow)}\mathbf{I}^\odot+\bar{\delta}_\odot\mathbf{P_z^\odot}\Big\}\\
\frac{N(\phi^*,\sigma(\leftarrow\Rightarrow))}{\Lambda_z(\Rightarrow)F(\Rightarrow)} &\sim \Big\{\Big(\frac{1}{\Lambda_z(\Rightarrow)}+\mathbf{P_z}\Big)-\frac{\bar{\delta}_\odot}{\Lambda_z(\Rightarrow)}\mathbf{I}^\odot-\bar{\delta}_\odot\mathbf{P_z^\odot}\Big\}\\
\frac{N(\phi^*,\sigma(\rightarrow\Leftarrow))}{\Lambda_z(\Leftarrow)F(\Leftarrow)} &\sim \Big\{\Big(\frac{1}{\Lambda_z(\Leftarrow)}-\mathbf{P_z}\Big)+\frac{\bar{\delta}_\odot}{\Lambda_z(\Leftarrow)}\mathbf{I}^\odot-\bar{\delta}_\odot\mathbf{P_z^\odot}\Big\}\\
\frac{N(\phi^*,\sigma(\leftarrow\Leftarrow))}{\Lambda_z(\Leftarrow)F(\Leftarrow)} &\sim \Big\{\Big(\frac{1}{\Lambda_z(\Leftarrow)}-\mathbf{P_z}\Big)-\frac{\bar{\delta}_\odot}{\Lambda_z(\Leftarrow)}\mathbf{I}^\odot+\bar{\delta}_\odot\mathbf{P_z^\odot}\Big\}.
\end{aligned} \tag{33}$$

Figure 37 shows examples of these angular distributions for the four different polarization combinations (Equation 28). In the next step, the distributions in Figure 37 (a) and (b) have been added,

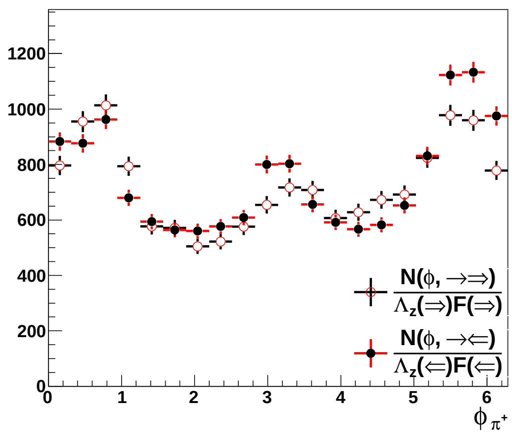

(a) $N(\phi^*, \rightarrow)$

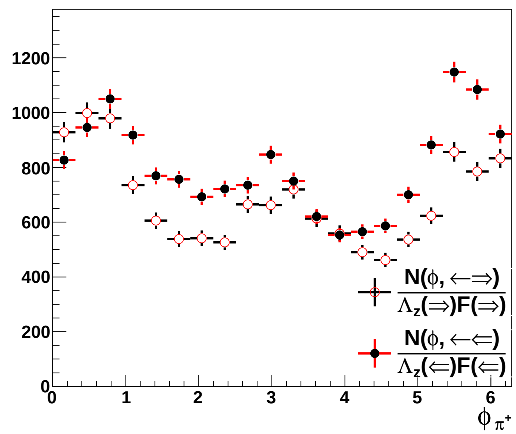

(b) $N(\phi^*, \leftarrow)$

Figure 37: Examples of ϕ^* angular distributions in the helicity frame of the beam polarization parallel (a) and anti-parallel (b) to the beam axis for the center-of-mass energy $W \in [1.675, 1.725]$ GeV and for the Topology $\gamma p \rightarrow p\pi^+(\pi^-)$. The data using the target polarization parallel (antiparallel) to the beam axis are from Period 6 (Period 7).

respectively, to produce an unpolarized target. Figure 38 shows examples of these distributions:

$$\begin{aligned}
N(\phi^*, \sigma(\rightarrow)) &\sim \frac{N(\phi^*, \sigma(\rightarrow\Rightarrow))}{\Lambda_z(\Rightarrow)F(\Rightarrow)} + \frac{N(\phi^*, \sigma(\rightarrow\Leftarrow))}{\Lambda_z(\Leftarrow)F(\Leftarrow)} \sim \left(\frac{1}{\Lambda_z(\Rightarrow)} + \frac{1}{\Lambda_z(\Leftarrow)}\right)\left(1 + \bar{\delta}_\odot \mathbf{I}^\odot\right), \\
N(\phi^*, \sigma(\leftarrow)) &\sim \frac{N(\phi^*, \sigma(\leftarrow\Rightarrow))}{\Lambda_z(\Rightarrow)F(\Rightarrow)} + \frac{N(\phi^*, \sigma(\leftarrow\Leftarrow))}{\Lambda_z(\Leftarrow)F(\Leftarrow)} \sim \left(\frac{1}{\Lambda_z(\Rightarrow)} + \frac{1}{\Lambda_z(\Leftarrow)}\right)\left(1 - \bar{\delta}_\odot \mathbf{I}^\odot\right).
\end{aligned} \tag{34}$$

The beam asymmetry can be calculated using the number of events for the helicity plus and minus from Equation 34. Since the effect for the electron beam charge asymmetry in the g9a dataset is negligible, it is not applied to the beam asymmetry (see Appendix B). An example of the polarization observable $\mathbf{I}^\odot$ is shown in Figure 38 (right) using the normalization factor $F(\Rightarrow)/F(\Leftarrow)$ from Table 15. In summary, the observable is given by:

$$\mathbf{I}^\odot = \frac{1}{\bar{\delta}_\odot} \frac{\left(\frac{N(\phi^*,\sigma(\rightarrow\Rightarrow))}{\Lambda_z(\Rightarrow)\cdot F(\Rightarrow)/F(\Leftarrow)} + \frac{N(\phi^*,\sigma(\rightarrow\Leftarrow))}{\Lambda_z(\Leftarrow)}\right) - \left(\frac{N(\phi^*,\sigma(\leftarrow\Rightarrow))}{\Lambda_z(\Rightarrow)\cdot F(\Rightarrow)/F(\Leftarrow)} + \frac{N(\phi^*,\sigma(\leftarrow\Leftarrow))}{\Lambda_z(\Leftarrow)}\right)}{\left(\frac{N(\phi^*,\sigma(\rightarrow\Rightarrow))}{\Lambda_z(\Rightarrow)\cdot F(\Rightarrow)/F(\Leftarrow)} + \frac{N(\phi^*,\sigma(\rightarrow\Leftarrow))}{\Lambda_z(\Leftarrow)}\right) + \left(\frac{N(\phi^*,\sigma(\leftarrow\Rightarrow))}{\Lambda_z(\Rightarrow)\cdot F(\Rightarrow)/F(\Leftarrow)} + \frac{N(\phi^*,\sigma(\leftarrow\Leftarrow))}{\Lambda_z(\Leftarrow)}\right)}. \tag{35}$$

4.2.2 Average Beam Asymmetry

Since the g9a dataset is broken up into different periods (Table 14), we have used three kinds of period combinations to calculate the beam asymmetry: Periods 3 and 2 (called combination-32), Periods 4 and 5 (called combination-45), and Periods 6 and 7 (called combination-67). Double-pion photoproduction is also based on four kinds of topologies:

- Topology 1: $\bar{\gamma}\bar{p} \rightarrow p\pi^+(\pi^-)$ (π^- not detected)

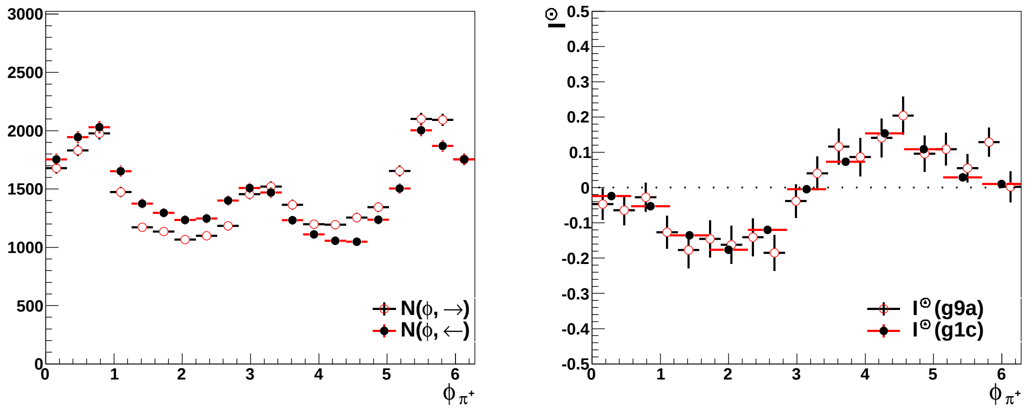

Figure 38: Left: CLAS-integrated azimuthal angular distributions for helicity-plus events $N(\phi^*, \rightarrow)$ and helicity-minus events $N(\phi^*, \leftarrow)$ for the center-of-mass energy $W \in [1.675, 1.725]$ GeV and the Topology $\gamma p \rightarrow p\pi^+(\pi^-)$. Right: The polarization observable $\mathbf{I}^\odot$ calculated from Equation 35. It is compared to the same observable published from the CLAS-g1c experiment. The dataset is the same as in Figure 37; Periods 6 and 7 have been used.

- Topology 2: $\bar{\gamma}\bar{p} \rightarrow p\pi^-(\pi^+)$ (π^+ not detected)
- Topology 3: $\bar{\gamma}\bar{p} \rightarrow \pi^+\pi^-(p)$ (proton not detected)
- Topology 4: $\bar{\gamma}\bar{p} \rightarrow p\pi^+\pi^-$ (all particles detected)

Since the CLAS spectrometer is designed to detect charged particles, we cannot distinguish between the reactionS $\gamma p \rightarrow o\pi^+\pi^-$ and $\gamma n \rightarrow n\pi^+\pi^-$ using the butanol target. The missing-mass distribution for the Topology $\gamma p \rightarrow \pi^+\pi^-(p)$, shown in Figure 15, includes the data from the reaction $\gamma p \rightarrow \pi^+\pi^-\,(p)$ and from the reaction $\gamma n \rightarrow \pi^+\pi^-\,(n)$ together, and this analysis cannot distinguish between the datasets for the reactions γp and γn. For this reason, the Topology $\gamma p \rightarrow \pi^+\pi^-\,(p)$ has been excluded in this analysis. The beam asymmetries from the three kinds of period combinations and the three kinds of topologies (Table 17) have been determined.

Topology 1: $\gamma p \rightarrow p\pi^+(\pi^-)$	combination-32
	combination-45
	combination-67
Topology 2: $\gamma p \rightarrow p\pi^-(\pi^+)$	combination-32
	combination-45
	combination-67
Topology 4: $\gamma p \rightarrow p\pi^+\pi^-$	combination-32
	combination-45
	combination-67

Table 17: The datasets used to calculate the average observable $\mathbf{I}^\odot$.

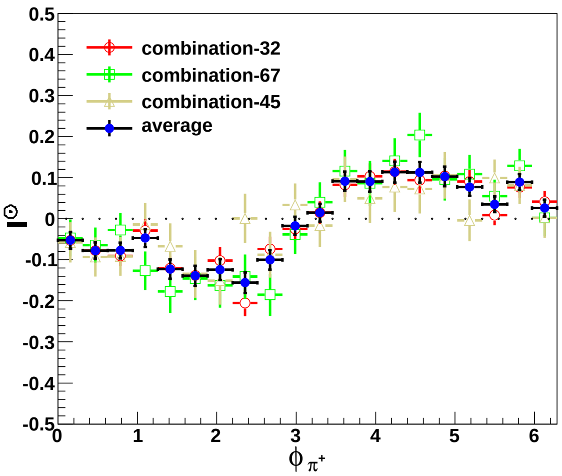

(a) Topology 1: $\gamma p \to p\pi^+(\pi^-)$

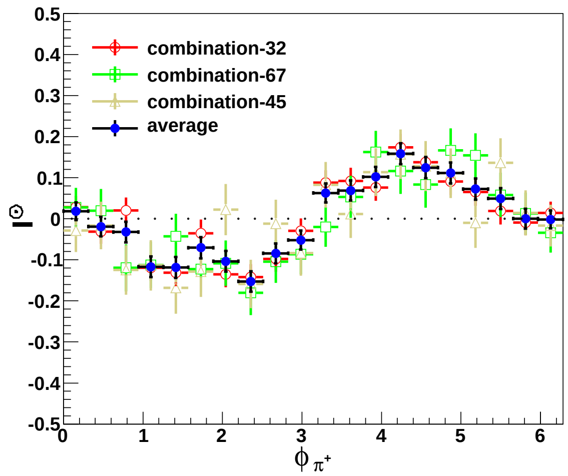

(b) Topology 2: $\gamma p \to p\pi^-(\pi^+)$

Figure 39: Polarization observables $\mathbf{I}^\odot$ from the three kinds of period-combinations in the Topology $\gamma p \to p\pi^+(\pi^-)$ (a) and the Topology $\gamma p \to p\pi^-(\pi^+)$ (b) for the center-of-mass energy $W \in [1.675, 1.725]$ GeV and their average in each topology. The polarization observable $\mathbf{I}^\odot$ in each period combination and each topology is derived from Equation 35.

Figure 38 (right) shows the comparison of the observable $\mathbf{I}^\odot$ from the g9a and g1c experiments. In the figure, the polarization observable $\mathbf{I}^\odot$ from the g9a dataset is made from combination-67 and Topology $\gamma p \to p\pi^+(\pi^-)$. In the next step, the average of the observables from the three different period combinations for each topology has been calculated to improve statistics. This is shown in Figure 39. The observables of the combination-32, combination-45, and combination-67 have statistical errors of different magnitudes. These statistical errors have been used as squared weights when the observables were averaged:

$$\bar{x} = \frac{\sum_i x_i \cdot \frac{1}{\sigma_i^2}}{\sum_i \frac{1}{\sigma_i^2}}, \tag{36}$$

where x_i is the observable and σ_i is its error.

To further improve the statistics and also to obtain better kinematic coverage, the results from Topologies 1, 2, and 4 have been averaged using Equation 36. This final observable from the butanol data is shown in Figure 40, together with the data published from the g1c experiment. Results of this analysis are in general very good agreement with the data published in [17] (see also Appendix C).

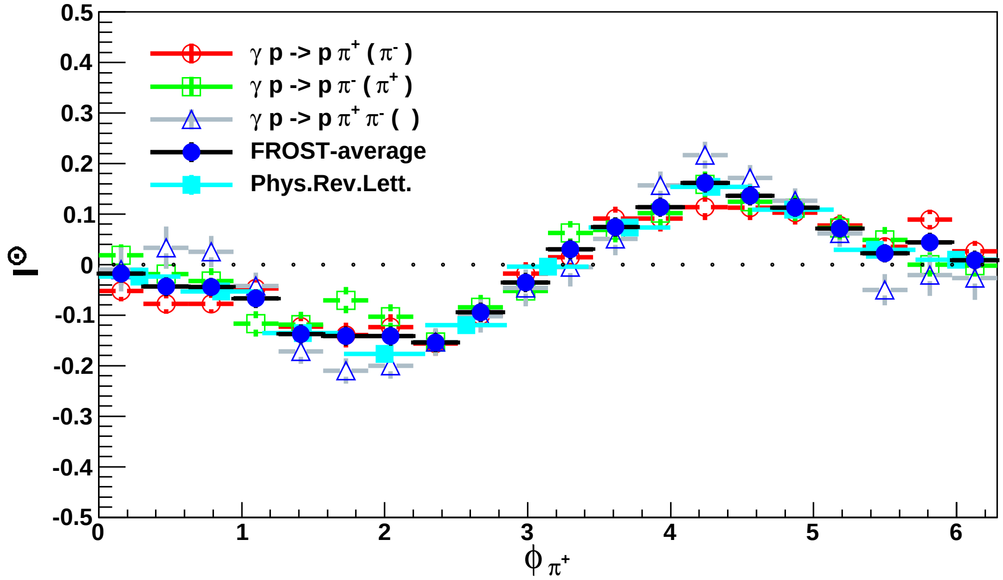

Figure 40: The beam asymmetries from the Topologies 1, 2, and 4 and the average of the three topologies, called FROST-average, for the center-of-mass energy $W \in [1.675, 1.725]$ GeV. The polarization observable $\mathbf{I}^{\odot}$ from this analysis is also compared to the results published in [17].

Comparisons

For different period combinations and topologies, we have compared the results to check consistency. Figure 41 (a)-(c) shows the differences ($\mathbf{I}^{\odot}{}_{\text{combination X}} - \mathbf{I}^{\odot}{}_{\text{combination Y}}$) for the three kinds of period combinations. Figure 42 (a)-(c) shows the differences ($\mathbf{I}^{\odot}{}_{\text{Topology X}} - \mathbf{I}^{\odot}{}_{\text{Topology Y}}$) for the different topologies integrated over all kinematic bins. Figure 42 (d) shows the differences ($\mathbf{I}^{\odot}{}_{\mathbf{g9a}} - \mathbf{I}^{\odot}{}_{\mathbf{g1c}}$) of the polarization observable $\mathbf{I}^{\odot}$ from this analysis and previous published CLAS data. The distributions are all centered at zero and show very good agreement.

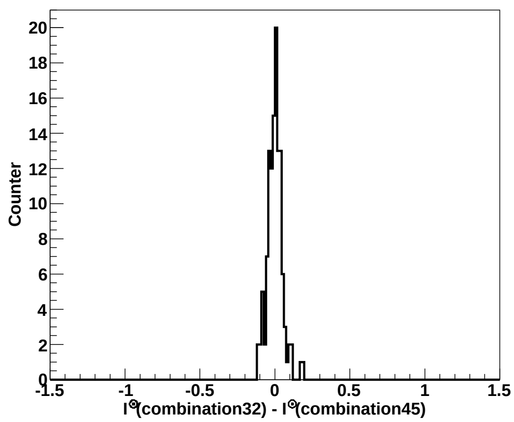

(a) Comparison of combination-32 and 45

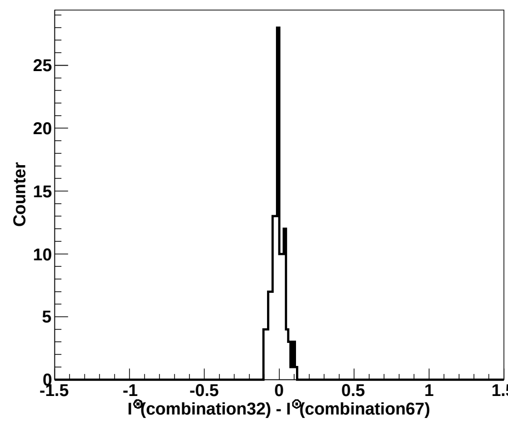

(b) Comparison of combination-32 and 67

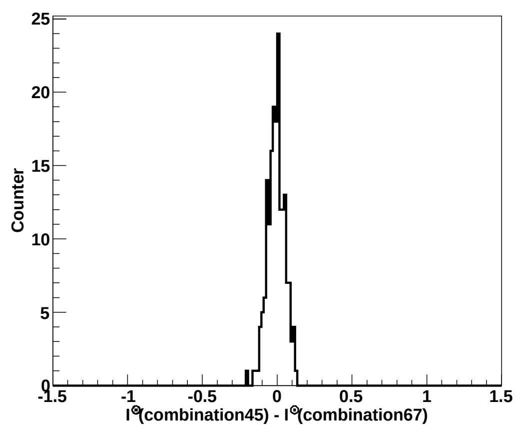

(c) Comparison of combination-45 and 67

Figure 41: Comparisons (differences) of results for the polarization observables $\mathbf{I}^{\odot}$ from different period combinations integrated over all energies for Topology $\gamma p \to p\pi^+(\pi^-)$. The distributions are all centered at zero, suggesting very good consistency among the results from different period combinations.

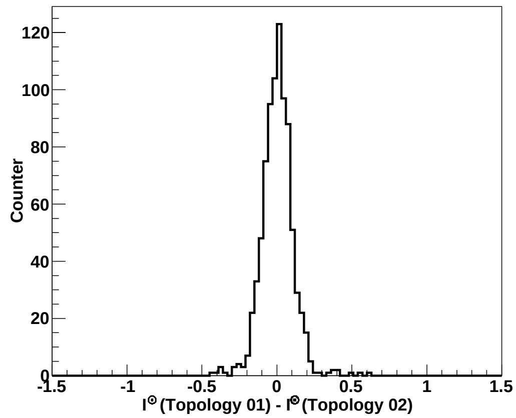

(a) Comparison of Topologies 1 and 2

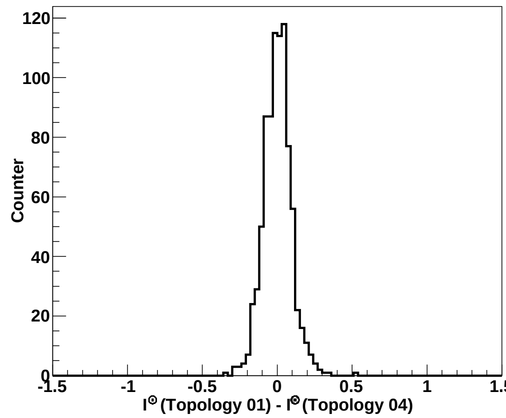

(b) Comparison of Topologies 1 and 4

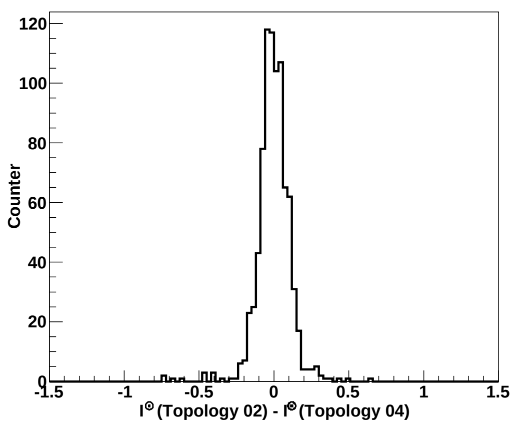

(c) Comparison of Topologies 2 and 4

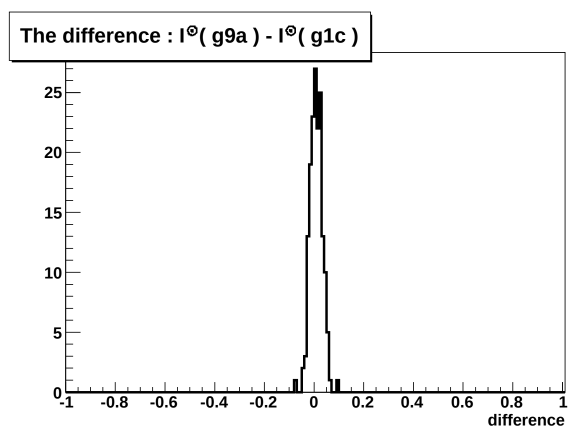

(d) Comparison of g9a and g1c

Figure 42: (a)-(c) Comparisons (differences) of results for the polarization observables $\mathbf{I}^{\odot}$ from different topologies integrated over all energies. The distributions are all fairly narrow and centered at zero, suggesting very good consistency among the results from different topologies. (d) Comparison (difference) of results for the polarization observables $\mathbf{I}^{\odot}$ from this analysis and from the g1c experiment, integrated over all energies. The results are in excellent agreement.

4.3 Polarization Observable $\mathbf{P_z}$

4.3.1 Target Asymmetry

The target asymmetry as a function of ϕ^* is given by:

$$\mathbf{T.Asy.} = \frac{N(\phi^*, \sigma(\Rightarrow)) - N(\phi^*, \sigma(\Leftarrow))}{N(\phi^*, \sigma(\Rightarrow)) + N(\phi^*, \sigma(\Leftarrow))}\,. \tag{37}$$

To calculate the target asymmetry, the polarized free-proton events of the full butanol data must be extracted. In the numerator of Equation 37, unpolarized events will cancel out. However, there are still unpolarized events in the denominator of Equation 37 (normalization). Since the Q-factor is defined as an event-based dilution factor, the number of Q-factor weighted butanol events, $N(\phi^*,\,\sigma(\rightarrow\Rightarrow))^Q$, denotes the number of the free-proton events. The event distributions of the four different data combinations, shown in Figure 43, are given by (equivalent to Equation 30):

$$\begin{aligned}
\frac{N(\phi^*, \sigma(\rightarrow\Rightarrow))^Q}{F(\Rightarrow)} &\sim \Big(1 + \bar{\Lambda}_z(\Rightarrow)\cdot\mathbf{P_z}\Big) + \bar{\delta}_\odot\cdot\mathbf{I}^\odot + \delta_\odot\cdot\bar{\Lambda}_z(\Rightarrow)\cdot\mathbf{P_z^\odot}\\
\frac{N(\phi^*, \sigma(\leftarrow\Rightarrow))^Q}{F(\Rightarrow)} &\sim \Big(1 + \bar{\Lambda}_z(\Rightarrow)\cdot\mathbf{P_z}\Big) - \bar{\delta}_\odot\cdot\mathbf{I}^\odot - \delta_\odot\cdot\bar{\Lambda}_z(\Rightarrow)\cdot\mathbf{P_z^\odot}\\
\frac{N(\phi^*, \sigma(\rightarrow\Leftarrow))^Q}{F(\Leftarrow)} &\sim \Big(1 - \bar{\Lambda}_z(\Leftarrow)\cdot\mathbf{P_z}\Big) + \bar{\delta}_\odot\cdot\mathbf{I}^\odot - \delta_\odot\cdot\bar{\Lambda}_z(\Leftarrow)\cdot\mathbf{P_z^\odot}\\
\frac{N(\phi^*, \sigma(\leftarrow\Leftarrow))^Q}{F(\Leftarrow)} &\sim \Big(1 - \bar{\Lambda}_z(\Leftarrow)\cdot\mathbf{P_z}\Big) - \bar{\delta}_\odot\cdot\mathbf{I}^\odot + \delta_\odot\cdot\bar{\Lambda}_z(\Leftarrow)\cdot\mathbf{P_z^\odot}\,.
\end{aligned} \tag{38}$$

Since the polarization observable $\mathbf{P_z}$ refers to unpolarized beam data, a dataset with a longitudinally-polarized target and an unpolarized beam is required. We can easily produce an unpolarized-beam dataset by adding the data with different beam polarizations from Equation 38. Figure 44 shows examples of these distributions given by $N(\phi^*, \sigma(\Rightarrow))^Q$ and $N(\phi^*, \sigma(\Leftarrow))^Q$:

$$\begin{aligned}
N(\phi^*, \sigma(\Rightarrow))^Q &\sim \frac{N(\phi^*, \sigma(\rightarrow\Rightarrow))^Q}{F(\Rightarrow)} + \frac{N(\phi^*, \sigma(\leftarrow\Rightarrow))^Q}{F(\Rightarrow)} \sim 2 + 2\cdot\bar{\Lambda}_z(\Rightarrow)\cdot\mathbf{P_z}\,,\\
N(\phi^*, \sigma(\Leftarrow))^Q &\sim \frac{N(\phi^*, \sigma(\rightarrow\Leftarrow))^Q}{F(\Leftarrow)} + \frac{N(\phi^*, \sigma(\leftarrow\Leftarrow))^Q}{F(\Leftarrow)} \sim 2 - 2\cdot\bar{\Lambda}_z(\Leftarrow)\cdot\mathbf{P_z}\,.
\end{aligned} \tag{39}$$

The target asymmetry derived from these unpolarized-beam datasets is given by:

$$\begin{aligned}
\mathbf{T.Asy.} &= \frac{\left(\frac{N(\phi^*,\sigma(\rightarrow\Rightarrow))}{F(\Rightarrow)/F(\Leftarrow)} + \frac{N(\phi^*,\sigma(\leftarrow\Rightarrow))}{F(\Rightarrow)/F(\Leftarrow)}\right) - \left(\frac{N(\phi^*,\sigma(\rightarrow\Leftarrow))}{1} + \frac{N(\phi^*,\sigma(\leftarrow\Leftarrow))}{1}\right)}{\left(\frac{N(\phi^*,\sigma(\rightarrow\Rightarrow))^Q}{F(\Rightarrow)/F(\Leftarrow)} + \frac{N(\phi^*,\sigma(\leftarrow\Rightarrow))^Q}{F(\Rightarrow)/F(\Leftarrow)}\right) + \left(\frac{N(\phi^*,\sigma(\rightarrow\Leftarrow))^Q}{1} + \frac{N(\phi^*,\sigma(\leftarrow\Leftarrow))^Q}{1}\right)}\\
&= \frac{\bar{\Lambda}_z(\Rightarrow) + \bar{\Lambda}_z(\Leftarrow)}{2}\cdot\mathbf{P_z}\,.
\end{aligned} \tag{40}$$

and the polarization observable $\mathbf{P_z}$ is shown in Figure 45 for combination-67 and Topology 1, $\gamma p \to p\pi^+\,(\pi^-)$.

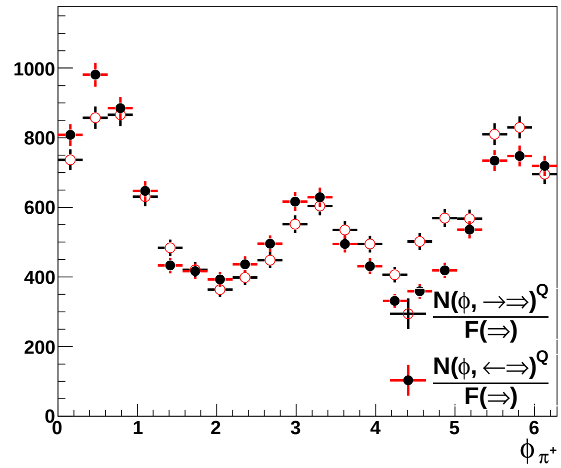

(a) $N(\phi^*, \Rightarrow)$

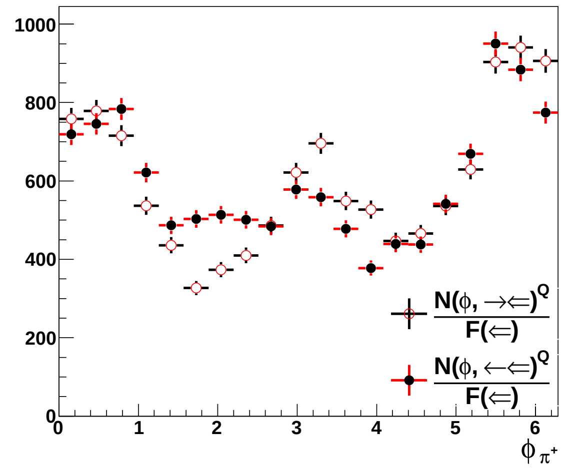

(b) $N(\phi^*, \Leftarrow)$

Figure 43: Examples of $\phi^*_{\pi^+}$ angular distributions for the target polarization parallel (a) and antiparallel (b) to the beam axis. The data are selected for $W \in [1.725, 1.775]$ GeV, combination-67, and Topology $\gamma p \to p\pi^+(\pi^-)$. This figure is similar to Figure 37; the distributions here are shown for a different W bin and not corrected for the degree of the target polarization.

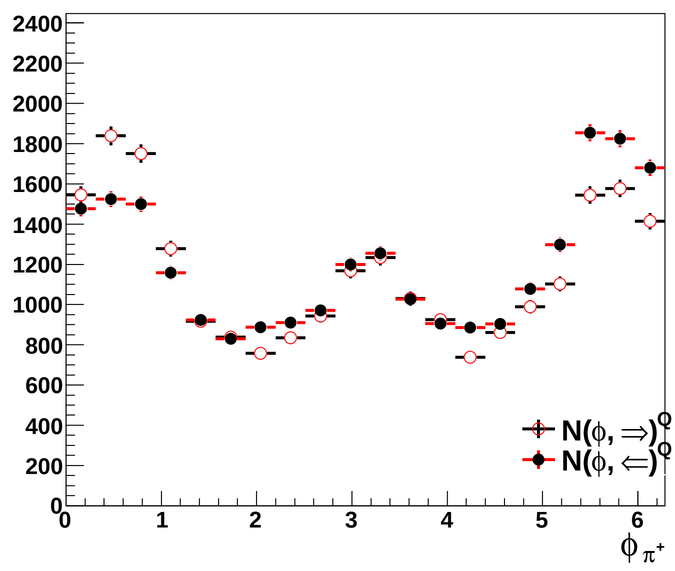

Figure 44: Azimuthal angular distributions for $N(\phi^*, \Rightarrow)^Q$ and $N(\phi^*, \Leftarrow)^Q$ for the center-of-mass energy $W \in [1.725, 1.775]$ GeV and the Topology $\gamma p \to p\pi^+(\pi^-)$ integrated over the beam-helicity states. A normalization is not necessary.

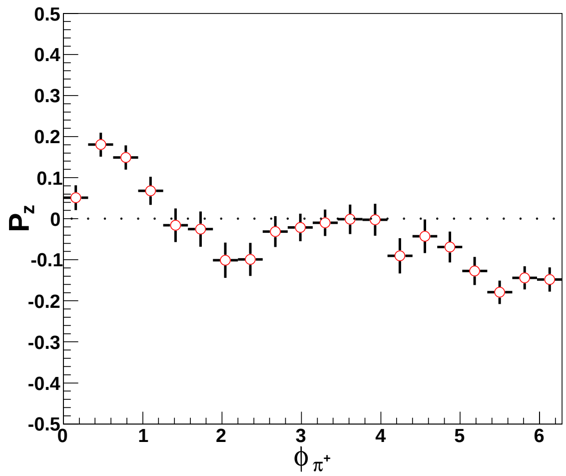

Figure 45: The polarization observable $\mathbf{P_z}$ calculated from Equation 40. The data used here are the same as the ones used in Figure 44.

4.3.2 Average Target Asymmetry

The target asymmetry can be calculated from the three kinds of period combinations and the three kinds of topologies, listed in Table 18, which is similar to calculating the average of the observable $\mathbf{I}^{\odot}$ in Section 4.2.2. As a matter of fact, Table 18 is identical to Table 17 but we repeat it here for a complete discussion of $\mathbf{P_z}$.

Topology 1: $\gamma p \to p\pi^+(\pi^-)$	combination-32
	combination-45
	combination-67
Topology 2: $\gamma p \to p\pi^-(\pi^+)$	combination-32
	combination-45
	combination-67
Topology 4: $\gamma p \to p\pi^+\pi^-$	combination-32
	combination-45
	combination-67

Table 18: The datasets used to calculate the average observable $\mathbf{P_z}$.

Figure 45 shows the polarization observable $\mathbf{P_z}$ from combination-67 and Topology $\gamma p \to p\pi^+(\pi^-)$. In Figure 46, each topology is based on the average of combination-32, combination-45, and combination-67 using again Equation 36. Figure 47 shows the average value of the observable $\mathbf{P_z}$ calculated from Topology $\gamma p \to p\pi^+(\pi^-)$ and Topology $\gamma p \to p\pi^-(\pi^+)$, as shown in Figure 46 for the center-of-mass energy $W \in [1.725, 1.775]$ GeV.

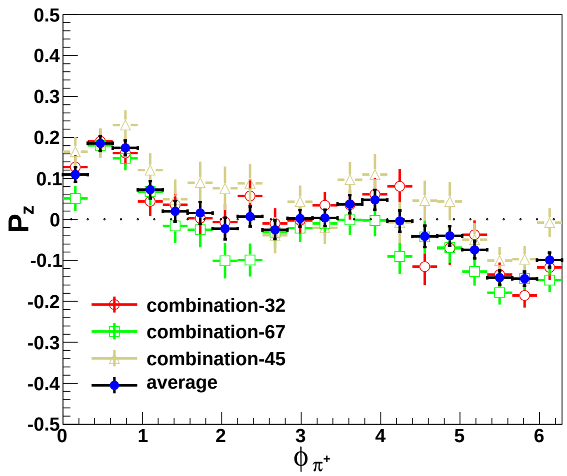

(a) Topology 1: $\gamma p \to p\pi^+(\pi^-)$

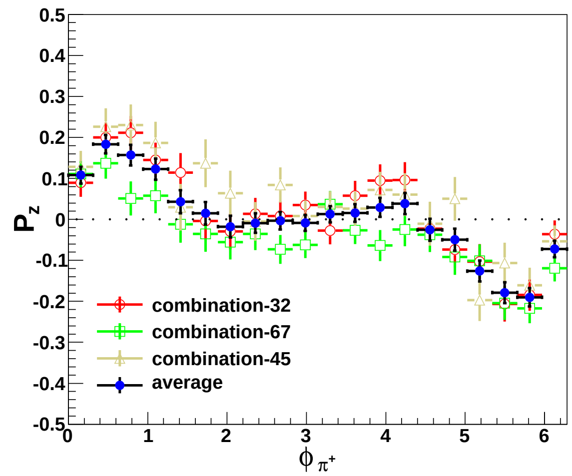

(b) Topology 2: $\gamma p \to p\pi^-(\pi^+)$

Figure 46: Polarization observables $\mathbf{P_z}$ based on the three kinds of period combinations for Topology $\gamma p \to p\pi^+(\pi^-)$ (a) and Topology $\gamma p \to p\pi^-(\pi^+)$ (b) for the center-of-mass energy $W \in [1.725, 1.775]$ GeV and their averages for each topology.

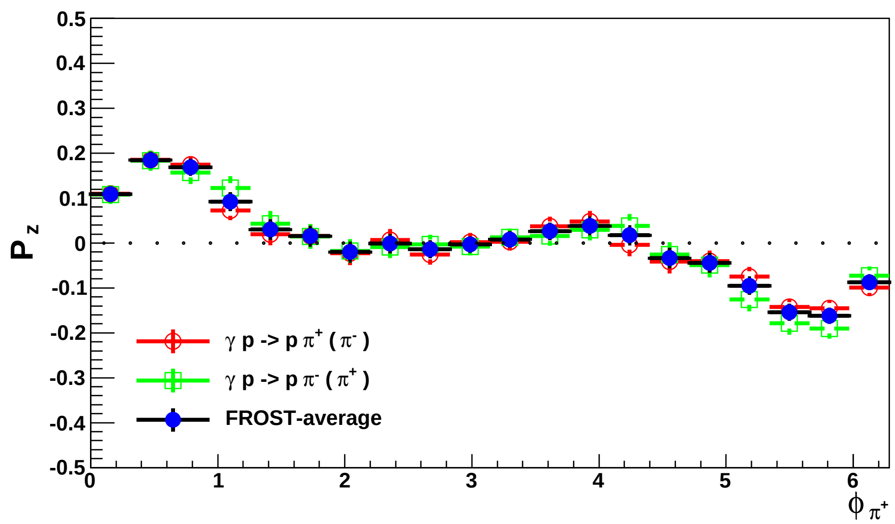

Figure 47: The average target asymmetry for the Topologies 1 and 2 based on the three kinds of period combinations, respectively, and their average, called FROST-average. The data are shown for the center-of-mass energy $W \in [1.725, 1.775]$ GeV and are the same as the ones used in Figure 46.

Comparisons

For the different period combinations and topologies, we have compared the results to ensure good consistency. Figure 48 shows the differences ($\mathbf{P_z}_{\,\text{combination}\,X} - \mathbf{P_z}_{\,\text{combination}\,Y}$) for the three kinds of period combinations, and Figure 49 the differences ($\mathbf{P_z}_{\text{Topology}\,X} - \mathbf{P_z}_{\text{Topology}\,Y}$) for the different topologies integrated over all kinematic bins. The distributions are all narrow and centered at zero. They show very good agreement.

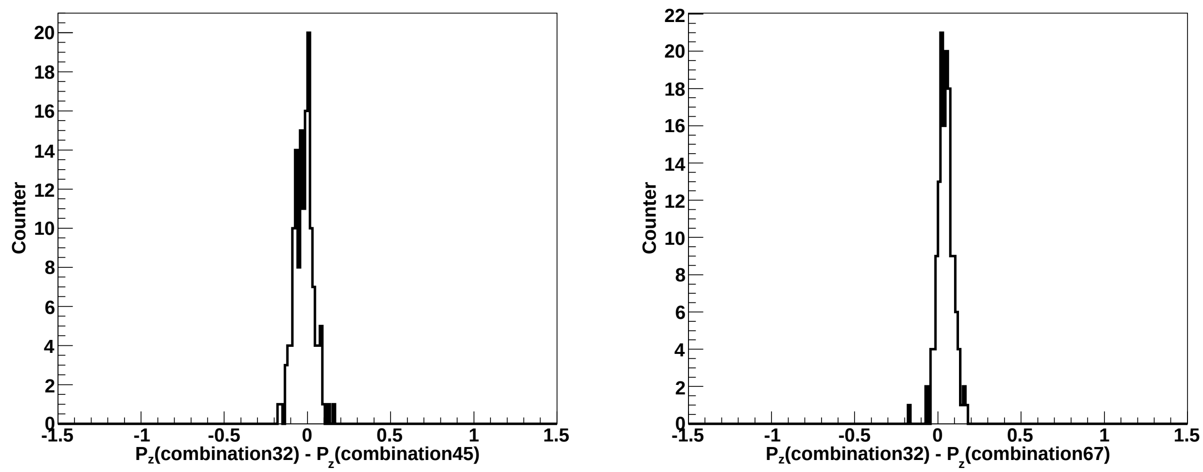

Figure 48: Comparisons (differences) of results for the polarization observable $\mathbf{P_z}$ from different period combinations integrated over all energies for Topology $\gamma p \to p\pi^+(\pi^-)$.

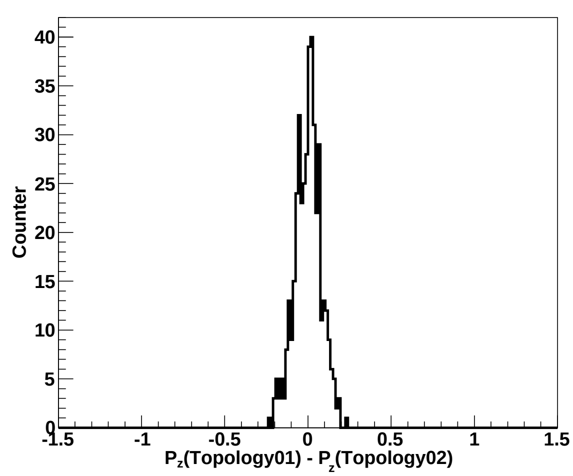

Figure 49: Comparison (difference) of results for the polarization observables $\mathbf{I}^{\odot}$ from different topologies integrated over all energies.

4.4 Polarization Observable $\mathbf{P_z^\odot}$

4.4.1 Helicity Difference

In the calculation of the helicity difference, again the average target polarization was used. Table 12 shows the average degree of target polarization for all periods. The degree of target polarization of Periods 4 and 5 is similar. Periods 6 and 7 also have similar values. However, the polarization for Periods 2 and 3 is slightly different. When the average target polarization for $\Lambda_z(\Rightarrow)$ and $\Lambda_z(\Leftarrow)$ is used in the calculation of the helicity difference, the target asymmetry, $\mathbf{P_z}$, from combination-32 has a negligible influence on the observable $\mathbf{P_z^\odot}$. The event distributions of the four different datasets are given by Equation 38.

The double polarization observable $\mathbf{P_z^\odot}$ refers to the dataset with a longitudinally-polarized target and circularly-polarized beam. The events with spin 3/2, $N(\phi^*, \sigma_{3/2})$, and spin 1/2, $N(\phi^*, \sigma_{1/2})$, are given by:

$$\begin{aligned} N(\phi^*, \sigma_{3/2}) &\sim \frac{N(\phi^*, \rightarrow\Rightarrow)}{F(\Rightarrow)} + \frac{N(\phi^*, \leftarrow\Leftarrow)}{F(\Leftarrow)} \sim 2 + 2 \cdot \bar{\delta}_\odot \cdot \bar{\Lambda}_z \cdot \mathbf{P_z^\odot}\,, \\ N(\phi^*, \sigma_{1/2}) &\sim \frac{N(\phi^*, \leftarrow\Rightarrow)}{F(\Rightarrow)} + \frac{N(\phi^*, \rightarrow\Leftarrow)}{F(\Leftarrow)} \sim 2 - 2 \cdot \bar{\delta}_\odot \cdot \bar{\Lambda}_z \cdot \mathbf{P_z^\odot}\,. \end{aligned} \tag{41}$$

Examples of these distributions are shown in Figure 50 for $W \in [1.675, 1.725]$ GeV and the Topology $\gamma p \to p\pi^+(\pi^-)$.

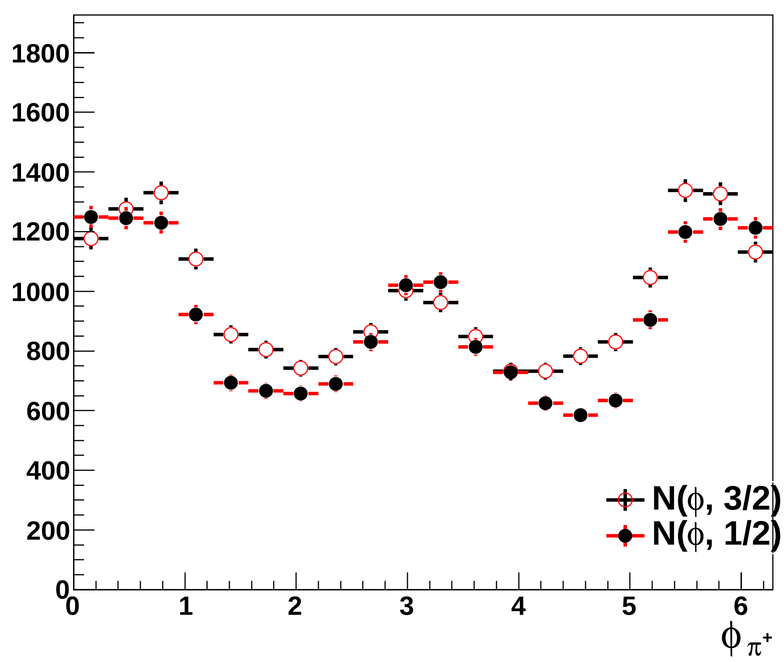

Figure 50: Azimuthal angular distributions for $N(\phi^*, 3/2)$ and $N(\phi^*, 1/2)$ for the center-of-mass energy bin $W \in [1.675, 1.725]$ GeV and the Topology $\gamma p \to p\pi^+(\pi^-)$.

The polarization observable $\mathbf{P_z^{\odot}}$ (Figure 51) is given by (similar to Equations 35 and 40):

$$\mathbf{P_z^{\odot}} = \frac{1}{\bar{\delta}_{\odot} \cdot \bar{\Lambda}_z} \frac{\left(\frac{N(\phi^*,\rightarrow\Rightarrow)}{F(\Rightarrow)/F(\Leftarrow)} + \frac{N(\phi^*,\leftarrow\Leftarrow)}{1}\right) - \left(\frac{N(\phi^*,\leftarrow\Rightarrow)}{F(\Rightarrow)/F(\Leftarrow)} + \frac{N(\phi^*,\rightarrow\Leftarrow)}{1}\right)}{\left(\frac{N(\phi^*,\rightarrow\Rightarrow)^Q}{F(\Rightarrow)/F(\Leftarrow)} + \frac{N(\phi^*,\leftarrow\Leftarrow)^Q}{1}\right) + \left(\frac{N(\phi^*,\leftarrow\Rightarrow)^Q}{F(\Rightarrow)/F(\Leftarrow)} + \frac{N(\phi^*,\rightarrow\Leftarrow)^Q}{1}\right)}. \tag{42}$$

4.4.2 Average Helicity Difference

The helicity difference can also be calculated from the three kinds of period combinations and the three kinds of topologies, listed in Tables 17 or 18, similar to calculating the averages of the observables $\mathbf{I}^{\odot}$ and $\mathbf{P_z}$ in the previous sections.

Figure 51 shows an example of the polarization observable $\mathbf{P_z^{\odot}}$ from combination-67 and Topology $\gamma p \rightarrow p\pi^+(\pi^-)$. In Figure 52, each topology is based on the average of combination-32, combination-45, and combination-67 using again Equation 36. Figure 53 shows the average value of the observable $\mathbf{P_z^{\odot}}$ calculated for Topology $\gamma p \rightarrow p\pi^+(\pi^-)$ and Topology $\gamma p \rightarrow p\pi^-(\pi^+)$ for the center-of-mass energy $W \in [1.675,\ 1.725]$ GeV. Figure 61 shows the average value of the observable $\mathbf{P_z^{\odot}}$ for the whole energy range $W \in [1.375,\ 2.125]$ GeV.

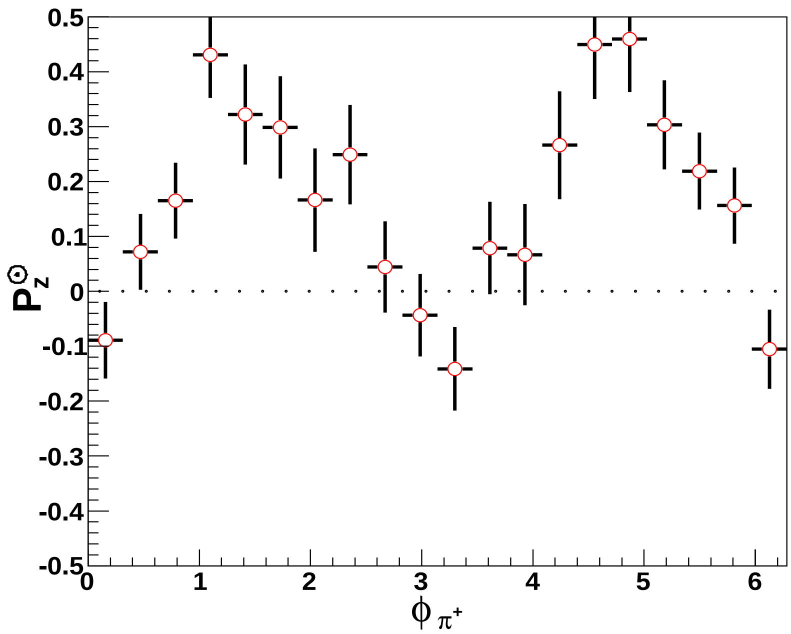

Figure 51: The polarization observable $\mathbf{P_z^{\odot}}$ calculated from Equation 42. The data used here are the same as the ones in Figure 50.

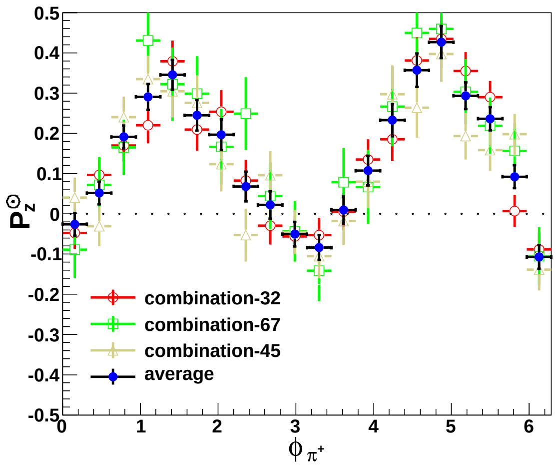

(a) Topology 1: $\gamma p \to p\pi^+(\pi^-)$

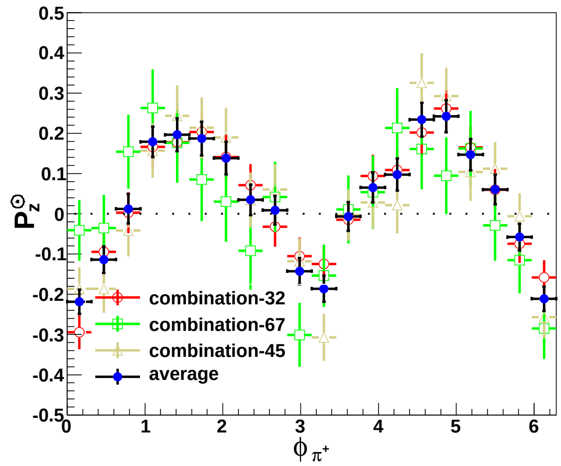

(b) Topology 2: $\gamma p \to p\pi^-(\pi^+)$

Figure 52: Polarization observable $\mathbf{P_z^{\odot}}$ from the three kinds of period combinations for Topology $\gamma p \to p\pi^+(\pi^-)$ (a) and Topology $\gamma p \to p\pi^-(\pi^+)$ (b) for $W \in [1.675,\ 1.725]$ GeV and the average in each topology.

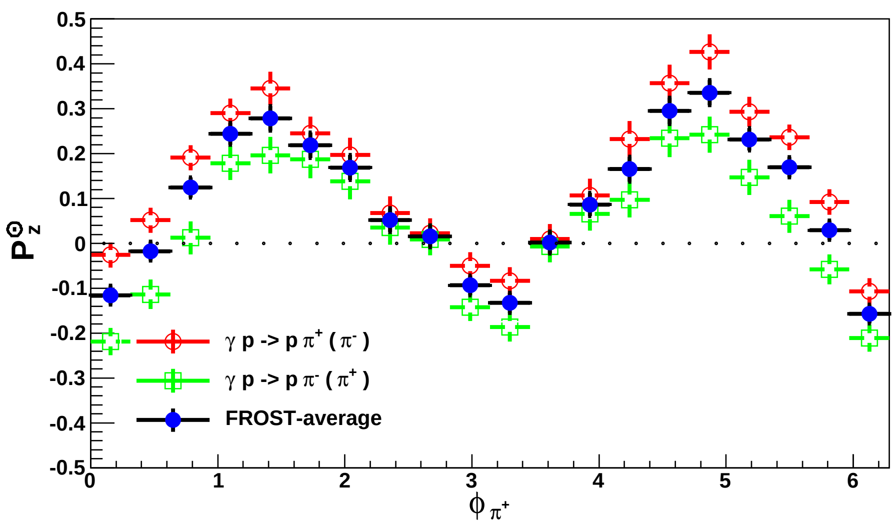

Figure 53: The average helicity difference of the Topology 1 and Topology 2 and their average, called FROST-average. The data are shown for the center-of-mass energy $W \in [1.675,\ 1.725]$ GeV.

Comparisons

For different period combinations and topologies, we have again compared the results to confirm the good consistency. Figure 54 shows the differences ($\mathbf{P_z^{\odot}}_{\,\text{combination}\,X} - \mathbf{P_z^{\odot}}_{\,\text{combination}\,Y}$) for the three kinds of period combinations, and Figure 55 shows the differences ($\mathbf{P_z^{\odot}}_{\,\text{Topology}\,X} - \mathbf{P_z^{\odot}}_{\,\text{Topology}\,Y}$) of different topologies integrated over all kinematic bins. The distributions are all very narrow and centered at zero and show good agreement.

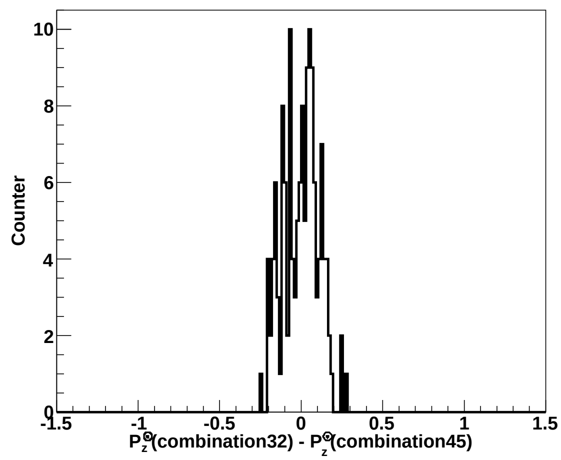

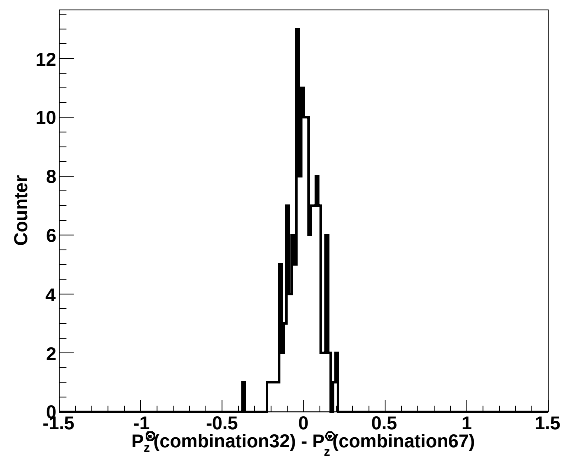

Figure 54: Comparisons (differences) of results for the polarization observable $\mathbf{P_z^{\odot}}$ from different period combinations integrated over all energies for Topology $\gamma p \to p\pi^+(\pi^-)$.

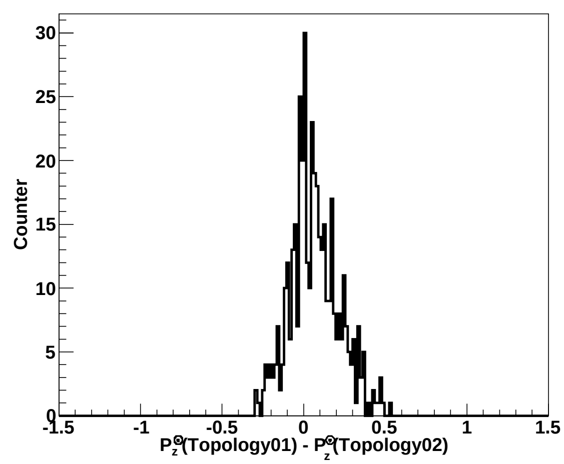

Figure 55: Comparison (difference) of results for the polarization observables $\mathbf{P_z^{\odot}}$ from different topologies integrated over all energies.

4.5 Systematic Uncertainties

Systematic uncertainties define errors which do not originate from limited statistics but are introduced by an inaccuracy in the measurement inherent to the system. Systematic errors of the experimental observations in the g9a experiment are usually based on instrumental effects: e.g. the beam polarization $\delta_{\odot}$, target polarization Λ_z, and normalization factor F from the photon beam flux. The contributions to the total systematic error are listed in Table 19 and have been carefully studied.

Contribution	ΔObs.	ΔObs./Obs.
Electron beam-charge asymmetry	< 0.004	
Circular polarization of photon beam		$< 0.2\,\%$
Target polarization		
Period combination-32		$< 1.0\,\%$
Period combination-45/67		$< 0.1\%$
Normalization (photon flux)		$< 0.4\,\%$
Accidentals		$< 2.5\,\%$
Q-factor method		$< 2.0\,\%$
Kinematic fitting (different CL cuts)		$< 1.5\,\%$

Table 19: Contributions to the total systematic uncertainty of the polarization observables.

The electron-beam helicity is flipped in the injector of the electron accelerator. Small beam-charge asymmetries of the electron beam can be one source of a systematic error. The contribution of the beam-charge asymmetry can be calculated from the difference between the polarization observable $\mathbf{I}^{\odot}$ before and after applying the effect of the electron beam charge asymmetry (see Appendix B).

4.5.1 Degree of Beam and Target Polarization, Normalization

The effect of these uncertainties on the polarization observables is very small and almost negligible. Table 19 gives upper limits but the associated systematic errors are even smaller on average. The errors for the degree of circular-beam polarization itself are given in Table 17, for the target polarization in Table 12. We have studied the influence on the beam-helicity difference, $\mathbf{I}^{\odot}$, by applying standard error propagation (see Appendix D) and applied the systematic errors on a kinematic bin-by-bin basis. Since these uncertainties are very small, we then applied the upper limits given in Table 19 to the target asymmetry and the helicity difference.

4.5.2 Accidental Background

The coincidence-time distribution after applying all the $\gamma p \to p\pi^+\pi^-$ selection cuts is shown in Figure 1 as black-filled histogram. The fraction of remaining accidental coincidences of at most $2.5\,\%$ within $|\Delta_{TGPB} < 1.2$ ns can be estimated from the comparison in the yields between the central peak in Figure 1 with neighboring beam buckets.

4.5.3 Kinematic Fitting

Since the asymmetries are normalized to the same data, the acceptance of the chosen kinematic variables drops out. Therefore, the choice of the applied confidence-level cut has only a small effect on the polarization observables. The effect is bigger for cross sections where the shape of the confidence-level distributions must be reproduced correctly in the Monte Carlo. We have used confidence-level cuts of 5 %, 10 %, and 15 % but found that the systematic effect is less than 1 %.

4.5.4 Q-Factor Method

Each fit used in the Q-factor method of background subtraction (Section 3.9.2) estimates an uncertainty for each parameter in the fit. When these uncertainties are propagated to the Q-factor, the resulting uncertainty will provide an estimate of how well determined the Q-factor itself is. Since the error of each parameter is linked to how well the fitting function describes the data, the uncertainty of the parameters is also an estimate of how well the fit does at modeling the invariant mass distribution. The method of propagating the error of the parameters to the uncertainty of each point in the polarization observable is taken from [14].

To propagate the error of the fit parameters to the Q-factor error ($\sqrt{\sigma_Q^2}$), the formula:

$$\sigma_Q^2 = \sum_{ij} \frac{\delta Q}{\delta \alpha_i} \left(C_\alpha\right)_{ij} \frac{\delta Q}{\delta \alpha_j} \tag{43}$$

has been used, where α_i is a fit parameter with index i and C_α is the covariance matrix which contains the errors of each fit parameter. The covariance matrix is calculated by and obtained from the RooFit fit package [15] used for fitting.

The propagation of these Q-factor errors to an uncertainty in the polarization observable is calculated by:

$$\sigma = \sum_{lk} \sqrt{\sigma_{Q_l}^2}\, \rho_{lk} \sqrt{\sigma_{Q_k}^2}\,, \tag{44}$$

where $\sqrt{\sigma_{Q_l}^2}$ is the Q-factor error for an event with index l and ρ_{lk} is the correlation factor between events with index l and k. The correlation factor is calculated by:

$$\rho_{lk} = \frac{N_{\text{common}}}{N_{nn}}\,, \tag{45}$$

where N_{nn} is the number of nearest neighbors used in Q-factor fitting and N_{common} is the number of those nearest neighbors which were used in both events l and k.

The Q-factor fitting uncertainties are mostly driven by statistics in some kinematic bins, in particular the number of available carbon events, which affects both the ratio in the fraction (Equation 21) but also the quality of the fit. If the fit covers too much phase space in the kinematic variables, the fit quality becomes poor. However, we observe relatively small systematic uncertainties on average.

4.5.5 Systematic Check of the Symmetry of the Observables

In this analysis, the dataset has been binned in two independent kinematical variables: the center-of-mass energy, W, and the azimuthal angle, $\phi^*_{\pi^+}$. As previously mentioned, the variable $\phi^*_{\pi^+}$ is the angle between the production plane (blue plane in Figure 36) and the decay plane (red plane in the same figure). Observables as function of $\phi^*_{\pi^+}$ exhibit either an odd or an even symmetry.

Figure 56 shows the polarization observable $\mathbf{I}^{\odot}$ for the whole energy range $W \in [1.375,\ 2.125]$ GeV. To check the symmetry of the observable $\mathbf{I}^{\odot}$, the transition $\phi^*_{\pi^+} \rightarrow 2\pi - \phi^*_{\pi^+}$ is performed: $\mathbf{I}^{\odot} = -\mathbf{I}^{\odot}(2\pi - \phi^*_{\pi^+})$. This is equivalent to applying a mirror operation with respect to the production plane, and then changing the sign of the asymmetry (Figure 56). The observable $\mathbf{I}^{\odot}$ exhibits the expected odd-symmetry behavior; the differences between the observables $\mathbf{I}^{\odot}(\phi^*_{\pi^+})$ and $-\mathbf{I}^{\odot}(2\pi - \phi^*_{\pi^+})$ show very small values.

Figure 57 and 58 present the polarization observables $\mathbf{P_z}$ and $\mathbf{P_z^{\odot}}$ for the whole energy range $W \in [1.375,\ 2.125]$ GeV, respectively. To also check the symmetries of the observables $\mathbf{P_z}$ and $\mathbf{P_z^{\odot}}$, the transition $\phi^*_{\pi^+} \rightarrow 2\pi - \phi^*_{\pi^+}$ has been applied, as for the observable $\mathbf{I}^{\odot}$. The observable $\mathbf{P_z}$ exhibits a similar odd symmetry. However, $\mathbf{P_z^{\odot}}$ is an even function of $\phi^*_{\pi^+}$, the mirror operation with respect to the production plane does not require a sign change as in the case of $\mathbf{I}^{\odot}$ and $\mathbf{P_z}$, i.e. $\mathbf{P_z^{\odot}} = \mathbf{P_z^{\odot}}(2\pi - \phi^*_{\pi^+})$ (Figure 58). The measured polarization observables $\mathbf{P_z}$ and $\mathbf{P_z^{\odot}}$ have overall well-defined symmetries; the differences between the observable and the observable after the transition $\phi^*_{\pi^+} \rightarrow 2\pi - \phi^*_{\pi^+}$ are all very small.

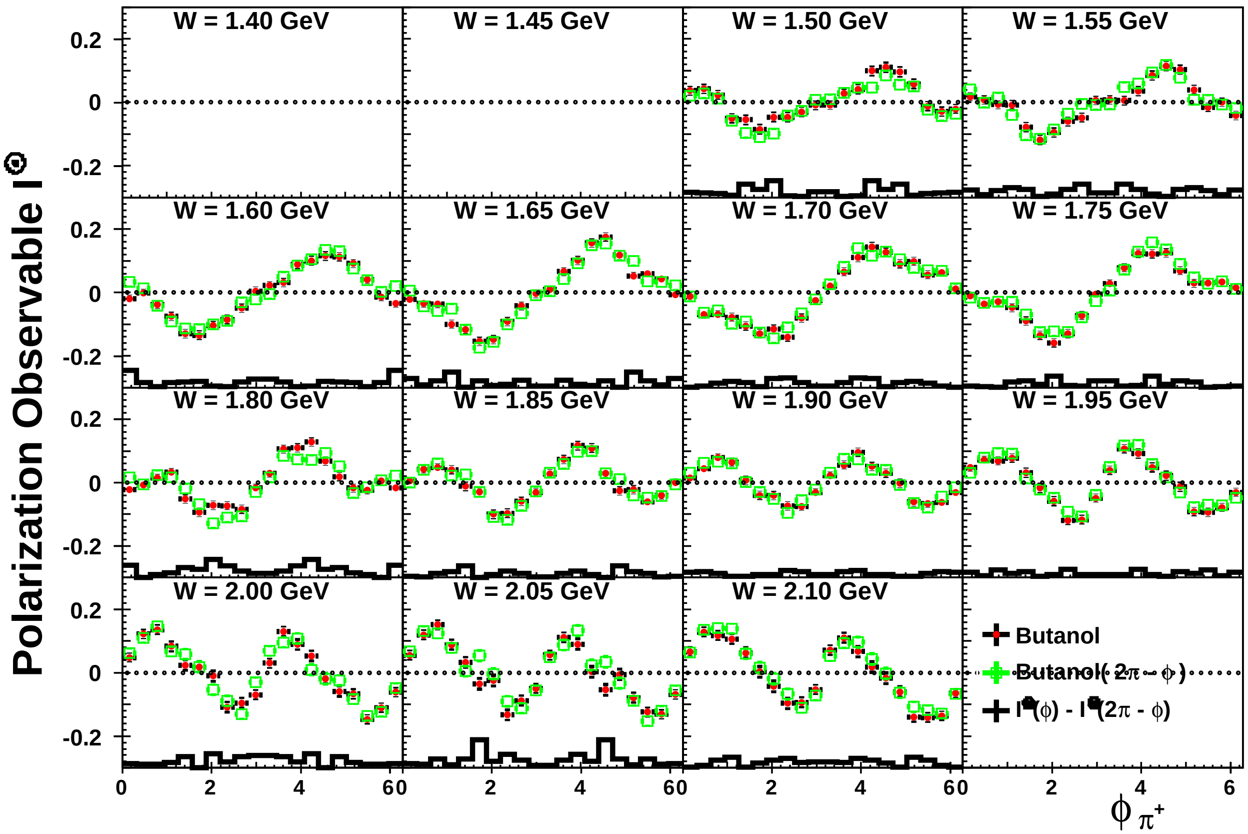

Figure 56: Measured beam-helicity asymmetry $\mathbf{I}^{\odot}$ in the reaction $\vec{\gamma}p \to p\pi^+\pi^-$ for the whole center-of-mass energy range $W \in$ [1.375, 2.125] GeV. The filled symbols denote the average observable $\mathbf{I}^{\odot}$ from the butanol data and the open symbol the observable $-\mathbf{I}^{\odot}(2\pi - \phi^*_{\pi^+})$ from the same dataset. The distribution at the bottom of each energy is the difference between the observable $\mathbf{I}^{\odot}$ and the observable $-\mathbf{I}^{\odot}(2\pi - \phi^*_{\pi^+})$.

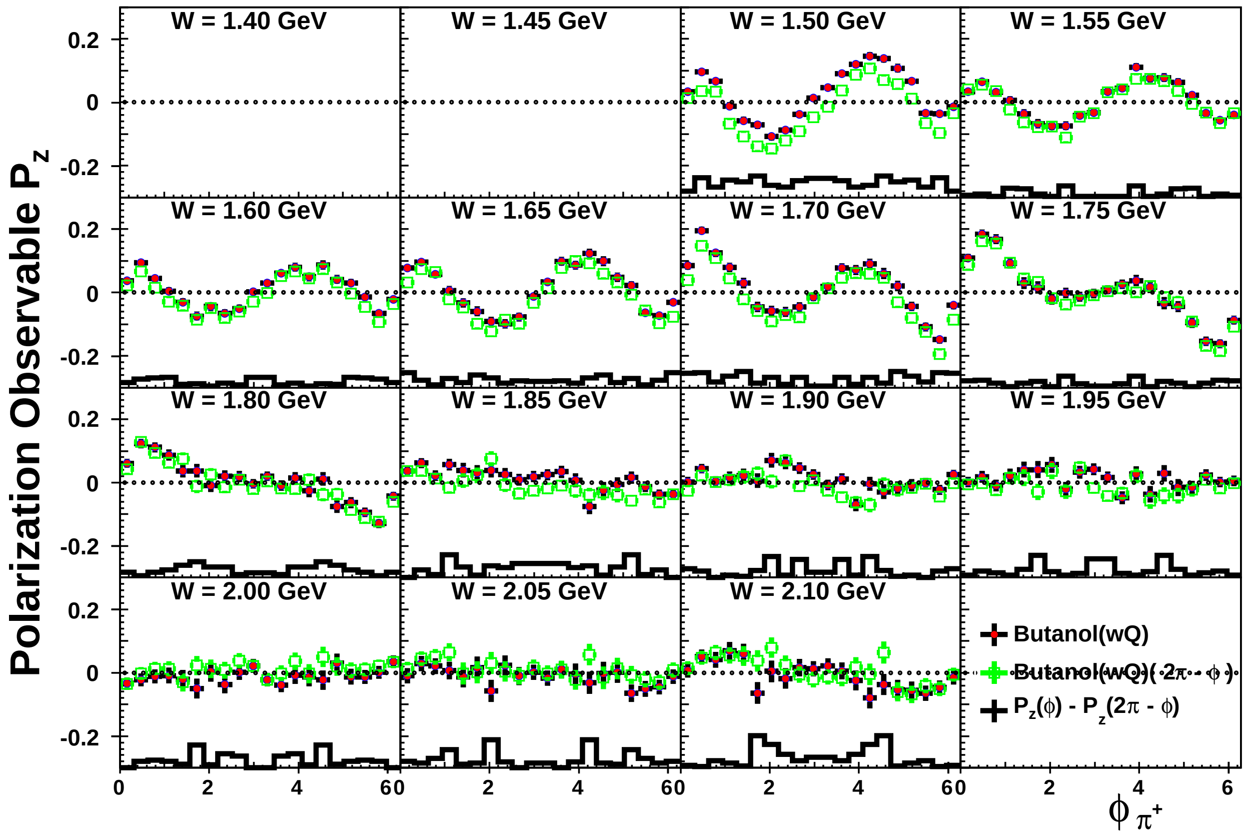

Figure 57: Measured target asymmetry $\mathbf{P_z}$ in the reaction $\gamma\vec{p} \rightarrow p\pi^+\pi^-$ for the whole center-of-mass energy range $W \in [1.375, 2.125]$ GeV. The filled symbols denote the average observable $\mathbf{P_z}$ from the butanol data weighted with the Q-factors (Section 3.9.2) and the open symbol the observable $-\mathbf{P_z}(2\pi - \phi^*_{\pi^+})$ from the same dataset. The distribution at the bottom of each energy is the difference between the observable $\mathbf{P_z}$ and the observable $-\mathbf{P_z}(2\pi - \phi^*_{\pi^+})$.

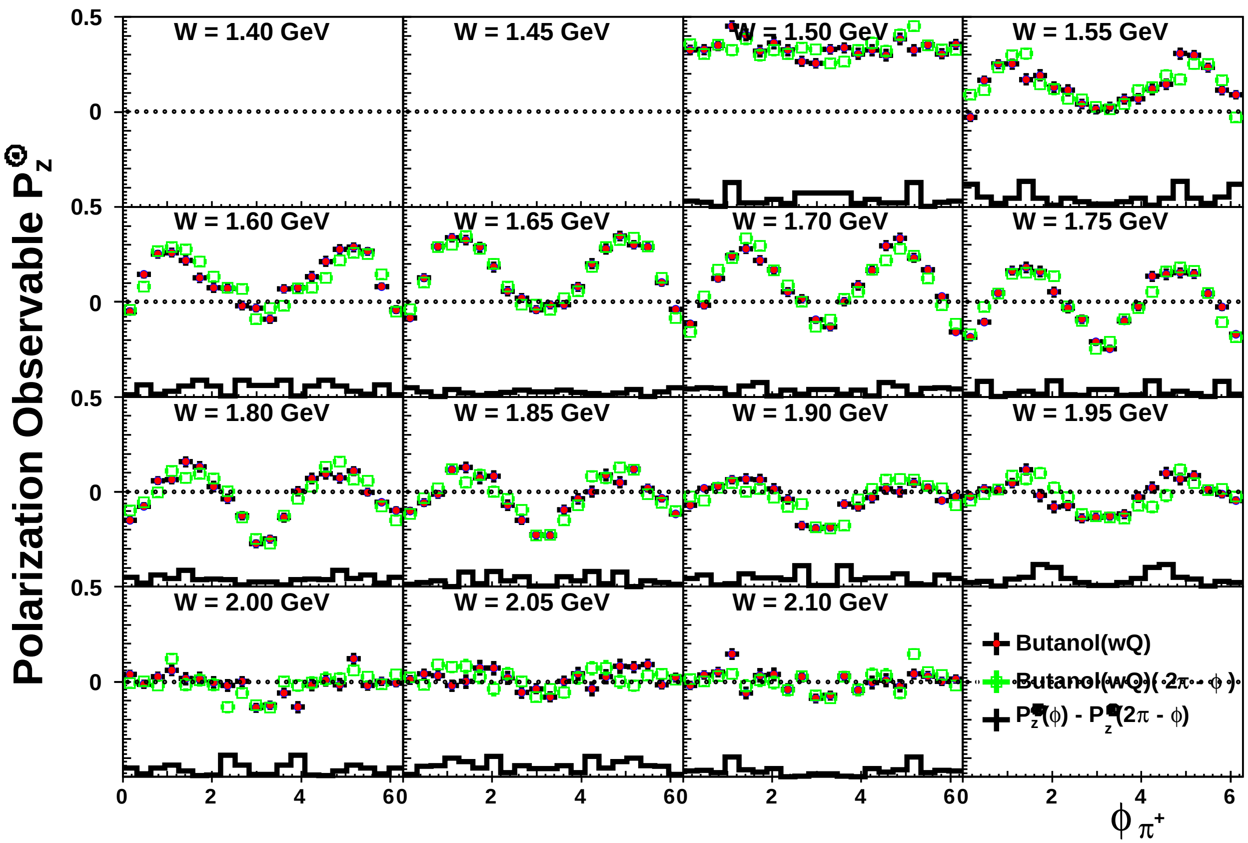

Figure 58: Measured helicity diffeence $\mathbf{P_z^{\odot}}$ in the reaction $\vec{\gamma}\vec{p} \rightarrow p\pi^+\pi^-$ for the whole center-of-mass energy range $W \in [1.375, 2.125]$ GeV. The filled symbols denote the average observable $\mathbf{P_z^{\odot}}$ from the butanol data weighted with the Q-factors (Section 3.9.2) and the open symbol the observable $\mathbf{P_z^{\odot}}(2\pi - \phi^*_{\pi^+})$ from the same dataset. The distribution at the bottom of each energy is the difference between the observable $\mathbf{P_z^{\odot}}$ and the observable $\mathbf{P_z^{\odot}}(2\pi - \phi^*_{\pi^+})$.

5 Results and Comparison of the Polarization Observables with Models

Figure 59 shows the comparison of the observable $\mathbf{I}^{\odot}$ from this analysis with the results from the CLAS-g1c experiment for the entire center-of-mass energy range, $W \in$ [1.375, 2.125] GeV. The observable $\mathbf{I}^{\odot}$ from the g9a experiment (in red) is in overall very good agreement with the published data (in light blue) [17] for the whole energy range. In addition, the observable from the CLAS-g9a experiment (this analysis) with 20 bins in the azimuthal angle, $\phi^*_{\pi^+}$, has better resolution than the results from the CLAS-g1c experiment, which used only 11 bins. Since the x-axis in this figure denotes the angle between the center-of-mass production plane (blue plane in Figure 36) and the decay plane (red plane in the same figure), the observable $\mathbf{I}^{\odot}$ must have a value of zero in this representation for $\phi^*_{\pi^+} = 0$, π, and 2π due to the odd sysmmetry. This is nicely observed in the data. Moreover, the results from the butanol data (in red, no background subtraction) and the butanol data weighted with the Q-factors (in deep blue, background subtracted) coincide very well for the whole $\phi^*_{\pi^+}$ angle range. The small discrepancies between these two results are due to the reduced statistics once the background is subtracted.

The measurements of the observable $\mathbf{I}^{\odot}$ are then compared to the results from the models of A. Fix [21] and W. Roberts [16], which are available from the threshold of the double-pion photoproduction reaction up to a center-of-mass energy of $W = 1.775$ GeV. The calculations by A. Fix and W. Roberts show the expected odd sysmmetry. The overall agreement, however, is not very good and there is even a big discrepancy between the two predictions themselves. Figure 60 shows the polarization observable $\mathbf{P_z}$, target asymmetry, for the whole center-of-mass energy range $W \in$ [1.375, 2.125] GeV. For $\mathbf{P_z}$, there are no experimentally published data available. All these model predictions provide a good estimate of the magnitude of the observable. However, there appears to be a sign issue in the representation versus $\phi^*_{\pi^+}$. Therefore, the results presented here will serve to improve predictions. Figure 61 shows the polarization observable $\mathbf{P}^{\odot}_{\mathbf{z}}$ for the whole energy range $W \in$ [1.375, 2.125] GeV. Since the observable $\mathbf{P}^{\odot}_{\mathbf{z}}$ was not published directly in [19] (only the helicity-dependent total cross-section difference, $\Delta\sigma = (\sigma_{3/2} - \sigma_{1/2})$, are available), these results are not shown in Figure 61. The polarization observable $\mathbf{P}^{\odot}_{\mathbf{z}}$ is in overall good agreement with the model predictions by A. Fix [21] and W. Roberts [16] in shape, but not in amplitude. It is worth noting though that A. Fix has been working with the results from the isospin-related channels, $n\pi^+\pi^0$ and $p\pi^0\pi^0$, measured at MAMI.

In summary, we have given an overview of measurements of the beam-helicity asymmetry, the target asymmetry, and the helicity difference for the photoproduction of two charged pions off a longitudinally-polarized proton target using circularly-polarized photons. The comparison between results using butanol events and butanol events weighted with the Q-factors (event-based background subtraction) also shows that the Q-factor method is a very useful tool to extract the polarization observables. The general lack of agreement between experiment and the theory signals severe shortcomings in the models. This is not a big surprise because the observables involving target polarization are first-time measurements. Thus, the comparison with the model predictions provides the basis for significant improvements in the interpretation of the data. A proper understanding of the $\pi^+\pi^-N$ channel in the region of overlapping nucleon resonances will provide an important contribution to solving the missing-resonance problem. We are planning on publishing the results in a series of publications including at least one PRL for the first-time measurements.

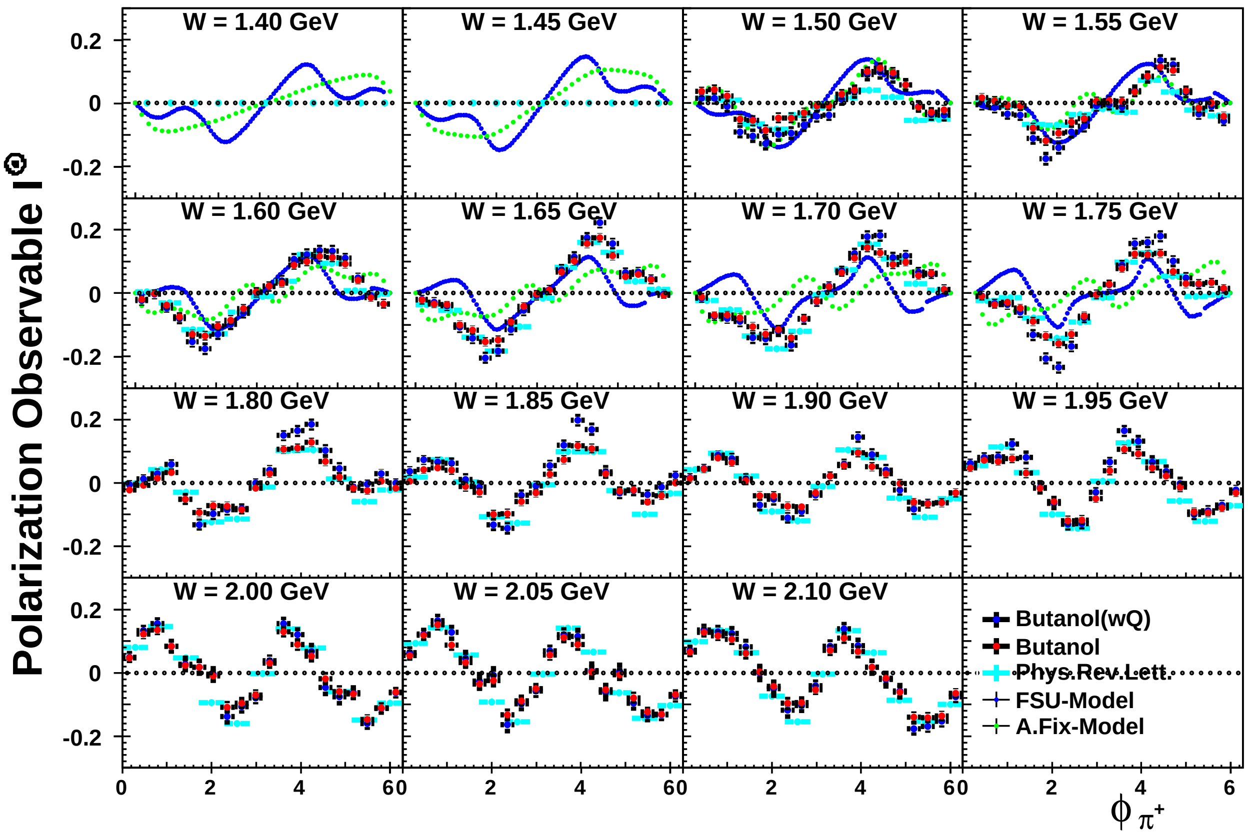

Figure 59: Comparison of the polarization observable $\mathbf{I}^{\odot}$ analyzed in this analysis and the polarization observable $\mathbf{I}^{\odot}$ published from the g1c experiment (light blue). The data are shown for the whole center-of-mass energy range $W \in [1.375, 2.125]$ GeV. All kinematic variables except for $\phi^*_{\pi^+}$ and W are integrated over. The red data points denote the observable $\mathbf{I}^{\odot}$ from the butanol data, and the blue data points denote the same observable from the butanol events weighted with the Q-factors (Section 3.9.2). The green dots indicate model calculations provided by A. Fix [21], and the blue dots by W. Roberts [16].

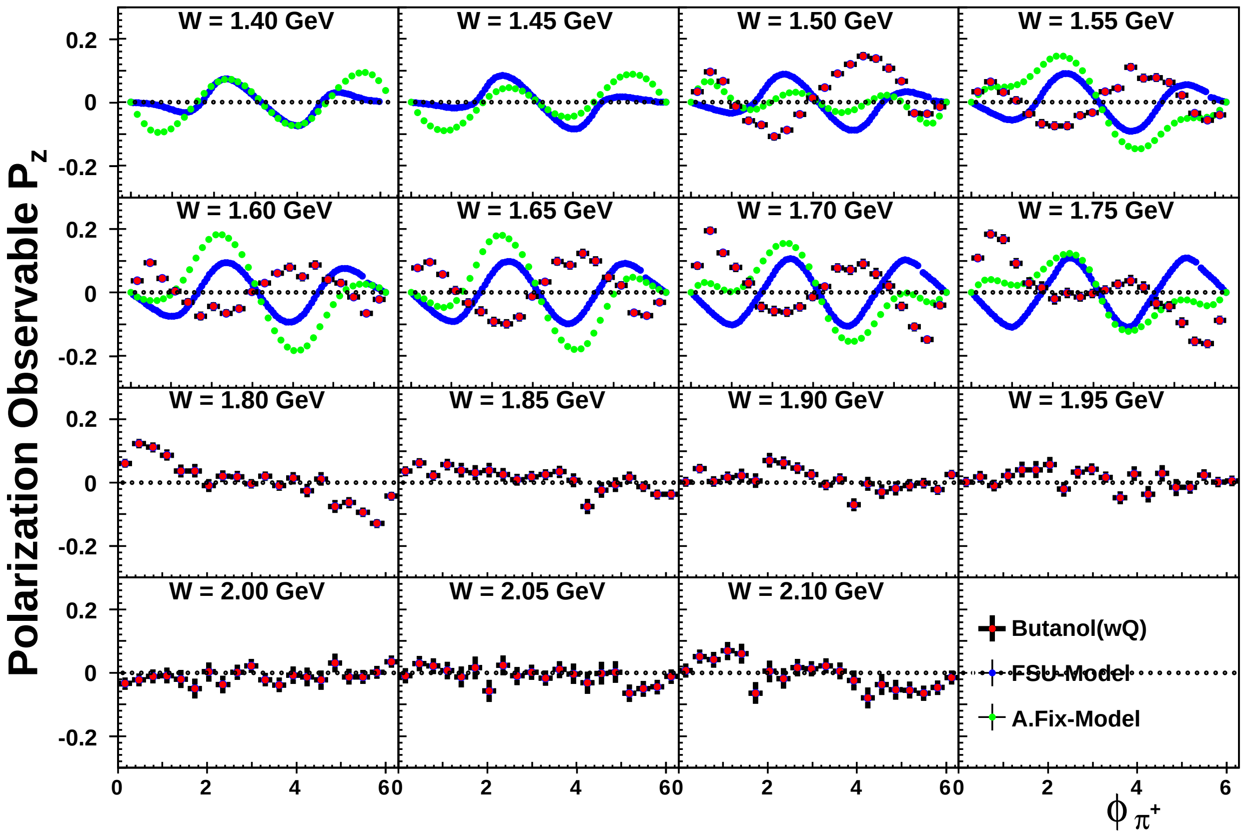

Figure 60: The polarization observable $\mathbf{P_z}$ from this analysis for the whole center-of-mass energy range $W \in [1.375, 2.125]$ GeV. All kinematic variables except for $\phi^*_{\pi^+}$ and W are integrated over. The red data points denote the observable $\mathbf{P_z}$ from the butanol events weighted with the Q-factors (Section 3.9.2). The green dots indicate model calculations provided by A. Fix [21], and the blue dots by W. Roberts [16].

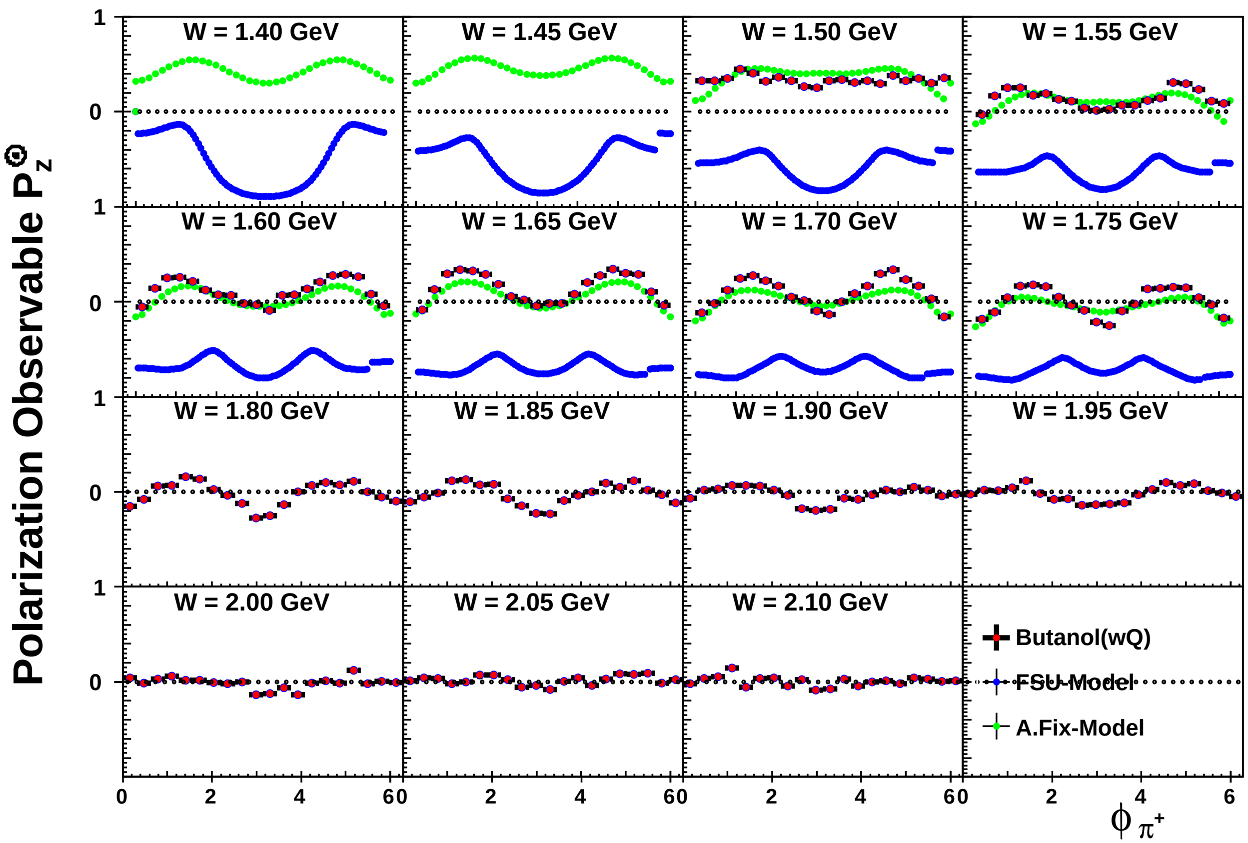

Figure 61: The polarization observable $\mathbf{P_z^{\odot}}$ from this analysis for the whole center-of-mass energy range $W \in [1.375, 2.125]$ GeV. All kinematic variables except for $\phi^*_{\pi^+}$ and W are integrated over. The red data points denote the observable $\mathbf{P_z^{\odot}}$ from butanol events weighted with the Q-factors (Section 3.9.2). The green dots indicate model calculations provided by A. Fix [21], and the blue dots by W. Roberts [16].

A Beam and Target Polarization

Table 14 illustrates the condition of the half-wave plate and the direction of the target polarization in the seven periods. The information in Table 14 should be confirmed. The condition of the half-wave plate is used for the beam polarization, as referenced in Table 13. If the condition of the half-wave plate in Table 14 per period is wrong, the beam asymmetries from three period combinations will not coincide. In conclusion, beam asymmetries made from three different period combinations show good agreement, as shown in Figure 62.

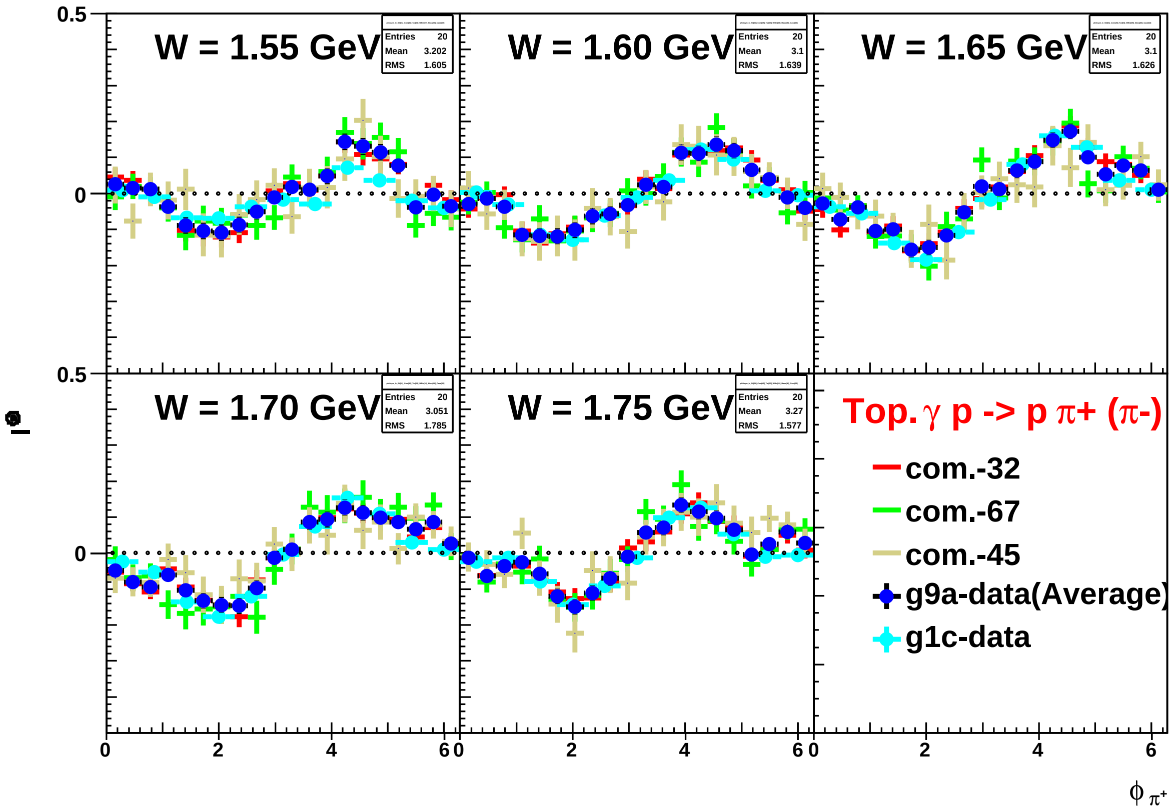

Figure 62: The beam asymmetries from the three period combinations using Topology $\gamma p \rightarrow p\pi^+(\pi^-)$ and the average beam asymmetry.

The direction of the target polarization in Table 14 can also be checked by using the target asymmetry. Target asymmetries determined from different directions of the target polarization will exhibit some structure and asymmetries using the same directions will be zero, as shown in Figure 63.

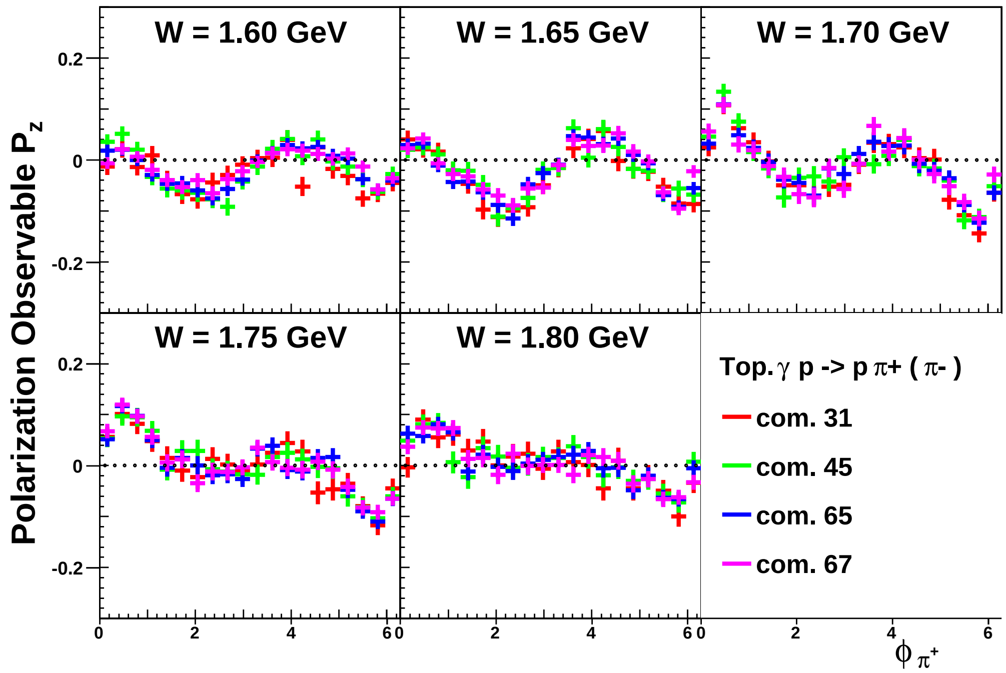

(a) Combinations of different target polarizations.

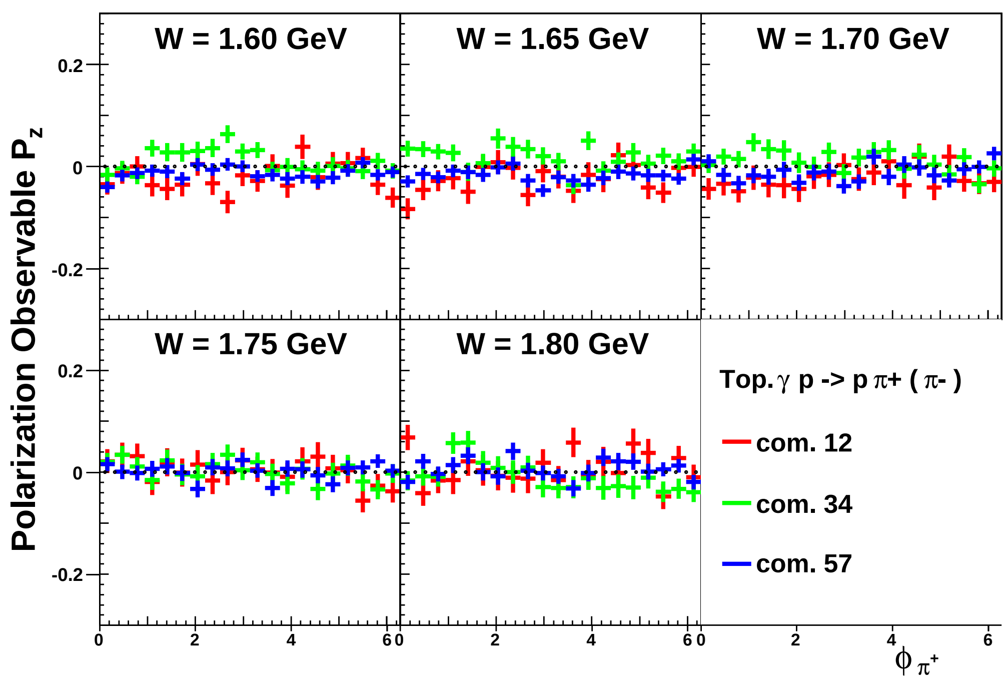

(b) Combinations of the same target polarization.

Figure 63: The target asymmetry made from different target polarizations (a) and from the same target polarization (b).

B Beam Charge Asymmetry

Table 9 shows the electron beam charge asymmetry in the g9a dataset and the total number of $\gamma p \to p\pi^+\pi^-$ events for the two helicity states. The electron beam charge asymmetry can be defined by:

$$Y^{\pm} = N^{\pm}/\alpha^{\pm}\,, \tag{46}$$

$$\begin{aligned}
Y^{+} &= \frac{1}{\alpha^{+}}\left(\frac{N(\phi,\rightarrow\Rightarrow)}{\Lambda_z(\Rightarrow)F(\Rightarrow)} + \frac{N(\phi,\rightarrow\Leftarrow)}{\Lambda_z(\Leftarrow)F(\Leftarrow)}\right) \sim \frac{A(\phi)}{\alpha^{+}}\Big(\frac{1}{\Lambda_z(\Rightarrow)} + \frac{1}{\Lambda_z(\Leftarrow)}\Big)\Big(1+\delta_{\odot}\mathbf{I}^{\odot}\Big)\,,\\
Y^{-} &= \frac{1}{\alpha^{-}}\left(\frac{N(\phi,\leftarrow\Rightarrow)}{\Lambda_z(\Rightarrow)F(\Rightarrow)} + \frac{N(\phi,\leftarrow\Leftarrow)}{\Lambda_z(\Leftarrow)F(\Leftarrow)}\right) \sim \frac{A(\phi)}{\alpha^{-}}\Big(\frac{1}{\Lambda_z(\Rightarrow)} + \frac{1}{\Lambda_z(\Leftarrow)}\Big)\Big(1-\delta_{\odot}\mathbf{I}^{\odot}\Big)\,,
\end{aligned} \tag{47}$$

and the asymmetry can be calculated using the corrected number of events for helicity plus and minus. The beam asymmetry A^{beam}, taking into account the effect of the electron beam charge asymmetry, is given by:

$$\begin{aligned}
A^{\text{beam}} &= \frac{Y^{+}-Y-}{Y^{+}+Y^{-}} = \frac{\frac{1}{\alpha^{+}}\left(\frac{N(\phi,\rightarrow\Rightarrow)}{\Lambda_z(\Rightarrow)F(\Rightarrow)} + \frac{N(\phi,\rightarrow\Leftarrow)}{\Lambda_z(\Leftarrow)F(\Leftarrow)}\right) - \frac{1}{\alpha^{-}}\left(\frac{N(\phi,\leftarrow\Rightarrow)}{\Lambda_z(\Rightarrow)F(\Rightarrow)} + \frac{N(\phi,\leftarrow\Leftarrow)}{\Lambda_z(\Leftarrow)F(\Leftarrow)}\right)}{\frac{1}{\alpha^{+}}\left(\frac{N(\phi,\rightarrow\Rightarrow)}{\Lambda_z(\Rightarrow)F(\Rightarrow)} + \frac{N(\phi,\rightarrow\Leftarrow)}{\Lambda_z(\Leftarrow)F(\Leftarrow)}\right) + \frac{1}{\alpha^{-}}\left(\frac{N(\phi,\leftarrow\Rightarrow)}{\Lambda_z(\Rightarrow)F(\Rightarrow)} + \frac{N(\phi,\leftarrow\Leftarrow)}{\Lambda_z(\Leftarrow)F(\Leftarrow)}\right)}\\
&= \frac{\frac{1+\delta_{\odot}I^{\odot}}{\alpha^{+}} - \frac{1-\delta_{\odot}I^{\odot}}{\alpha^{-}}}{\frac{1+\delta_{\odot}I^{\odot}}{\alpha^{+}} + \frac{1-\delta_{\odot}I^{\odot}}{\alpha^{-}}}
\end{aligned} \tag{48}$$

The polarization observable $\mathbf{I}^{\odot}$ is given by:

$$I^{\odot} = \frac{1}{\delta_{\odot}}\frac{A^{\text{beam}}\left(\frac{1}{\alpha^{+}}+\frac{1}{\alpha^{-}}\right) - \left(\frac{1}{\alpha^{+}}-\frac{1}{\alpha^{-}}\right)}{\left(\frac{1}{\alpha^{+}}+\frac{1}{\alpha^{-}}\right) - A^{\text{beam}}\left(\frac{1}{\alpha^{+}}-\frac{1}{\alpha^{-}}\right)}\,. \tag{49}$$

Equation 35 shows the polarization observable $\mathbf{I}^{\odot}$ without the effect of the beam charge asymmetry and equation 49 shows the polarization observable $\mathbf{I}^{\odot}$ with the effect of the beam charge asymmetry. Figure 64 shows the difference. The electron beam charge asymmetry can be neglected in this analysis.

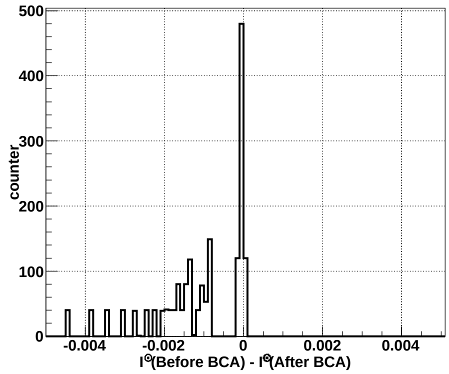

Figure 64: Comparison between the polarization observables $\mathbf{I}^{\odot}$ before and after applying the beam charge asymmetry.

C Effect of Bound-Nucleon Events on $\mathbf{I}^{\odot}$

The butanol data are composed of free-proton, bound-nucleon, and additional background events. However, we cannot easily distinguish between the free-proton events and the remaining events in the butanol data.

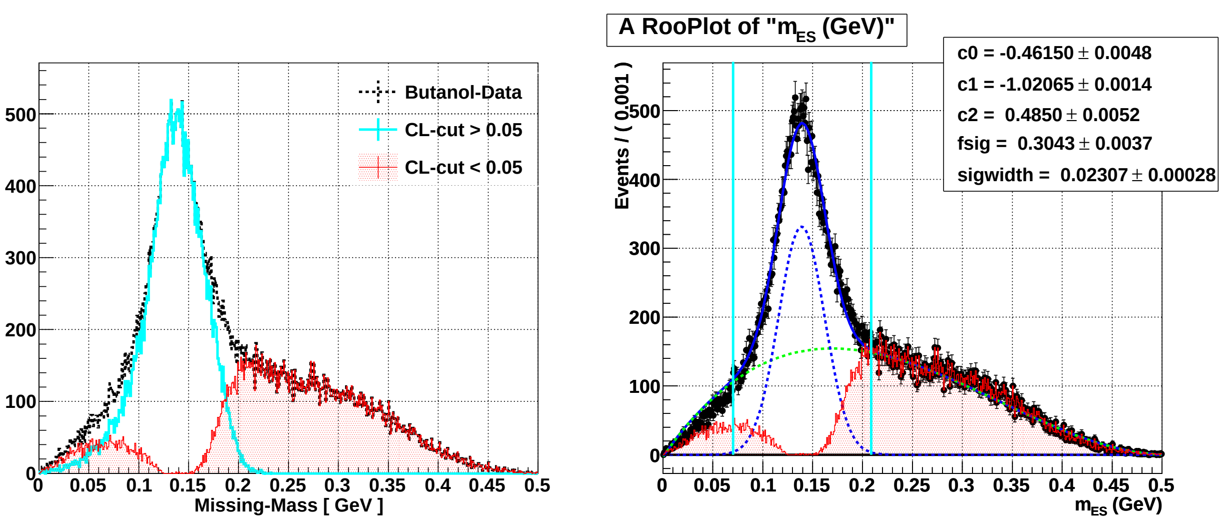

(a) (b)

Figure 65: (a) The missing-mass distribution for the butanol target with and without the confidence-level cut. (b) The same missing-mass distribution fitted with a gaussian and a second-order chebyshev polynomial. The data are selected according to $W \in [1.575, 1.625]$ GeV and Topology $\gamma p \rightarrow p\pi^{+}(\pi^{-})$. The hatched area includes events whose the confidence-level is less than 0.05. The light blue line is located at the π^{+} mass $\pm\, 3\sigma$ of the fitted gaussian. The dashed green line is the second-order chebyshev polynomial.

Figure 65 (a) shows missing-mass distributions including the effects of different confidence-level cuts. In Figure 65 (b), the free-proton data are described with a gaussian function. The bound-nucleon and background data are described using a second-order chebyshev polynomial. Since the CLAS missing-mass distributions from a liquid-hydrogen target (for the two-pion channel) are typically background free, we assume that the background events visible in Figure 65 (a) stem from the carbon in the butanol target. We also assume that the beam asymmetry made from the free-proton events is similar for bound nucleons and that g9a dataset is not sensitive to distinguish between the beam asymmetries for free-proton and bound-nucleon events.

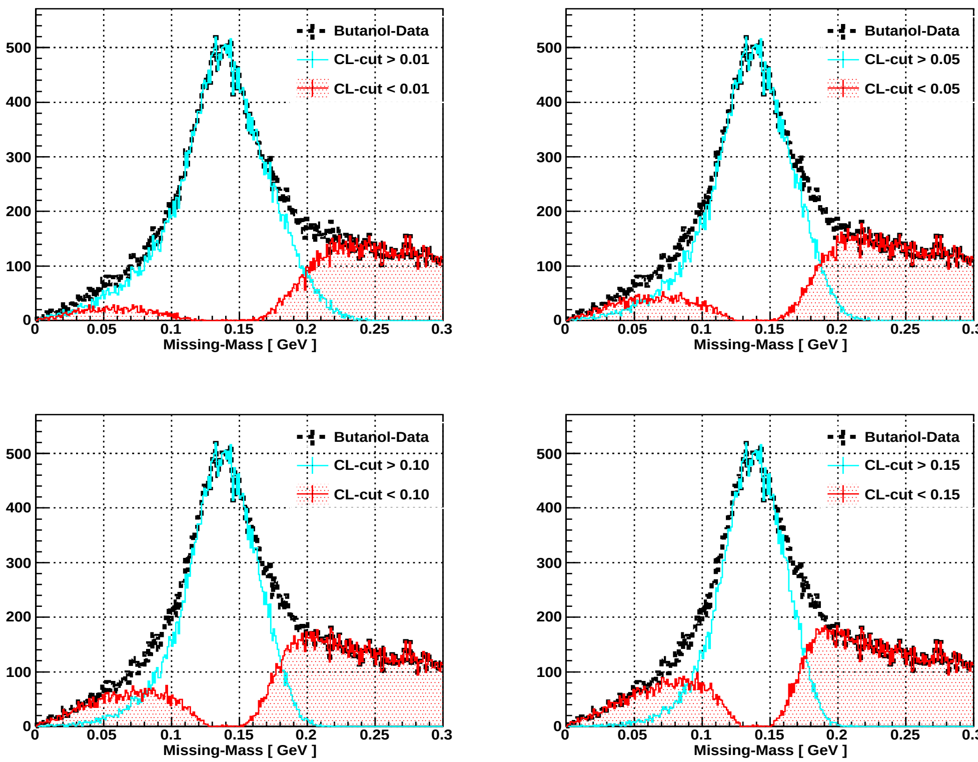

Figure 66: The missing-mass distributions from the butanol target made with different CL cuts. The data are selected according to $W \in [1.575,\ 1.625]$ GeV and Topology $\gamma p \to p\pi^+(\pi^-)$.

Figure 66 shows the missing-mass distributions of Topology $\gamma p \to p\pi^+(\pi^-)$ for the confidence-level cuts 1 %, 5 %, 10 %, and 15 %. When the confidence-level cut is increased, more and more background events are cut out. The different amount of background events under the free-proton peak in Figure 66 can have an effect on the amplitude of the beam asymmetry. Figure 67 shows the comparison between the polarization observables $\mathbf{I}^{\odot}$ extracted with the confidence-level cuts 1 %, 5 %, 10 %, and 15 % to the published g1c data. Figure 67 shows that the beam asymmetry is more or less independent of the confidence-level cut. The different amount of background events under the free-proton peak has clearly no big effect on the structure of the beam asymmetry.

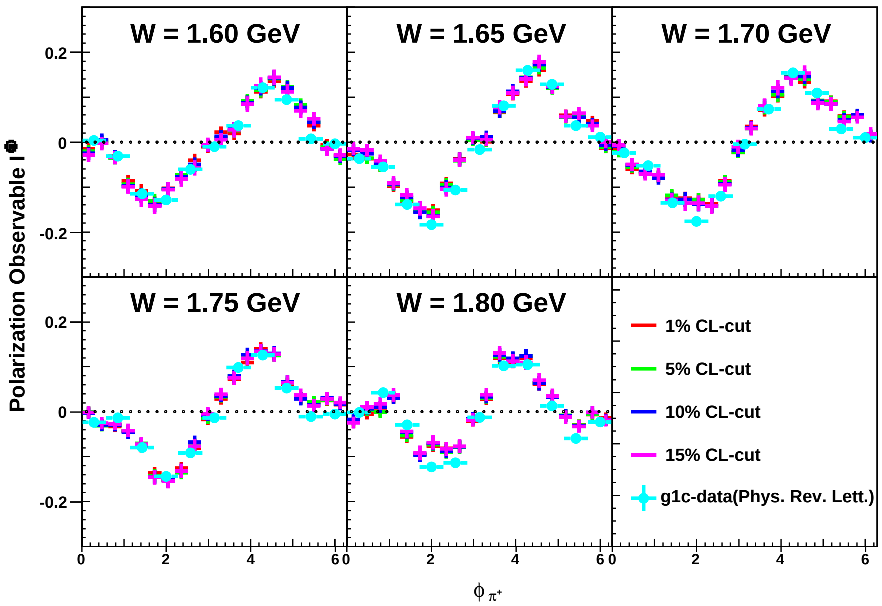

Figure 67: The average beam asymmetries extracted with a 1 %, 5 %, 10 %, and 15 % CL-cut in comparison with the polarization observable $\mathbf{I}^{\odot}$ published from the CLAS-g1c experiment.

Our conclusion is that after applying the confidence-level cut, the effect of background events is almost negligible for the beam-helicity asymmetry. The polarization observables $\mathbf{I}^{\odot}$ from free-proton and bound-nucleon events have similar values, i.e. the FROST experiment is not sensitive to the effects of Fermi motion. Figure 68 (a) shows the differences ($\mathbf{I}^{\odot}{}_{X\,\%\,\mathrm{CLcut}} - \mathbf{I}^{\odot}{}_{5\,\%\,\mathrm{CLcut}}$) and Figure 68 (b) describes the percent error between X % CL-cut and 5 % CL-cut when X is a 1 % CL-cut, a 10 % CL-cut, or a 15 % CL-cut.

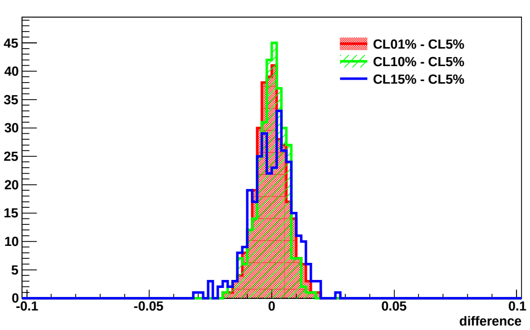

(a) Difference

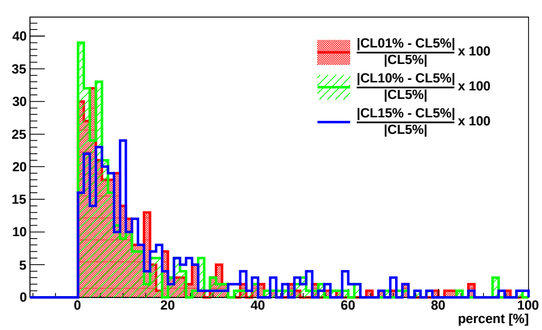

(b) Percent error

Figure 68: Difference and percent error between the polarization observable $\mathbf{I}^{\odot}$ for a 5 % CL-cut and other CL cuts.

D Error Propagation

The target polarization Λ_z, normalization factor F, and beam polarization $\delta_\odot$ in Equation 35 also have systematic errors the effects of which on the polarization observable $\mathbf{I}^\odot$ must be taken into account. The polarization observable $\mathbf{I}^\odot$ is given by:

$$\mathbf{I}^\odot = \frac{1}{\bar{\delta}_\odot} \frac{N(\rightarrow) - N(\leftarrow)}{N(\rightarrow) + N(\leftarrow)}\,, \tag{50}$$

where

$$N(\rightarrow) = \frac{N(\rightarrow\Rightarrow)}{\{\Lambda(\Rightarrow)/\Lambda(\Leftarrow)\}\{F(\Rightarrow)/F(\Leftarrow)\}} + N(\rightarrow\Leftarrow)\,, \tag{51}$$

and

$$N(\leftarrow) = \frac{N(\leftarrow\Rightarrow)}{\{\Lambda(\Rightarrow)/\Lambda(\Leftarrow)\}\{F(\Rightarrow)/F(\Leftarrow)\}} + N(\leftarrow\Leftarrow)\,. \tag{52}$$

In the following, we set $A = \Lambda(\Rightarrow)/\Lambda(\Leftarrow)$ and $B = F(\Rightarrow)/F(\Leftarrow)$. The errors of $N(\rightarrow)$ and $N(\leftarrow)$ due to the target polarization and normalization factor can then be calculated using standard error propagation:

$$\Delta N(\rightarrow) = \sqrt{\left(\frac{N(\rightarrow\Rightarrow)\cdot\Delta A}{A^2\cdot B}\right)^2 + \left(\frac{N(\rightarrow\Rightarrow)\cdot\Delta B}{A\cdot B^2}\right)^2}\,, \tag{53}$$

and

$$\Delta N(\leftarrow) = \sqrt{\left(\frac{N(\leftarrow\Rightarrow)\cdot\Delta A}{A^2\cdot B}\right)^2 + \left(\frac{N(\leftarrow\Rightarrow)\cdot\Delta B}{A\cdot B^2}\right)^2}\,. \tag{54}$$

The error of the polarization observable $\mathbf{I}^\odot$ is also given by standard error propagation:

$$\begin{aligned}\Delta I^\odot &= \sqrt{\left(\frac{\partial I^\odot\cdot\Delta N(\rightarrow)}{\partial N(\rightarrow)}\right)^2 + \left(\frac{\partial I^\odot\cdot\Delta N(\leftarrow)}{\partial N(\leftarrow)}\right)^2 + \left(\frac{\partial I^\odot\cdot\Delta\bar{\delta}_\odot}{\partial\bar{\delta}_\odot}\right)^2} \\ &= \sqrt{\frac{(2N(\leftarrow))^2\cdot(\Delta N(\rightarrow))^2}{(\bar{\delta}_\odot)^2\cdot(N(\rightarrow)+N(\leftarrow))^4} + \frac{(2N(\rightarrow))^2\cdot(\Delta N(\leftarrow))^2}{(\bar{\delta}_\odot)^2\cdot(N(\rightarrow)+N(\leftarrow))^4} + \frac{(N(\rightarrow)-N(\leftarrow))^2\cdot(\Delta\bar{\delta}_\odot)^2}{(\bar{\delta}_\odot)^4\cdot(N(\rightarrow)+N(\leftarrow))^2}}\end{aligned} \tag{55}$$

The error of the polarization observable $\mathbf{I}^\odot$ from Equation 55 consists of three parts: the error due to the target polarization, the error due to the normalization factor, and the error due to the beam polarization. Figure 69 shows the error distributions for $\mathbf{I}^\odot$ from the three parts.

The error from the target polarization is given by (Equations 55 and 53):

$$\Delta I^\odot_{Tar.Pol.} = \sqrt{\frac{2N(\leftarrow)^2\cdot N(\rightarrow\Rightarrow)^2 + 2N(\rightarrow)^2\cdot N(\leftarrow\Rightarrow)^2}{(\bar{\delta}_\odot)^2\cdot(N(\rightarrow)+N(\leftarrow))^4\cdot(A^2\cdot B)^2}\cdot(\Delta A)^2}\,. \tag{56}$$

The error from the normalization factor is given by:

$$\Delta I^\odot_{Nor.Fac.} = \sqrt{\frac{2N(\leftarrow)^2\cdot N(\rightarrow\Rightarrow)^2 + 2N(\rightarrow)^2\cdot N(\leftarrow\Rightarrow)^2}{(\bar{\delta}_\odot)^2\cdot(N(\rightarrow)+N(\leftarrow))^4\cdot(A\cdot B^2)^2}\cdot(\Delta B)^2}\,. \tag{57}$$

The error from the beam polarization is given by:

$$\Delta I^{\odot}_{BeamPol.} = \sqrt{\frac{1}{(\bar{\delta}_{\odot})^4} \cdot \left(\frac{N(\rightarrow) - N(\leftarrow)}{N(\rightarrow) + N(\leftarrow)}\right)^2 \cdot (\Delta\bar{\delta}_{\odot})^2}\,, \tag{58}$$

and the error of polarization observable $\mathbf{I}^{\odot}$ is given by:

$$\Delta I^{\odot} = \sqrt{\left(\Delta I^{\odot}_{Tar.Pol.}\right)^2 + \left(\Delta I^{\odot}_{Nor.Fac.}\right)^2 + \left(\Delta I^{\odot}_{Beam.Pol.}\right)^2}\,. \tag{59}$$

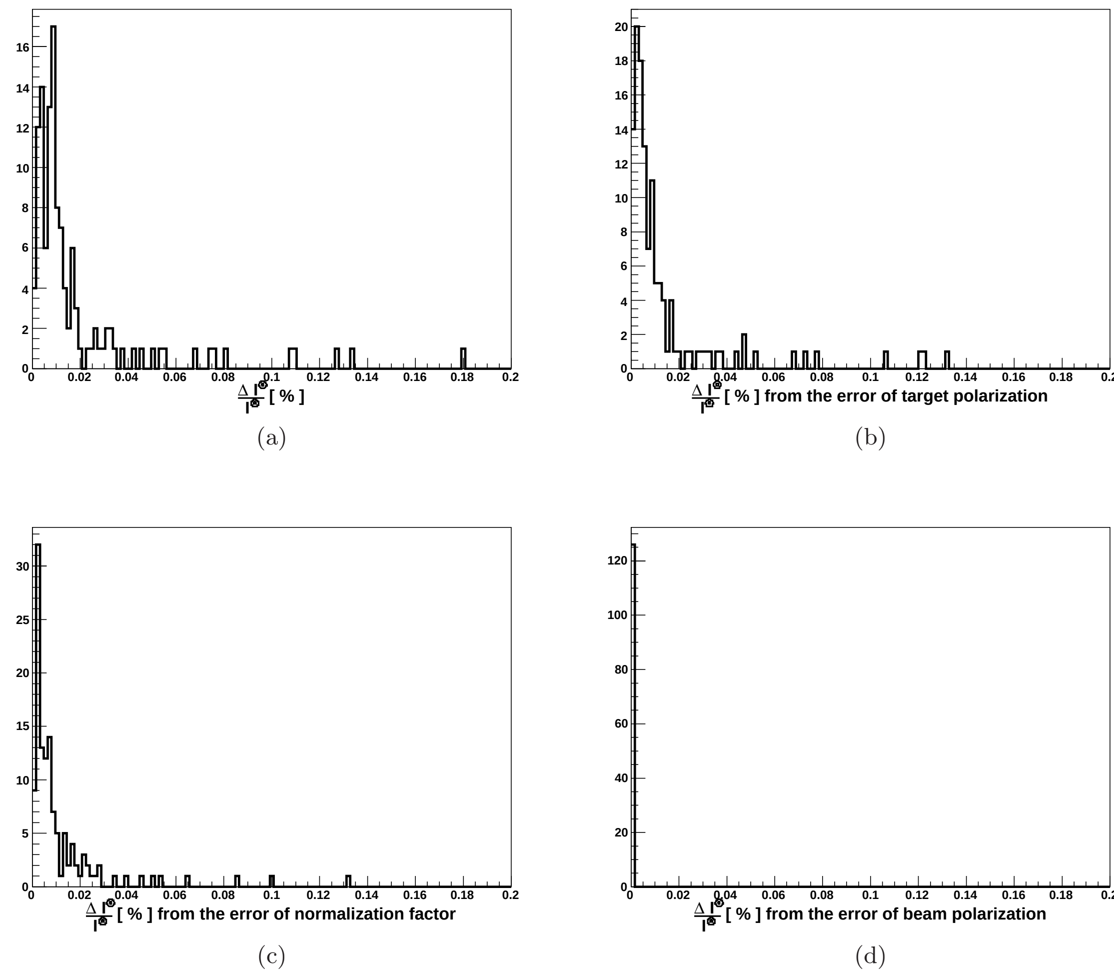

Figure 69: The statistical error contribution on observable $\mathbf{I}^{\odot}$ from the target polarization (b), from the normalization factor (c), and the beam polarization (d). The sum of these errors is shown in (a).

References

[1] V. Crede, M. Bellis, and S. Strauch *et al.* [CLAS Collaboration], "Measurement of $\pi^+\pi^-$ Photoproduction in Double-Polarization Experiments using CLAS," Jefferson Lab Proposal, **E-06-013**, (2006).

[2] B. A. Mecking *et al.* [CLAS Collaboration], "The CEBAF Large Acceptance Spectrometer (CLAS)," Nucl. Instrum. Meth. A **503**, 513 (2003).

[3] D. I. Sober *et al.*, "The bremsstrahlung tagged photon beam in Hall B at JLab," Nucl. Instrum. Meth. A **440**, 263 (2000).

[4] C. D. Keith *et al.*, "The Jefferson Lab Frozen Spin Target," Nucl. Instrum. Meth. A **684**, 27 (2012) [arXiv:1204.1250 [physics.ins-det]].

[5] E. Pasyuk, "A Brief User Guide to GPID," CLAS Note 2007-008 (2007).

[6] M. Williams, C. A. Meyer, "Kinematic Fitting in CLAS," CLAS Note 2003-017 (2003).

[7] E. Pasyuk, "Energy loss corrections for charged particles in CLAS," CLAS Note 2007-016 (2007).

[8] S. Stepanyan *et al.*, "Energy calibration of the JLab bremsstrahlung tagging system," Nucl. Instrum. Meth. A **572**, 654 (2007) [physics/0608302 [physics.ins-det]].

[9] M. Dugger, C. Hanretty, "Correction to the incident photon energy for g8b data," CLAS Note 2009-030 (2009).

[10] M. Dugger, "Check of tagger photon energy for g9a (version 2)," FROST Group Meeting, July 27th (2010).

[11] H. Olsen and L. C. Maximon,"Photon and Electron Polarization in High-Energy Bremsstrahlung and Pair Production with Screening," Phys. Rev. **114**, 887 (1959).

[12] E. Pasyuk, "The hydrogen contamination of the carbon data in g9a experiment", FROST Group Meeting, March 13th, 2013.

[13] M. Dugger, B. G. Ritchie, "DRAFT of CLAS-note: Phase space dependent scale factors fro FROST g9a data."

[14] M. Williams, M. Bellis and C. A. Meyer, "Separating Signals from Non-Interfering Backgrounds using Probabilistic Event Weightings," arXiv:0804.3382 [physics.data-an].

[15] W. Verkerke, D. Kirkby, "RooFit Users Manual v2.91," Document version 2.91-33, October 14th (2008).

[16] W. Roberts and T. Oed, "Polarization observables for two-pion production off the nucleon," Phys. Rev. C **71**, 055201 (2005) [nucl-th/0410012].

[17] S. Strauch *et al.* [CLAS Collaboration], "Beam-helicity asymmetries in double-charged-pion photoproduction on the proton," Phys. Rev. Lett. **95**, 162003 (2005) [hep-ex/0508002].

[18] D. Krambrich *et al.* [Crystal Ball at MAMI Collaboration], "Beam-Helicity Asymmetries in Double Pion Photoproduction off the Proton," Phys. Rev. Lett. **103**, 052002 (2009).

[19] J. Ahrens *et al.* [GDH and A2 Collaborations], "First measurement of the helicity dependence for the $\gamma p \to p\pi^+\pi^-$ reaction," Eur. Phys. J. A **34**, 11 (2007).

[20] K. Livingston, "Binned fitting techniques for measuring photon beam asymmetry," CLAS Note 2012-010 (2012).

[21] A. Fix and H. Arenhovel, "Double pion photoproduction on nucleon and deuteron," Eur. Phys. J. A **25**, 115 (2005) [nucl-th/0503042].